

SUITABILITY STUDIES WITH AN HV-CMOS SENSOR
FOR CONTINUOUS USE AND DETECTION OF
SECONDARY PARTICLE TRACKS WITH
A BEAM TELESCOPE DURING ION IRRADIATION
AT A MEDICAL IRRADIATION FACILITY

STUDIEN MIT EINEM HV-CMOS-SENSOR ZUR EIGNUNG IM
LANGZEITBETRIEB UND ZUR DETEKTION VON
SEKUNDÄRTEILCHENSPIREN MIT EINEM STRAHLTELESKOP AN EINER
MEDIZINISCHEN BESTRAHLUNGSEINRICHTUNG

MASTER THESIS

by

Christina Klauda

At the Department of Physics
Institute of Experimental Particle Physics (ETP)

REVIEWER: Prof. Dr. Ulrich Husemann
SECOND REVIEWER: Prof. Dr. Ivan Perić
ADVISOR: Dr. Rudolf Schimassek
SECOND ADVISOR: Dr. Stefan Maier

KARLSRUHE, 10.01.2022

Christina Klauda:
Suitability Studies with an HV-CMOS Sensor
for Continuous Use and Detection of
Secondary Particle Tracks with
a Beam Telescope during Ion Irradiation
at a Medical Irradiation Facility
January 2022

Declaration and Review

I hereby declare that the work in this master thesis was carried out following the requirements of the University's regulations and that it has not been submitted for any other academic award. Except where indicated by specific reference in the text, the work is the candidate's work. Work that was done in collaboration with, or with the assistance of, others is indicated as such.

Karlsruhe, January 2022

(Christina Klauda)

This thesis has been accepted by the first reviewer of the master thesis.

Karlsruhe, January 2022

(Prof. Dr. Ulrich Husemann)

Contents

1. Introduction	1
2. Particle Detection with Silicon Sensors	3
2.1. Physical Properties of Silicon	3
2.1.1. Electronic Band Structure	3
2.1.2. Doping	4
2.1.3. pn-Junction	6
2.1.4. The Metal Oxide Field Effect Transistor (MOSFET)	6
2.2. Interaction of Particles with Matter	8
2.2.1. Generation of Charge Carriers in Silicon	8
2.2.2. Interaction Processes of Charged Particles	8
2.2.3. Interaction Processes of Neutral Particles	10
2.2.4. Multiple Scattering in Thick Layers	12
2.3. Working Principle of Silicon Sensors	12
2.4. Radiation Damage	13
2.4.1. Bulk Damage	14
2.4.2. Surface Damage	14
3. Applied HV-CMOS Technology	19
3.1. Classical Hybrid Silicon Sensors	19
3.2. Principle of Monolithic Active Pixel Sensors	19
3.3. Principle of Monolithic HV-CMOS Sensors	20
3.4. Integrated Sensor: ATLASpix3	21
3.5. Signal Processing and Readout System for ATLASpix3	21
3.6. Calibration of the Sensor	23
3.6.1. Measurement of S-Curves	23
3.6.2. Detection Threshold Tuning	24
3.6.3. Amplitude Information Calibration	25
4. Applications of HV-CMOS Sensors	27
4.1. The Large Hadron Collider and its High Luminosity Upgrade	27
4.1.1. The Large Hadron Collider (LHC)	27
4.1.2. The ATLAS Experiment	28
4.1.3. High Luminosity and ATLAS Inner Tracker Upgrade	29
4.2. Monitoring of Medical Irradiation Treatments	31
4.2.1. Therapy with Heavy Ions	31
4.2.2. Irradiation Facility: Heidelberg Ion Therapy Center (HIT)	32
4.2.3. Beam Monitoring	34
4.2.4. HV-CMOS Sensors as Beam Monitoring Device	37
5. Irradiation Studies with ATLASpix3	39
5.1. Motivation of Irradiation by Previous Studies	39
5.2. Measurement and Analysis Procedure	41
5.2.1. Mechanical Setup	41
5.2.2. Irradiation	42
5.2.3. S-Curve Scan and Tuning	43
5.2.4. Energy Calibration with X-Ray Spectrum Lines	44

5.2.5.	Strontium-90 Measurement	46
5.2.6.	Analysis Procedure	46
5.3.	Characterization before Irradiation	46
5.3.1.	S-Curve Detection and Tuning	48
5.3.2.	Time over Threshold (ToT) Calibration	48
5.4.	Test Signal Measurements	50
5.4.1.	Dispersion of Threshold Values	50
5.4.2.	Dispersion in Tuning Values	52
5.4.3.	Dispersion of Noise	52
5.5.	Measurements and Calibration with X-Rays	52
5.5.1.	Energy Calibration	54
5.5.2.	Gain Dispersion	56
5.5.3.	Dispersion of Detection Rate – Indirect X-Ray Irradiation	58
5.6.	Measurements with Charged Particles	60
5.6.1.	Strontium-90 Signal Detection	60
5.6.2.	Dispersion of Detection Rate – Charged Particles	62
5.6.3.	Cluster Size Dispersion	63
5.6.4.	Leakage Current	63
5.7.	Summary and Comparison with Beam Dump Studies	64
6.	Beam Test – Secondary Particle Tracking	67
6.1.	Previous Studies on Secondary Particle Tracking	67
6.2.	Experimental Setup	68
6.2.1.	Mechanical Setup	70
6.2.2.	Properties of four-layer ATLASpix3 Beam Telescope	71
6.3.	Pre-Characterization of the Telescope Sensor Layers	73
6.4.	Measurement Procedure	74
6.5.	Corryvreckan Framework	77
6.6.	Preparation of Beam Test Data	78
6.6.1.	Spill Structure and Separation of Data Files	78
6.6.2.	Clustering	78
6.6.3.	Correlations	79
6.6.4.	Sensor Alignment	82
6.7.	Analysis of Beam Test Data	83
6.7.1.	Secondary Particle Tracking	83
6.7.2.	Reconstruction of Penetration Depth and Track Origin	85
6.7.3.	Particle Rates	89
6.8.	Summary	89
7.	Summary and Outlook	93
A.	Irradiation Study with ATLASpix3	95
B.	Secondary Particle Studies with ATLASpix3 Telescope	97
B.1.	Slow Neutron Conversion with Polyethylene (PE)	97
B.2.	Pre-Characterization of Sensor Layers	99
B.3.	Corryvreckan Configuration Files	104
	Bibliography	107

1

Introduction

With large high energy physics experiments as ATLAS¹ at the Large Hadron Collider (LHC), located at CERN², scientists strive for better understanding of nature's elementary processes. Next to the beam energy, the luminosity is a measure of the LHC performance [HM06]. To further increase size of datasets recorded at the LHC, a maximum instantaneous luminosity of $\mathcal{L} = 5 \times 10^{34} \text{ cm}^{-2}\text{s}^{-1}$ is aimed for with the high-luminosity (HL) upgrade until the end of 2027 [Bej+17]. In the course of this upgrade and within the increasing requirements for particle detectors in general, the HV-CMOS silicon sensor technology was invented by Ivan Perić in 2007 [Per07]. This allows the instrumentation of large areas for tracking at lower cost than technologies used previously. The technology enables a monolithic sensor concept to be built on a high-voltage CMOS process and a direct implementation of the readout electronics in the sensor diode. Fast separation and collection of the generated charge are achieved via drift in the depleted zone with depletion voltages up to 120 V [Kie+18]. A smaller material budget and therefore, less multiple scattering, and reduced costs are advantages over classical hybrid pixelated silicon sensors [Ehr21].

A new potential field of application of the HV-CMOS technology is beam monitoring in medical irradiation treatments, as performed at the Heidelberg Ion Therapy Center (HIT). This facility offers medical irradiations of tumors for cancer patients with protons and charged ions, as helium, carbon, and oxygen [Hab+04]. The characteristic energy deposition of heavy charged particles in matter shows a sharp peak, referred to as Bragg peak, which is a valuable tool for radiation therapy due to the sharp localization and capability of sparing sensitive tissue around tumors. Precise monitoring of the initial beam throughout irradiation is essential for treatment success. Due to the high spatial resolution, fast response, low material budget, and cost, HV-CMOS sensors are in discussion as monitoring devices. The integrated HV-CMOS sensor ATLASpix3, studied in this thesis, was originally developed for the specifications of the outermost tracker layer of the ATLAS expected after the HL upgrade of the LHC. Therefore, it fulfills the requirements concerning readout speed and radiation hardness. With estimations of a lifetime dose for the fifth pixel layer in the upgraded ATLAS detector, a tolerance against a fluence of up to $3.8 \times 10^{15} \text{ n}_{\text{eq}}/\text{cm}^2$ is required [ATL17]. A distinction has to be made between radiation damage inside the bulk (non-ionizing radiation) and damage at the surface and the readout electronics (mainly ionizing radiation). Due to a bunch crossing rate of 40 MHz, ATLASpix3 was designed for a time resolution $\leq 25 \text{ ns}$ to assign the correct timestamp to the signals [ATL19]. A depletion zone of $\sim 50 \mu\text{m}$ and high in-pixel amplification result in large signals. The sensitive part of the matrix has a size of $20.2 \times 19 \text{ mm}^2$.

For a possible use of HV-CMOS sensors in beam monitoring, in prior studies, a stack of ATLASpix3 sensors was placed in the HIT beam dump. Due to a minimum beam width of 3.5 mm and higher rates of up to 2×10^{10} particles/s, the requirements at the HIT facility differ from the originally intended scope at the ATLAS experiment. The sensors were exposed to highly inhomogeneous irradiation with an HIT annual dose equivalent of protons and carbon

¹ATLAS – A Toroidal LHC Apparatus

²CERN – Conseil Européenne pour la Recherche Nucléaire (European Organization for Nuclear Research)

ions at energies around 110 MeV/u. In consequence, a reduced detection efficiency of charged electrons from a ^{90}Sr source, and increases in noise hits and leakage current were visible in studies by R. Schimassek [Sch21b]. To disentangle the different irradiation effects and study any impacts of damaged readout electronics, an irradiation with X-rays with the expected annual dose at the HIT was performed in this thesis. The impact on signal amplification was studied and the effects of the different radiation types were compared.

During the irradiation with a therapeutic carbon ion beam, charged nuclear fragments with high range are produced. Due to uncontrollable dose deposition, these secondary particles are highly unintentional. Still, the secondaries can be used for non-invasive and real-time monitoring methods [Gwo+13]. The method of secondary particle tracking can reduce uncertainties due to organ motion, tumor shrinkage, or other uncertainties in beam application [Kra15]. Previous studies from 2021 with the hybrid pixel sensor TimePix have demonstrated a potential fitness of this method for clinical applications [Fél+21].

The following work addresses the question of whether HV-CMOS sensors as ATLASpix3 are possibly suitable for the use in secondary particle tracking. A four-layer ATLASpix3 telescope was designed, built, and tested by R. Schimassek for earlier studies [Sch21b], and was now used for the purpose of secondary particle tracking at a beam test at HIT.

This thesis is organized as follows: In Chapter 2, the properties of the semiconductor silicon and the basics of particle detection with silicon sensors are presented. The HV-CMOS technology and the ATLASpix3 sensor are introduced in Chapter 3. Attention was put to the in-pixel signal readout process of ATLASpix3, the amplification, and possible damage. The original field of application in the high energy physics experiment ATLAS is outlined in Section 4.1. Section 4.2 introduces the field of medical radiation therapy, the irradiation facility HIT, the important field of beam monitoring, and the approach of secondary particle tracking as a method to increase precision during irradiation treatments.

An irradiation of an ATLASpix3 sample with X-rays was planned and conducted in the X-ray tube of the ETP³. The results are presented in Chapter 5. In addition, the suitability of ATLASpix3 for secondary particle tracking was tested. Therefore, a mechanical setup, capable of automated angle and distance adjustment, was developed, built, and used during a beam test at HIT. The mechanical setup and analyses of the data are presented in Chapter 6. The beam test data analysis framework *Corryvreckan* was used in the analysis [Dan+21].

A summary of the work is given in Chapter 7.

³ETP – Institute of Experimental Particle Physics at Karlsruhe Institute of Technology

2

Particle Detection with Silicon Sensors

As it is not possible to “see” or directly “measure” elementary particles, we depend on the interaction between particles of our interest and a certain detection material. The usage of the semiconductor material silicon led to huge improvements in detections methods in the last 50 years.

The following chapter will give a short introduction to the properties of silicon and the structures needed for the application as particle detectors. As radiation damage plays a role in this work, an introduction is given in section 2.4.

2.1. Physical Properties of Silicon

Since the early 20th century, applications based on semiconductor techniques have increased rapidly, the number of metal-oxide-semiconductor field-effect transistors (MOSFET) on microchips currently doubles every two years [RR20]. The huge range in electrical conductivity is a reason for a broad usage in industry and science.

Due to the large natural stock of insulating SiO₂, its non-toxic behaviour, and the mature production processes, the element silicon is commonly used as a semiconductor. This chapter describes the physical properties of the element silicon in Section 2.1.1 and the process of doping as a method of shaping the conduction properties of silicon (Section 2.1.2). The typical sensor element is a pn-junction, introduced in Section 2.1.3. The necessary readout electronics and circuits are implemented with transistors, described in Section 2.1.4.

2.1.1. Electronic Band Structure

The electronic properties of a material depend on the valence electrons. To obtain their energetic states, the Schrödinger equation must be solved, but with typical densities of 10²³ atoms per cm³, approximations are required. The periodic properties of a cristalline structure allow the description of the wave function as a plane wave, modulated by a periodic term $u_n(\mathbf{k}, \mathbf{r}) = u_n(\mathbf{k}, \mathbf{r} + \mathbf{R})$, referred to as Bloch waves:

$$\Psi_n(\mathbf{k}, \mathbf{r}) = e^{i\mathbf{k}\mathbf{r}} \cdot u_n(\mathbf{k}, \mathbf{r}) . \quad (2.1)$$

Here \mathbf{R} describes an integer multiple of the lattice vector and \mathbf{k} is the wave vector in reciprocal space. The parabolic dispersion of a free electron is perturbed by a periodic potential from the atoms in the lattice. This leads to correction terms that are aggregated to the effective mass m^* . The parabolic dispersion with m^* can be considered as valid for points of high symmetry:

$$E_{\text{kin}} = \frac{\hbar^2 \cdot \mathbf{k}^2}{2m^*} , \quad (2.2)$$

where \hbar is defined as the Planck constant. The band structure of silicon inside an elementary cell in momentum space - the first Brillouin zone - is shown in Figure 2.1. As the effective mass

depends on the direction of \mathbf{k} inside the Brillouin zone, the dispersion relation is plotted with several marked points of high symmetry.

The allowed ranges of energy states can be considered as quasi-continuous and are referred to as energy bands. The density of states per energy range reveals an energy gap of $E_g = E_c - E_v = 1.17$ eV for silicon at room temperature. Here E_c (conduction band) describes the lowest allowed energy state, not occupied in the ground state (temperature $T = 0$ K). The valence band, with a maximum energy of E_v , is the last fully occupied band. The occupation probability of the energetic states follows Fermi-Dirac statistics:

$$f(E, T) = \frac{1}{1 + \exp\left(\frac{E - \mu(T)}{k_B T}\right)}. \quad (2.3)$$

Here, k_B is the Boltzmann constant, and $\mu(T)$ denotes the temperature-dependent total chemical potential.

Depending on the band gap, materials can be assigned to three groups: metals, semiconductors and isolators. Materials with a band gap $0.5 \text{ eV} < E_g < 3 \text{ eV}$ are known as semiconductors, and silicon is a common representative of this class. An important property with regard to conductivity is the number of intrinsic charge carriers n_i . The higher the temperature, the more states in the conduction band are occupied and the higher the number of intrinsic charge carriers.

$$n_i \propto \left(\frac{k_B T}{2\pi\hbar^2}\right)^{3/2} e^{-E_g/2k_B T} \quad (2.4)$$

More detailed information about semiconductor physics can be found e.g. in [GM14].

2.1.2. Doping

W. Pauli once wrote in a letter to R. Peierls [Pau85]: “One shouldn’t work on semiconductors, that is a filthy mess [...]” It turned out, that adding even more “filth” – in form of certain impurities – is a valuable tool to regulate the number of free charge carriers and therefore the electrical conductivity of a semiconductor.

The crystalline structure of silicon is shown in Figure 2.2. Silicon belongs to the group of IV-semiconductors. It has four valence electrons and therefore crystallizes in a diamond cubic crystal structure by forming covalent bonds with the electrons of the neighbor atoms. If a donor with five valence electrons replaces one silicon atom of the lattice (Figure 2.2a), one electron is only loosely bound to the donor atom. These quasi-free electrons form additional energy states close beneath the conduction band edge and can easily be excited to the conduction band and then contribute to charge transport. Usually donors are elements from the fifth main group, as phosphorus, arsenic or antimony.

Figure 2.2b shows a boron atom built in substitutionally in the silicon lattice. This leads to the lack of an electron in the covalent bond and therefore results in an additional unoccupied state near the valence band. This unoccupied state can be described as a quasiparticle, referred to as hole with positive charge and negative effective mass.

In total, the doped material stays electrically neutral, based on the charge neutrality condition:

$$N_D^+ + p = N_A^- + n \quad . \quad (2.5)$$

Here N_D^+ and N_A^- denote the density of stationary charged donor or acceptor atoms and n/p are the densities of negative/positive (electrons e^- /holes h^+) free charge carriers.

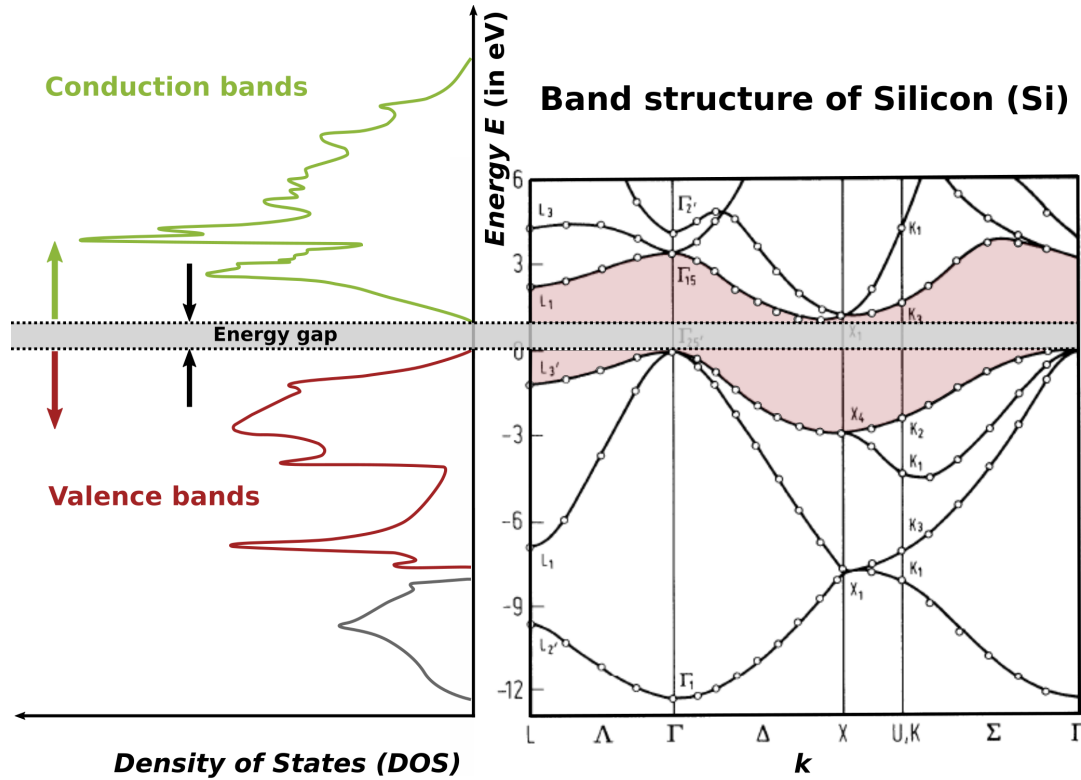


Figure 2.1.: Band structure and density of states in silicon – The right plot shows the band structure of the indirect semiconductor silicon in the first Brillouin zone with a band gap $E_g = 1.17$ eV. On the left side the density of states is outlined. The valence bands (red) are the last fully occupied bands at room temperature. The energy states in the conduction band (green) are occupied only above the ground state. (adapted from [MRS02; Bre11])

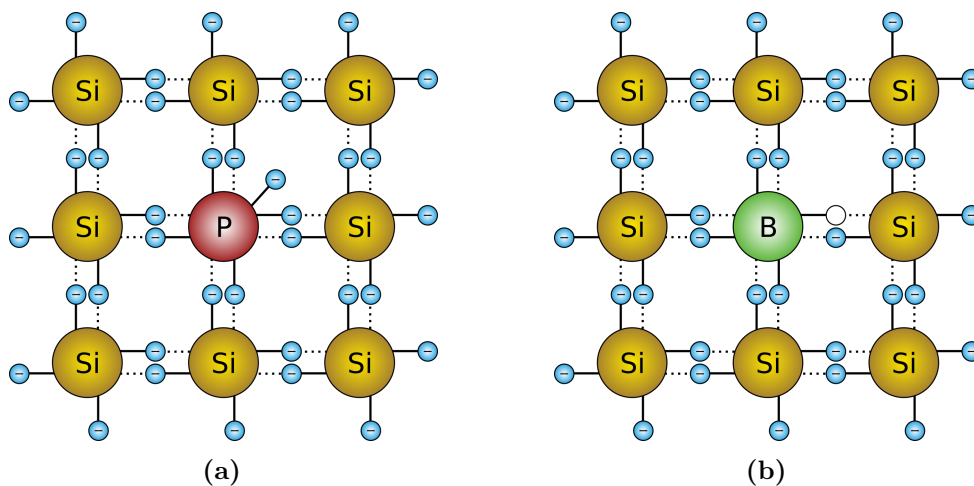


Figure 2.2.: Doping of a silicon crystal – The systematic addition of impurities in semiconductors changes the intrinsic behavior. (a) n-doping with phosphorus leads to an additional valence electron. (b) p-doping with boron results in a missing electron and hence an unoccupied state. (adapted from [Hen06])

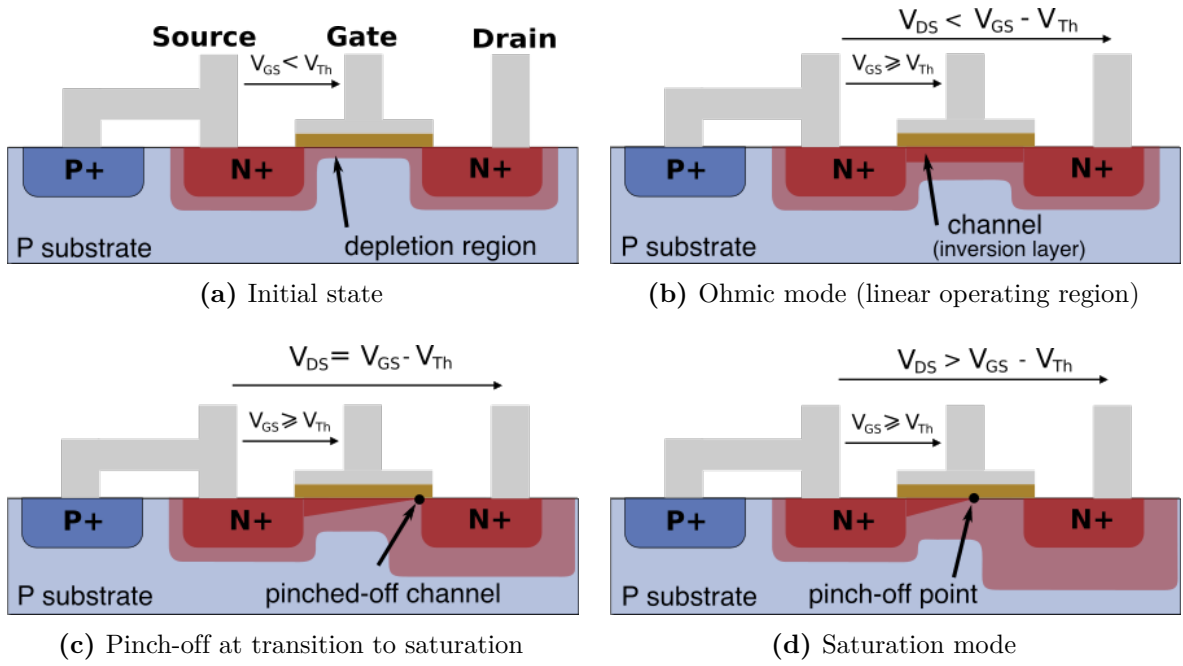


Figure 2.3.: The operation modes of an n -MOSFET – adapted from [DS08]

2.1.3. pn-Junction

An effective particle detector should have the highest possible signal to noise ratio (SNR). This leads to two opposing requirements. On the one hand a low ionization energy for large signals is favorable, but too small band gaps would also lead to a large increase of free charge carriers in the conduction band and would therefore result in high noise. The typical signal is several orders of magnitude smaller than the number of thermally produced e^-h^+ -pairs. To measure the signal, a reduction of free charge carriers in the detection material becomes necessary, realizable with a pn-junction.

To form a pn-junction, two oppositely doped semiconductors are brought together. The high density gradient in charge carriers is compensated by diffusion currents - electrons from the n -doped region recombine with the holes from the p -doped region and vice versa. This leads to a depletion zone without free charge carriers. The exchange of diffusion currents takes place until a thermodynamic equilibrium is set.

With help of the Schottky approximation and solving of the Poisson equation the width of the depletion zone w can be calculated [Thu18]. The width is directly proportional to the diffusion voltage U_D , an intrinsic characteristic of the semiconductors doping, which typically has values around 0.7 V.

$$w = x_n + x_p = \sqrt{\frac{2\epsilon\epsilon_0}{q} \cdot \frac{n_A + n_D}{n_A \cdot n_D} \cdot (U_D - U_{\text{ex}})} \quad (2.6)$$

Depending of the polarity, an additional external voltage U_{ext} leads to an increase or decrease of the depletion zone.

2.1.4. The Metal Oxide Field Effect Transistor (MOSFET)

For highly integrated circuits, the MOSFET is the most important component. In general, it is a voltage driven resistor with a nearly powerless gate control. The general structure and the

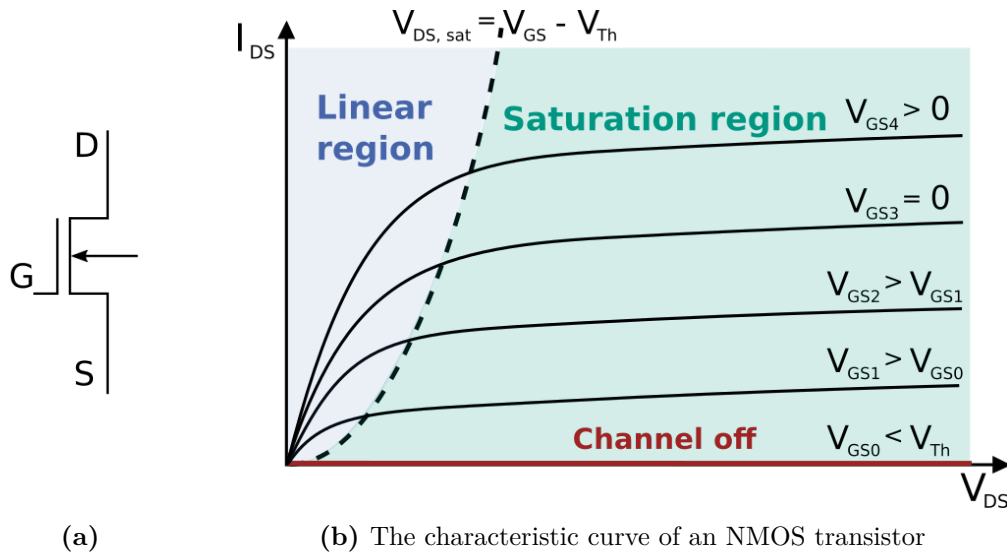


Figure 2.4.: The circuit symbol and the characteristic curve of an NMOS transistor – (a) The symbol of an NMOS transistor, (b) The plot depicts the operation modes of a MOSFET with the characteristic curve for five different $V_{GS,i}$. (adapted from [Phi09])

three operation modes of an NMOS transistor with an n -channel are described along Figure 2.3 [Thu18; Sau10]:

- (a) Two strongly n -doped wells – source (S) and drain (D) – are implemented in a lightly p -doped substrate and the pn-junctions form depleted regions. The gate (G) is isolated from the substrate via a layer of SiO_2 (in brown) which covers the zone between the N^+ -regions. The electrical contact at the gate is normally realized with highly doped conducting polycrystalline silicon, instead of metal due to the similar lattice. As long as the voltage V_{GS} between the gate and the source is beneath a threshold voltage V_{Th} , no charge transport is possible due to a lack of charge carriers.
- (b) With increasing V_{GS} the minority charge carriers of the p -substrate (electrons) wander off to the MOS junction. Here the electrons recombine with the majority charge carriers of the p -substrate, the holes. If V_{GS} exceeds the threshold V_{Th} , an inversion layer building an n -channel forms. The channel expands for a growing drain-source voltage V_{DS} and the current I_{DS} increases linearly in the ohmic mode. The linear increase can be seen in Figure 2.4b.
- (c) As the voltage V_{DS} keeps growing, the effective gate voltage is decreasing towards the drain contact (Figure 2.3c). As a result the current I_{DS} saturates as soon as the channel is pinched off at the N^+ -region of the drain. This is the case if V_{DS} exceeds $V_{GS} - V_{Th}$.
- (d) For $V_{DS} > V_{DS, sat}$ the pinch-off point wanders towards the source contact, reducing the channel length. The voltage drop of the growing V_{DS} over the p -conducting region leaves I_{DS} to be constant. The drain-source current I_{DS} in dependency of the voltage U_{DS} is shown in Figure 2.4.

As only one type of charge carrier contributes to the charge transport, this transistor is a unipolar device. A PMOS transistor is realized with inversed doping types.

Further beneficial properties of MOSFETs are the high impedance, useful for amplification circuits, and the small sized components. The channel length L describes the distance of the N^+ -wells in the MOSFET and needs to be small for a high packing density in ICs. In the beginnings of ICs the channel length had values of several $10\ \mu\text{m}$ but has decreased exponentially over the last years.

CMOS Technology The complementary metal-oxide-semiconductor (CMOS) technology is a common semiconductor manufacturing process, using complementary and symmetrical pairs of NMOS and PMOS transistors for logical functions. Placing both types of transistor in same substrate keeps the processing simple and cheap. A basic device is the CMOS inverter – also known as NOT gate – built with a duality of a PMOS and an NMOS transistor. Apart from the switching state, one transistor is always off and the power consumption is rather low. [Fai83]

2.2. Interaction of Particles with Matter

To understand the working principle of silicon sensors, the interaction processes of particles traversing matter have to be understood. A differentiation between several particle types, their mass, charge, and initial energy has to be made. Also the properties of the traversed material and its thickness play an important role for the energy deposition. The following section only describes the processes relevant for this work. [Dem14; KW16] are recommended for further information on this topic.

2.2.1. Generation of Charge Carriers in Silicon

The fundamental principle of signal generation in a silicon sensor is the generation of electron-hole pairs in the depleted region of the semiconductor via ionization or absorption processes. A huge advantage of silicon sensors over e.g. gas proportional chambers is thereby the low ionization energy of $I = 3.62\ \text{eV}$. This energy is necessary for the direct transition of electrons at $\mathbf{k} = 0$. The value lies above the band gap ($E_{g, \text{Si}} = 1.17\ \text{eV}$) as silicon is an indirect semiconductor.

Apart from particle properties such as mass and charge, statistical fluctuations of energy deposition are relevant in signal detection. The low number of ionized charge carriers in thin sensors results in a big uncertainty according to Poisson statistics. Also, the energy transfer of each individual process is not free of fluctuations. The asymmetric Landau distribution considers these uncertainties and describes the statistical fluctuations of energy loss in thin sensor layers [KW16]:

$$f_L(\lambda) = \frac{1}{\pi} \int_0^\infty e^{-t \ln(t-\lambda t)} \sin(\pi t) dt. \quad (2.7)$$

The mean energy loss $\bar{\lambda}$ is no good measure of the localization of the distribution because of the non-neglectable tail for large λ . Instead, the most probable value (MPV) is used to describe the localization.

2.2.2. Interaction Processes of Charged Particles

For the detection of particles in silicon sensors mainly electromagnetic interactions with e.g. charged particles are relevant. Here, the dominating interaction process depends on the particle's mass. A distinction between heavy charged particles (e.g. hadrons) and electrons has to be made.

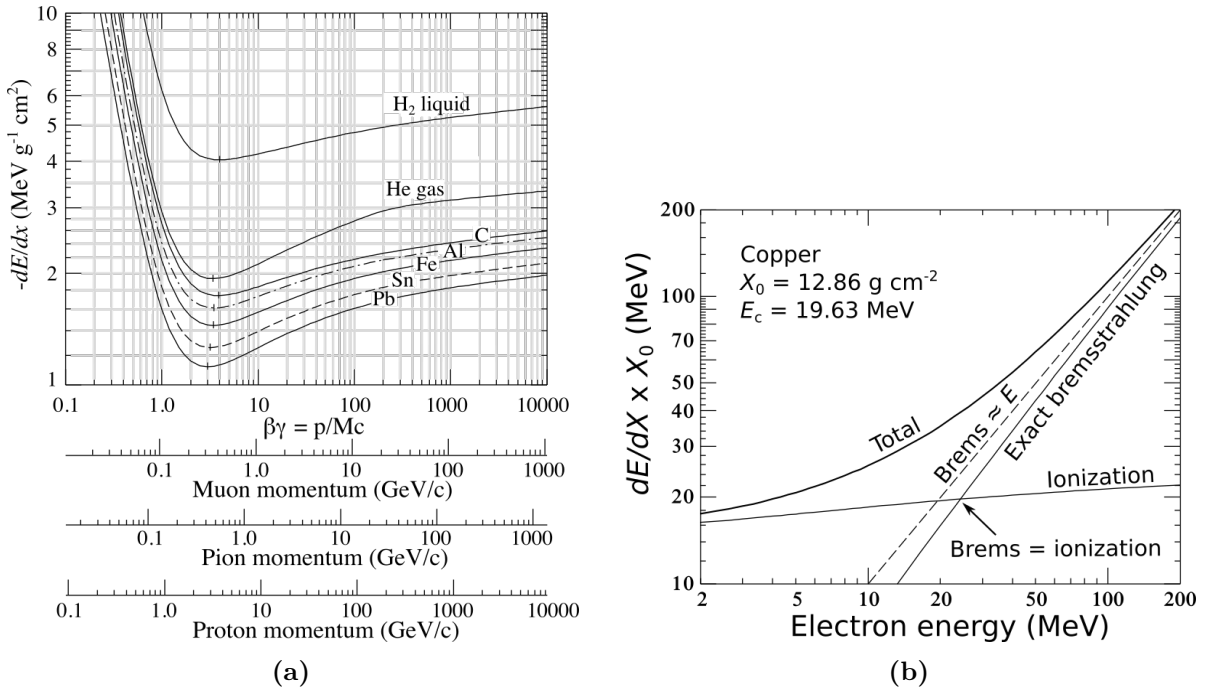


Figure 2.5.: Energy deposit of charged particles in matter – (a) The mean energy loss rate of several hadrons in different material according to the Bethe equation. The approximation is only valid in the region $0.1 \leq \beta\gamma \leq 1000$. (b) The energy loss of electrons in copper. Ionization processes dominate for energies below 20 MeV and bremsstrahlung above. (both plots adapted from [Zyl+20])

Heavy Charged Particles

The main interaction process of heavy, charged particles is ionization. In this case, the mean energy loss dE per traversed distance in matter dx is described by the Bethe equation:

$$-\left\langle \frac{dE}{dx} \right\rangle = 4\pi N_A r_e^2 m_e c^2 \frac{Z_p^2 \cdot Z_t}{A} \frac{1}{\beta^2} \left[\frac{1}{2} \ln \left(\frac{2m_e c^2 \beta^2 \gamma^2 T_{\max}}{I^2} \right) - \beta^2 - \frac{\delta(\beta\gamma)}{2} - \frac{C}{Z_t} \right] \quad (2.8)$$

N_A	Avogadro number	β	Velocity relative to the speed of light
r_e	Classical electron radius	γ	Lorentz factor
m_e	Electron mass	T_{\max}	Maximum kinetic energy transferred to the electron in a single collision
c	Speed of light	I	Average excitation energy
Z_p	Charge of projectile particle	$\delta(\beta\gamma)$	Density effect correction for high $\beta\gamma$
Z_t	Atomic number of target matter	C/Z_t	Shell correction term for low $\beta\gamma$
A	Mass number of the matter		

Figure 2.5a shows the energy deposition according to equation (2.8) for hadrons in different material. The equation is only valid in the Bethe region ($0.1 \leq \beta\gamma \leq 1000$). Below and above this range, the necessary approximations are not valid any more [Zie99; KW16]. The course of the Bethe curve (eq. 2.8) shows a minimum around $\beta\gamma \approx 3$, depending on the material. Particles with energies near this minimum are referred to as minimum ionizing particles (MIPs).

While a particle traverses matter, the energy of this particle is absorbed continuously by statistical interaction processes. As the particle's energy decreases the energy loss is increasing. The dependency of the Bethe equation on β^{-2} results in a sharp peak in the energy deposition in matter at the end of the particles range. The typical curve of the energy deposition is

referred to as Bragg curve and this property makes heavy charged particles interesting for medical applications. In Chapter 4.2 the principle of radiation therapy in cancer treatment is introduced.

Electrons and Positrons

Figure 2.5b illustrates the energy loss of electrons in copper. Due to their small masses, the scattering in the Coloumb field of the atomic hull cannot be neglected for electrons. This interaction process resembles Rutherford scattering with emission of a Bremsstrahlung photon. Besides ionization the effects of Bremsstrahlung have to be considered in the energy deposition:

$$\frac{dE}{dx} = \left(\frac{dE}{dx}\right)_{\text{ion}} + \left(\frac{dE}{dx}\right)_{\text{rad}} . \quad (2.9)$$

Depending on their initial energy, different processes are dominant for the interaction. As the power of emitted Bremsstrahlung is proportional to E/m^2 low energetic electrons mainly lose their energy via ionization. In copper this transition takes place at around 20 MeV.

In this thesis, the low energetic electrons produced at the β^- decay of a ^{90}Sr source are used in the measurements. The energy deposition of these electrons corresponds to that of an MIP.

2.2.3. Interaction Processes of Neutral Particles

Photons

Although photons are neutral particles, they interact via the electromagnetic force. Therefore they are relevant for detecting processes in silicon sensors. Figure 2.6 shows the contributions of different effects to the total interaction. Inelastic or elastic scattering processes with nuclei, electrons or magnetic fields can occur. Depending on the photon's energy, one of three cross sections dominates [Dem14]:

- $E_\gamma \lesssim 100 \text{ keV}$: For small energies, the photoelectric effect dominates. Photons are fully absorbed by an atom, which emits a shell electron if the binding energy is overcome. For the recoil matter must be present for the conservation of momentum.
- $100 \text{ keV} \lesssim E_\gamma \lesssim 20 \text{ MeV}$: The Compton effect is an inelastic scattering effect of photons with quasi-free electrons in outer atomic shells. The energy of the photons has to be larger than the binding energy of the electron, which is excited into a free state. The photon continues traversing the matter with altered energy and angle.
- $E_\gamma \gtrsim 20 \text{ MeV}$: Pair production takes place for photon energies above $2 \times 511 \text{ keV}$. In this process, a photon is converted into an electron-positron pair. This process can only take place in the presence of a nucleus or an electron to absorb the recoil and conserve momentum. As the Feynman diagrams of Bremsstrahlung and pair production are variants of one another, the energy scales of the cross sections are highly related.

In general, the energy of optical photons is too low for ionizing the silicon lattice, unlike x-rays with energies of several keV. In case of an interaction in the silicon sensor substrate, the energy of the photon is fully absorbed [Ehr21]. The energy loss of mono-energetic photons therefore resembles a Gaussian shaped distribution.

Neutrons

Even though the energies of neutrons would be sufficient for ionization processes in most applications of high energy physics, hardly any electron-hole production takes place in silicon, due to their electrical neutrality. As the detection of neutrons can become essential in several

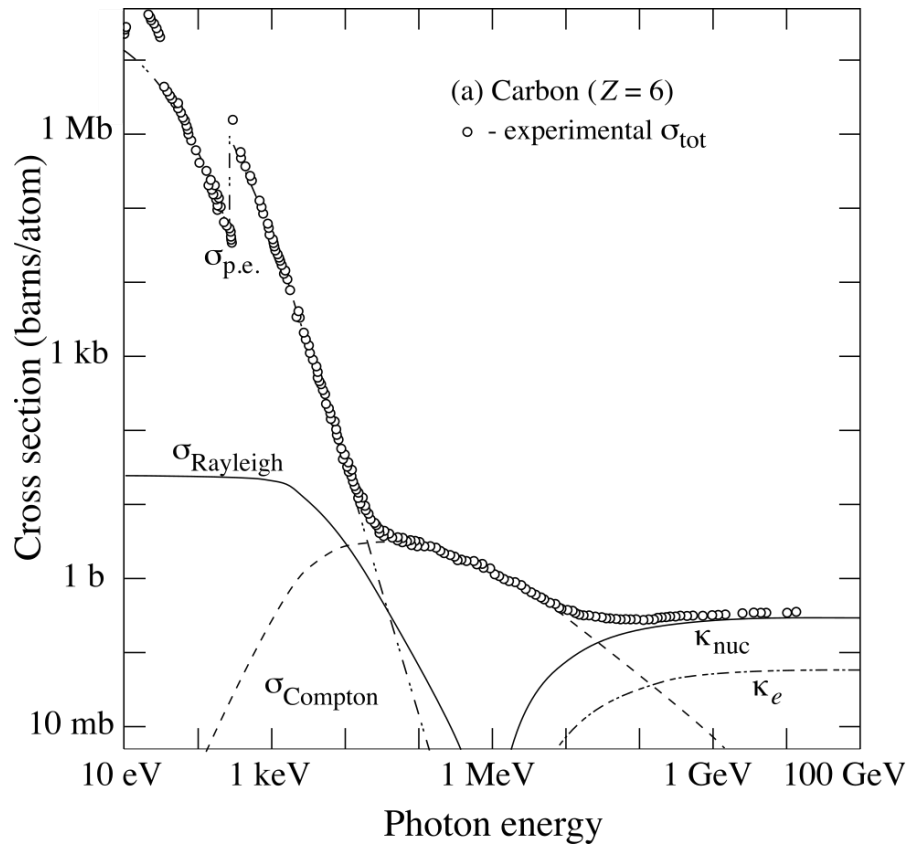


Figure 2.6.: Cross sections of photons in matter – Dominant cross sections of photons in matter at different energies are combined to a total cross section, which fits the measured data. (from [Zyl+20])

application fields, moderators can be useful. Inside the moderator, interaction (scattering) processes take place, producing charged particles such as protons. Suitable moderators depend on the initial energies of the neutrons. ${}^6\text{Li}$ or ${}^3\text{He}$ can be used for low energetic neutrons, whereas materials with high amounts of hydrogen (e.g. polyethylene (PE)) are used for the conversion of fast neutrons [Jak+11; Dem14]. Neutrons can also be absorbed by nuclei. This leads to a deexcitation by emission of radiation or even fission of a heavy nucleus in smaller charged fragments. Their charge then allows detection with silicon sensors and conclusions about the initial neutrons. Furthermore neutrons play a role in radiation damage processes, addressed in section 2.4.

2.2.4. Multiple Scattering in Thick Layers

Apart from the properties as mass and atomic numbers of the target material also the distance traveled is relevant for interactions. After traversing a material of a certain thickness, the particle has interacted many times, resulting in a statistical distribution of the scattering angle relative to the initial direction. According to the central-limit theorem for an infinite number of scattering events, a pure Gaussian distribution would be expected. Molière successfully approximated the angular distribution from multiple Coulomb scattering ($n > 20$) with a Gaussian distribution and a standard deviation θ_0 [Ahl80; LD91]:

$$f(\theta | \theta_0) = \frac{1}{\sqrt{2\pi} \cdot \theta_0^2} \cdot \exp\left(-\frac{\theta^2}{2 \cdot \theta_0^2}\right)$$

$$\text{with } \theta_0 = \frac{13.6 \text{ MeV}}{p \cdot v} \cdot Z_t \cdot \sqrt{\frac{X}{X_0}} \cdot \left[1 + 0.038 \cdot \ln\left(\frac{X}{X_0}\right)\right] \quad (2.10)$$

θ	Scattering angle from initial axis	θ_0	Standard deviation of the Gaussian approximation
X	Path length in material	Z_t	Charge of scattering material (target)
X_0	Radiation length in $\text{g}\cdot\text{cm}^{-2}$	v	Velocity of traversing particle in c
p	Momentum of particle in MeV/c		

This Gaussian distribution is only valid for small scattering angles. For large angles the consideration of the Rutherford cross section of a single Compton scattering event becomes relevant. Therefore the tails of the scattering angle distribution follow $\sim 1/\sin^4(\theta/2)$ with stronger contributions to larger angles than the pure Gaussian distribution.

2.3. Working Principle of Silicon Sensors

The working principle of a silicon sensor is illustrated in Figure 2.7. A lightly p-doped silicon substrate builds the bulk of the sensor. Strongly n-doped wells are implemented in the material, forming a pn-junction with a depleted region. Polysilicon contacts are used for the signal readout.

When charged particles traverse the sensor bulk, electron-hole pairs are generated. These free charge carriers drift towards the electrodes in the intrinsic electric field of the pn junction and a depletion voltage. The typical time scales of the signal production in silicon are several nanoseconds, therefore, silicon sensors can be considered fast. At the contacts, the charge is read out via an capacitively (AC) coupled readout system. The signal is amplified and digitized by the readout electronics. The number of electron-hole pairs generated by a MIP in the depleted zone $d = 50 \mu\text{m}$ of a HV-CMOS sensor can be estimated with the MPV for the

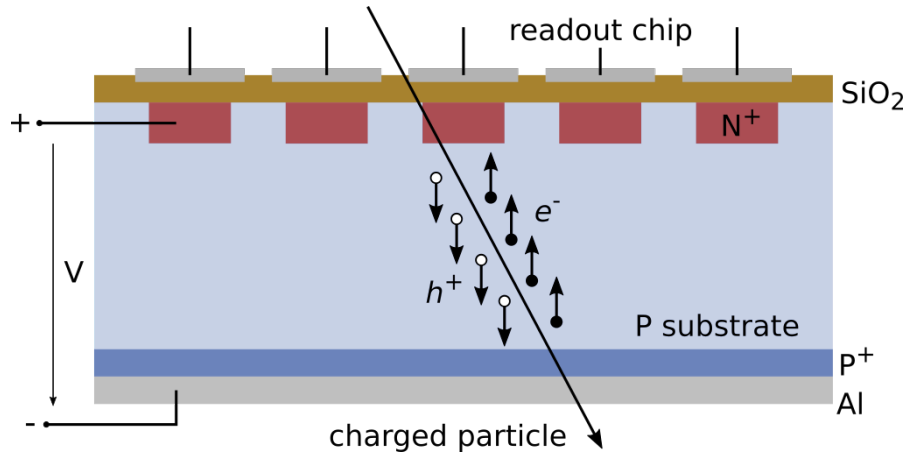


Figure 2.7.: Working principle of silicon sensors explained on a p-type strip sensor
 – As a charged particle traverses the lightly p-doped bulk material of the sensor, electron-hole pairs are generated by ionizing processes. The charge carriers are separated by the electric field and drift towards the collection electrodes. The readout electronics amplify, digitalize and pass on the induced charge from the N-wells for further processing. (adapted from [Dro18])

energy loss dE/dx in silicon [Har17]:

$$N = \frac{dE}{dx} \cdot \frac{d}{E_{\text{ion}}} = 390 \frac{\text{eV}}{\mu\text{m}} \cdot \frac{300 \mu\text{m}}{3.62 \text{ eV}} \approx 5400. \quad (2.11)$$

A detector has to be sensitive enough for the detection of a MIP traversing the sensor bulk vertically, right in between two strips, as this is the “worst case scenario” for particle detection. The spatial resolution of a silicon sensor depends on its segmentation. For a sensor with a pitch p it is given by:

$$\sigma_x^2 = \frac{1}{p} \int_{-p/2}^{p/2} x^2 dx = \frac{p^2}{12} \Rightarrow \sigma_x = \frac{p}{\sqrt{12}}. \quad (2.12)$$

This resolution can be improved by charge sharing effects. If the signal width exceeds the segmentation width of the sensor, the signal can be approximated as a Gaussian distribution and the center of gravity (c.o.g.) can be determined. This leads to a more precise coordinate measurement with an increased resolution.

$$\left(\frac{\sigma_x}{p}\right)^2 = \frac{1}{2\pi^2} \sum_{m=1}^{\infty} \frac{\exp(-4\pi^2 m^2 (\sigma/p)^2)}{m^2} \quad (2.13)$$

Here σ/p describes the width of the signal in units of the pitch. Further information on silicon sensors in more depth and general is provided in [Har17] and [KW16].

2.4. Radiation Damage

In applications of silicon sensor, high particle rates are often important for sufficient statistics or sometimes simply inevitable. This leads to a large energy deposition in the detection material and defects in the atomic structure. A distinction has to be made between damage inside the bulk and damage at the surface. These effects will be discussed in the following.

The information on radiation damage in the bulk is taken from [Har17] and [KW16], if not stated otherwise. More information on surface damage in MOS structures is provided in [Bor18] and [Sch+08].

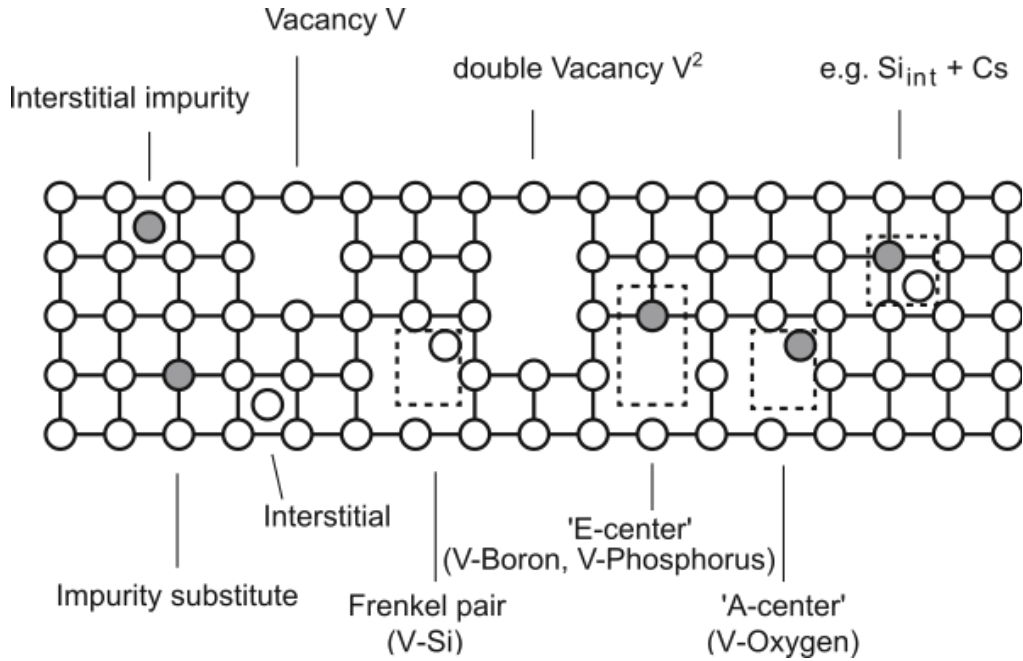


Figure 2.8.: Types of Bulk Damage – Atomic displacements in the silicon lattice. (translated from [KW16])

2.4.1. Bulk Damage

The main problem for classical silicon sensors are displacement damage and crystal defects induced by Non Ionizing Energy Loss (NIEL). As ionizing is a reversible effect in semiconductors, mainly non-ionizing radiation is problematic for the bulk. The NIEL-scaling hypothesis is a method to correlate and unify the experimental data in irradiation studies. The energy transfer to the atomic lattice is assumed to be purely non-ionizing, and the fluence is converted into the damage induced by neutrons at an energy of 1 MeV, the neutron equivalent n_{eq} . As an example, the fluence Φ_{eq} for the fifth pixel detector layer of the upgraded ATLAS detector at the CERN LHC (Section 4.1) after ten years of the high luminosity upgrade is estimated to be $\Phi_{eq} \approx 10^{15} n_{eq}/\text{cm}^2$ [Sch21b].

Typical defect types are illustrated in Figure 2.8. Additionally, cluster defects can occur where defects combine. These defects create new energy levels in the silicon bandstructure and change the fundamental properties of the material. Typical effects are an increase of leakage current, type inversion of the substrate and therefore a change in the necessary depletion voltage, and charge trapping effects. These effects lead to a decrease of the charge collection efficiency. Some defects recombine over time, which is referred to as annealing and can be sped up at increased temperatures (typically $60^\circ\text{C} - 80^\circ\text{C}$), whereas cooling suppresses annealing effects.

2.4.2. Surface Damage

In this thesis the SI unit gray (Gy) is used to describe the total absorbed ionizing dose per absorber mass:

$$1 \text{ Gy} = 1 \frac{\text{J}}{\text{kg}} \quad . \quad (2.14)$$

Due to the amorphous structure of the SiO_2 displacement is no primary damage effect. Instead, the generation of electron-hole pairs by ionizing particles is no reversible process as in the

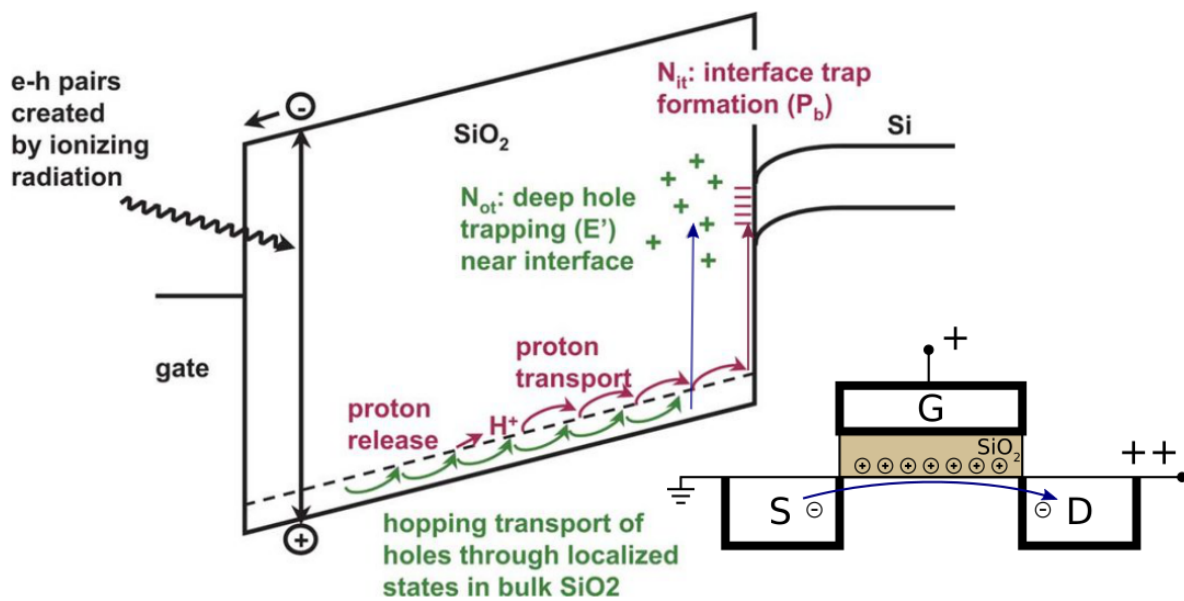


Figure 2.9.: Radiation induced charge generation in the band diagram of a MOS capacitor – The left plot shows the band diagram of a MOS transition. The p-doped silicon is connected to SiO₂. Ionizing radiation leads to the generation of electron-hole pairs and the formation of trapped charges near and at the interface of SiO₂ and silicon. In the right plot, an NMOS transistor with positive surface charges in the SiO₂ is shown. High densities of surface charges lead to a transport of negative charge carriers in the *n*-channel of the transistor, even though the conduction conditions are not fulfilled. (adapted from [Sch+08])

semiconductor bulk and therefore problematic. The typically strong fields in MOSFETs below the gate prevent electron-hole pairs from direct recombination. As the mobility of electrons is up to 10^6 times higher than the one of holes in SiO_2 , electrons drift of to the gate very fast, leaving positive stationary charges. There are two main types of radiation-induced charge effects in the oxide [Sch+08]:

1. **Oxide-trapped charge:** Electron-hole pairs generated by ionizing radiation are separated by the external field and the holes wander towards the SiO_2 -Si interface due to the positive voltage V_{GS} . The mobility μ_{h} of the holes is strongly decreased by trapping effects, leading to positive oxide-trap charges near the interface. This charge is neutralized fast by electrons tunneling into the oxide or by thermally excited electrons from the valence bands in the SiO_2 .
2. **Interface-trapped charge:** During the production of MOS structures, hydrogen atoms are used to passivate dangling bonds between silicon bulk and SiO_2 due to differences in the lattice structure [Tse+07]. The bonding of these H-atoms is not strong and H^+ -ions are easily released by hopping holes and react to interface traps. While the former effect is likely to be neutralized, interface-trapped charges are rather stable ($\sim 10^3$ s). Both effects are illustrated in Figure 2.9.

Positive charge carriers near the surface lead to leakage currents (as depicted in Figure 2.9) and can result in cross talk between individual pixels, a reduction of the SNR and the prevention of valid switching states of the transistor as it is always conducting [Ehr15].

The charges induced by radiation and the radiation effects of the conduction properties depend on the transistor type. The induced oxide-trapped charges are positive in case of an NMOS transistor (Figure 2.9), and the building of an n-channel is supported. Therefore, the effective threshold of the transistor is reduced and it becomes permanently conductive at a certain point. For PMOS transistors the threshold is increased, therefore, this type is less prone to radiation effects. In general the development of smaller structures is beneficial for better radiation hardness. Oxide layers with few nanometers thickness enable tunneling of holes into the substrate and prevent charges from being trapped. Also, variations in the design of transistors have favorable effects. Leakage currents in NMOS structures, which can bypass the gate in the linear layout (2.10a), are strongly suppressed in an annular design (2.10b). This also prevents unintended switching effects in adjacent transistors [KW16].

While bulk damage is the dominant radiation damage effect in classical silicon sensors, with smaller and more complementary structures, surface damage becomes more important. This is the case for monolithic sensor devices as HV-CMOS sensors (Chapter 3).

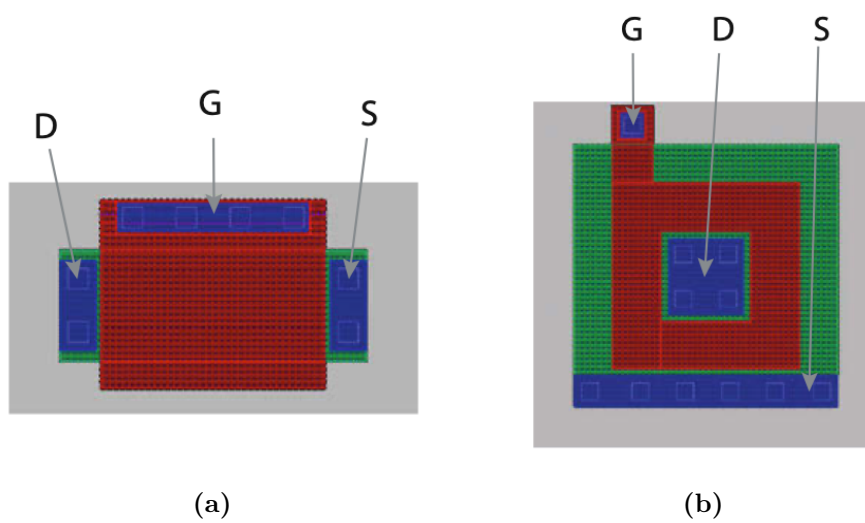


Figure 2.10.: Layout types of a MOSFET transistor – A MOSFET consists of a drain (D - green), a source (S - green), a gate (G - red) and metal contacts (blue). Two different geometrical layouts are shown in this sketch: The linear layout (a) is the classical layout. A annular layout (b) improves the radiation hardness by suppressing leakage currents due to trapped interface charges in the oxide. (from [KW16])

3

Applied HV-CMOS Technology

Today, silicon sensors are undisputedly one of the most important detection technologies for high-energy physics (HEP) and are constantly being further developed. The High Voltage Complementary Metal-Oxide-Semiconductor (HV-CMOS) technology concept, invented by Ivan Perić in 2007, represents a further leap in this development [Per07]. This chapter describes the principle of hybrid sensors and the advantages of monolithic sensors over hybrid pixel sensors, the development of fully depleted HV-CMOS devices and an example of this sensor technology, studied in this work: the ATLASp3 sensor. The readout process of the ATLASp3 and possible radiation damage in the readout chain are discussed.

3.1. Classical Hybrid Silicon Sensors

The basic working principle of silicon sensors is the same for all sensor types and was described before, in Section 2.3. In a classical hybrid pixelated layout, the sensor bulk and the readout electronics are separate devices, connected via bump bonds (Figure 3.1a). A wide depletion zone due to high applicable bias voltages leads to large signals. Also, sensor and electronics are each highly optimized and hybrid sensors have already distinguished themselves useful in many HEP experiments.

Yet, there are disadvantages of the hybrid technology. As a layering of sensor bulk, bump bond and ASIC is necessary, the material budget (X/X_0) is rather high. Multiple scattering is problematic for precise determination of particle trajectories. In addition, they have a high power consumption and are expensive in production, especially as the bump-bonding process is no standard technology. The approximated cost of sensor, readout chip and assembly per square meter of the CMS pixel detector is 2.1×10^6 € [Ehr21].

3.2. Principle of Monolithic Active Pixel Sensors

The principle of monolithic active pixel sensors (MAPS) was developed in the 1970s and today this technique is widely spread e.g. in camera applications [TSD15]. The idea was to implement the readout electronics directly in the substrate of the sensor diode. This is a standard low-voltage CMOS process and can be realized easily and at low cost. The power consumption is low and due to fully analog signal processing in the matrix and outsourced switching operations to the periphery, the low cross talk between pixels leads to low noise. Thin substrates ($d \sim 50 \mu\text{m}$) reduce multiple scattering effects but also the generated signal ($\sim 80 e^-/\mu\text{m}$ – see Equation 2.11). A disadvantage of this technology is the low applicable voltage because of the sensitive transistors. The signals are generated in a lowly doped bulk and a depletion of the whole sensor material and a charge separation via an external electric field is not realizable. The signal is collected via diffusion in the substrate and a drift in the field of the pn-junction near the electrodes. Therefore, the signal is rather small and slow (~ 100 ns) and the lack of applied voltage also affects the radiation hardness [dS87; KW16]. Especially

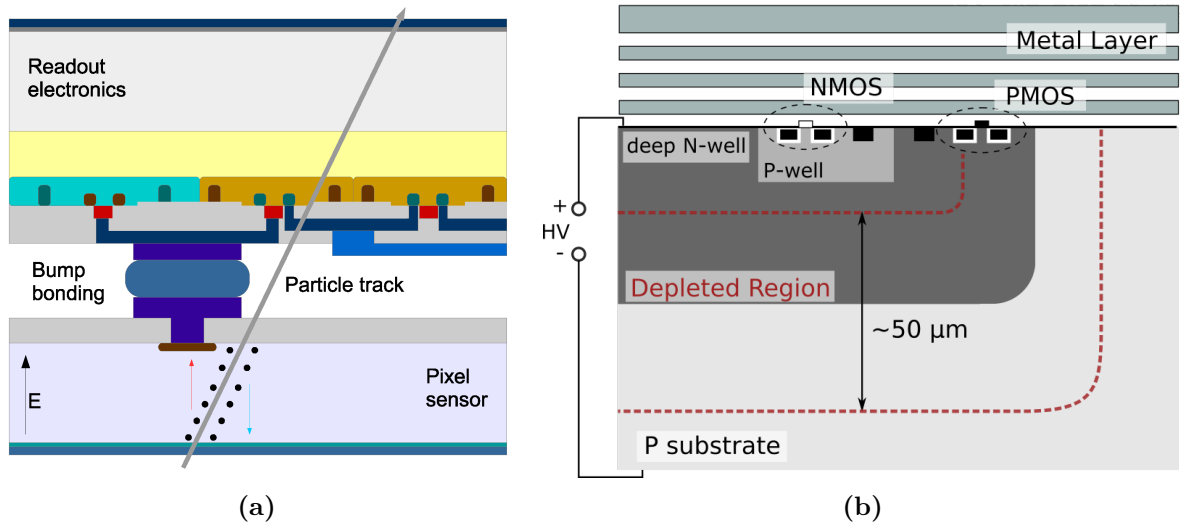


Figure 3.1.: Comparison of a hybrid and monolithic pixel sensors – (a) Diagram of a hybrid pixel detector: In the hybrid layout, the separated readout electronics and the sensor bulk are connected via a solder contact, referred to as bump bond. (from [Mar20]) (b) Schematic of a monolithic HV-CMOS sensor: The transistors needed for the readout electronics are directly implemented in the sensor substrate and protected by a deep N-well, which doubles as a collection electrode. (from [Sch16])

the slow charge collection and the lack of radiation hardness makes this sensor technology insufficient for large HEP experiments like CMS or ATLAS.

3.3. Principle of Monolithic HV-CMOS Sensors

The first steps in solving these problems were the studies on a high voltage MAPS (HV-MAPS) by Ivan Perić in 2004 [Per04], which led to the invention of a HV-CMOS pixel sensor in 2007 [Per07], enabling the realization of the Mu3e experiment¹. Here the pixel electronics are placed into a lowly n -doped deep N-well, making the combination of low- and high-voltage processes possible. The sensitive small transistors are protected by the deep N-well and the high voltage devices enable depletion voltages up to 120 V [Kie+18]. Metal layers above the embedded structures establish the connections between the elements. A schematic of the depleted monolithic HV-CMOS sensor is shown in Figure 3.1b. These improvements lead to fast charge separation and collection via drift in the $\sim 50 \mu\text{m}$ thick depletion zone, a timing resolution of $\sim 1 \text{ ns}$ and improved radiation hardness of up to $10^{15} \text{ n}_{\text{eq}}/\text{cm}^2$. As the depletion zone is rather thin compared to the one of classical sensor, charge sharing effects can be neglected for this sensor type.

A further advantage is the largely reduced cost of $84.1 \times 10^3 \text{ €/m}^2$, compared to hybrid sensors [Ehr21]. More information on this topic can be found in [Per+21].

¹The Mu3e experiment will search for the decay of a muon to three electrons at the Swiss Paul Scherrer Institute [WB19].

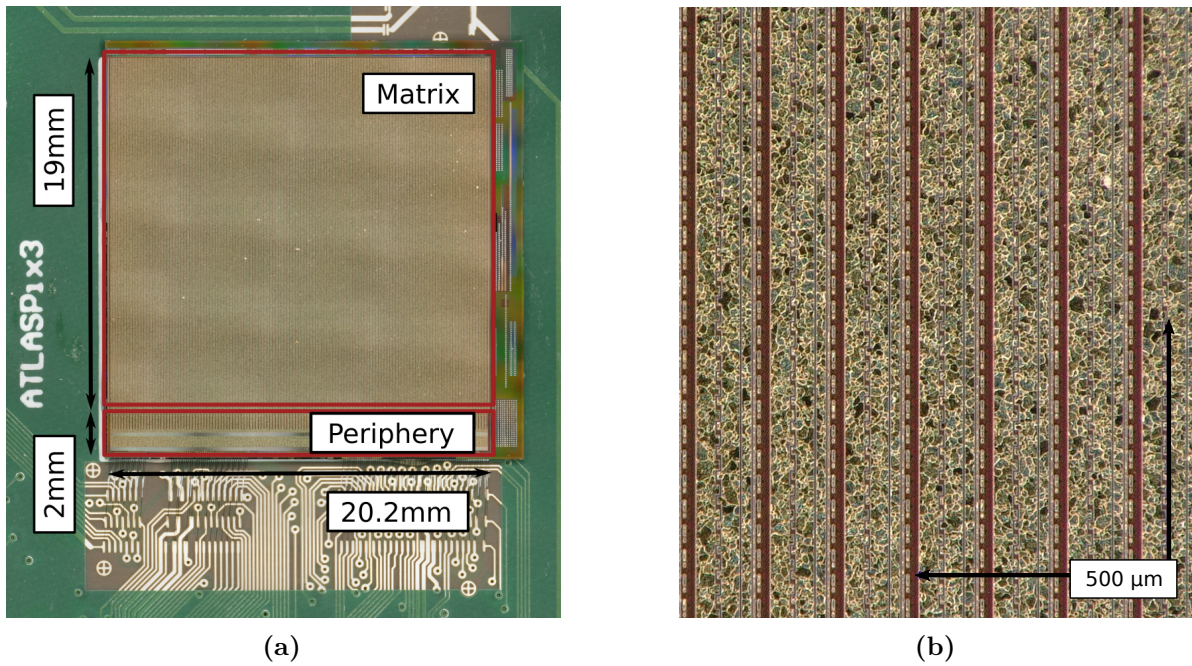


Figure 3.2.: Magnified images of the ATLASp3 sensor – (a) The chip – consisting of a sensor matrix and the periphery – is wire-bonded on a circuit board. (b) The structure of the sensor surface and the segmentation of the rows and columns are visible.

3.4. Integrated Sensor: ATLASp3

The integrated sensor ATLASp3 was designed to meet the specifications of the outermost pixel layer of the ATLAS inner tracker (ITk) for the HL-LHC (Section 4.1). It is the first fully depleted monolithic HV-CMOS pixel detector with full reticle size. The matrix has a size of $19\text{ mm} \times 20.2\text{ mm}$ with a fill factor² of 100%. The adjacent periphery is not sensitive and has a share of 10% of the area. A picture of the chip bonded on a printed circuit board (PCB) is shown in Figure 3.2a. The matrix is made of 372 rows and 132 columns, resulting in 49 104 pixels with a size of $50\text{ }\mu\text{m} \times 150\text{ }\mu\text{m}$. More information on the layout of the ATLASp3 is provided in [Sch+21; Sch21b].

3.5. Signal Processing and Readout System for ATLASp3

In Chapter 5 of this thesis, the influence of ionizing radiation on the electronics of the HV-CMOS sensor ATLASp3 is studied. Therefore, the signal processing chain in the pixel and the further readout has to be understood. During the measurements, the sensor is supplied with power and configured by a flexible testing system, implemented by F. Ehrler and R. Schimassek [Ehr21; Sch21b]. The readout and configuration of ATLASp3 is controlled via a graphical user interface (GUI), developed by R. Schimassek. More detailed information than presented in the following about the signal processing, the readout, and the configuration of the sensor is provided in [Sch21b].

Signal Processing

A simplified schematic of the signal processing chain, for one pixel of ATLASp3, is shown in

²The fill factor describes the sensitive percentage of the matrix.

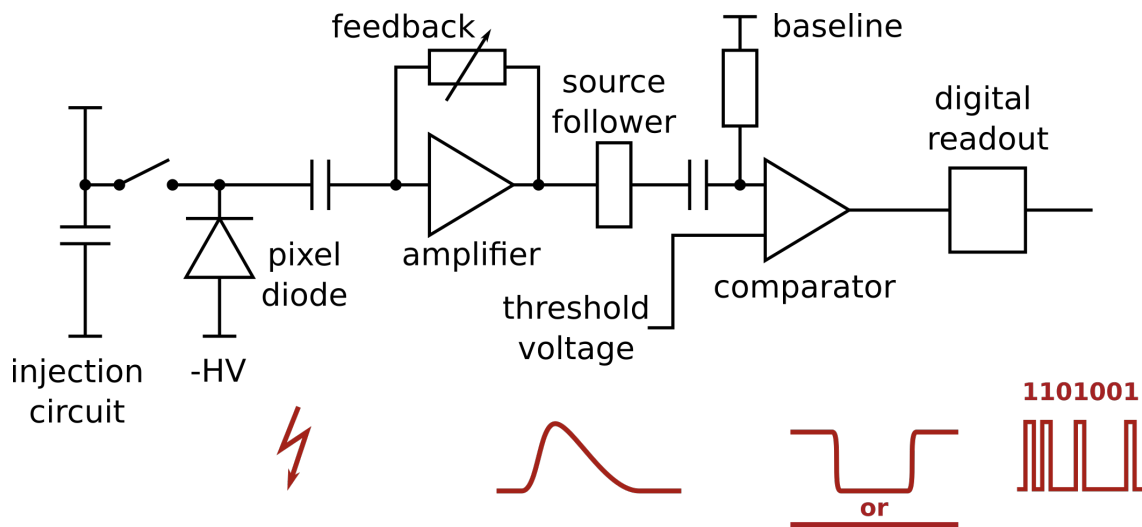


Figure 3.3.: Implemented pixel electronics in an HV-CMOS sensor – The simplified schematic illustrates the signal processing for one sensor pixel. A charge is injected into the pixel electronics by a particle or from the test injection circuit, indicated by a capacitor. The amplifier and the source follower convert the signal into a voltage. The feedback loop is adjustable. The variable feedback gives a continuous reset and the feedback strength defines the signal length. If the signal voltage exceeds the threshold voltage, the signal information is passed on to the readout. (adapted from [Ehr15])

Figure 3.3. Each pixel forms a sensor diode containing a charge sensitive amplifier (CSA), a comparator, a 4-bit RAM – 3-bit of RAM for threshold adjustments and one disable bit for the amplifier – and an output driver. Signals generated in the pixel diode or from an external injection circuit are converted and shaped into an analog voltage signal by the amplifier and a source follower. The feedback resets the CSA output continuously, leading to the slow falling edge of the signal. Otherwise, consecutive particle signals would lead to saturation of the amplifier. The feedback is realised with a transistor in saturation, granting a constant feedback current and hence, an almost linear correlation between the signal length and the charge generating it. Further description of the implementation on the feedback circuit is provided in [Ehr15; Per+21]. If the baseline voltage plus the signal from a particle exceeds the threshold voltage, the output pulse sets a flag in the periphery to store the incident (via a long routing line), where time information is added. The hit data contains the row address (372 rows – 9 bit), the column address (132 columns – 8 bit), the leading edge time stamp (10 bit), and a trailing edge time stamp (7 bit) of the comparator pulse, used for the time-over-threshold (ToT) calculation. The ToT (visualized in Figure 3.5) describes the length of a signal and is proportional to the deposited charge. Depending on the readout mode, the data from the hit buffers is either filtered based on a trigger signal in the Content Addressable Memory or directly transferred to end of column buffers in hit-driven mode.

Readout Setup with the GECCO System

The single chip setup during a ^{90}Sr measurement is shown in Figure 3.4. The sensor has to be supplied on the one hand with power and on the other hand with configuration information. Also, the digital signal data has to be recorded. The GEneric Configuration and COntrol (GECCO) system is a flexible testing system for HV-CMOS sensor development and provides all three features. The device under test (DUT) is connected with a field-programmable



Figure 3.4.: Single Chip Measurement Setup of the ATLASpix3 – From left to right: (1) FPGA: Nexys Video Board, (2) GECCO board, (3) Single Chip during a ^{90}Sr measurement.

gate-array (FPGA) and the necessary power supplies via the GECCO board. The FPGA provides the connection to the computer via USB (control and data acquisition) or ethernet (data acquisition). Different function card slots and optional jumper pins provide versatility for different sensor setups. The hardware, software, and firmware were developed by F. Ehrler and R. Schimassek [Ehr21; Sch21b].

The Four Layer Telescope Setup

From the same carrier PCBs as in the single chip setup, a four-layer beam telescope setup has been built with the GECCO system [Sch21b]. The data output of each layer is received by the single FPGA where it is combined to one data stream. There, the data of the four layers is also assigned a common time stamp allowing synchronous readout of all layers [Sch21b]. The full layout properties are described in Chapter 6.

3.6. Calibration of the Sensor

ATLASpix3 provides several configuration and calibration parameters. External charge injections via the injection circuit allow the measurement of so-called S-curves (Section 3.6.1). In this thesis, particular attention was paid to individual threshold tuning via the tuning DAC, which is addressed in Section 3.6.2. The determination of the signal length calibration parameters which are necessary to estimate the signal size from the provided ToT is described in Section 3.6.3.

The calibration procedures, such as the S-curve scan, the tuning procedure, and the ToT calibration were implemented by R. Schimassek for earlier measurements [Sch21b]. Apart from signal generation in the sensor diode, an external charge injection can be applied in each pixel over the injection circuit, shown in Figure 3.3. An adjustable voltage V_{inj} charges the capacitor and the stored charge is passed on as a test signal. These test signals can be injected in each pixel of the matrix. This feature allows the careful investigation of individual pixel characteristics. Based on this, adjustments to optimize the pixel performance can be done.

3.6.1. Measurement of S-Curves

An S-curve scan provides important information about a pixel's threshold and noise values. Thereby, n_{inj} signals are injected in a pixel. This is repeated for increasing injection voltage

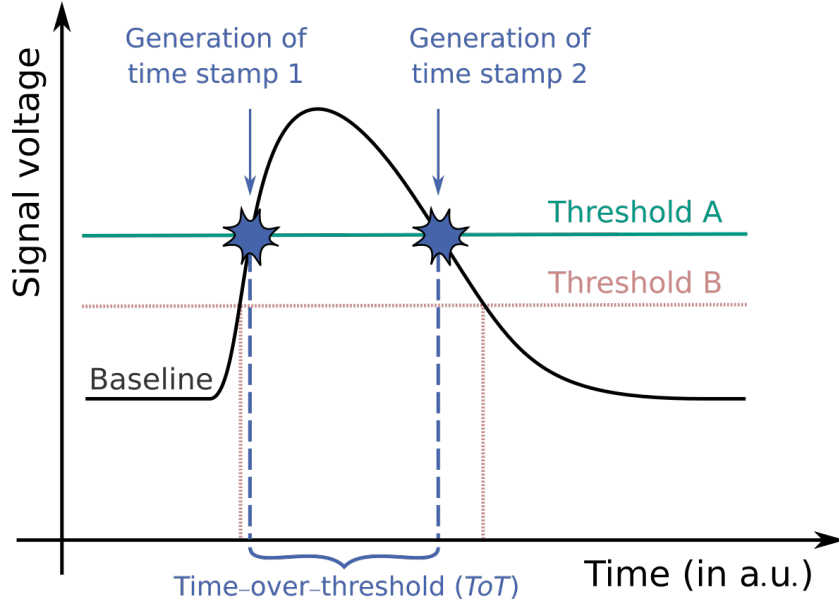


Figure 3.5.: Time-over-threshold (ToT) generation – The generated signal is added to a baseline voltage. If the sum of both exceeds the threshold, time stamps are generated at the leading and the trailing edge. The difference of these time stamps – referred to as ToT – depends on the signal size and the threshold. A higher threshold (A) leads to a smaller ToT . For a precise signal size measurement, the pixels of the sensor matrix should be tuned to equivalent threshold values.

steps. The detection efficiency η is described by the number of detected hits n_{det} per n_{inj} injected signals:

$$\eta(V_{inj}) = \frac{n_{det}}{n_{inj}}. \quad (3.1)$$

The efficiency plotted against the injected signal size gives the S-curve and can be fitted with the Gaussian error function. Figure 3.6 shows the S-curves of a single pixel for different configurations. The point of symmetry – or also, the signal size at which the transition of detection efficiency 0 to 1 takes place – is referred to as threshold voltage. The width of the transition describes the noise of the pixel, according to width of a Gaussian distribution. Fluctuations of the electronics, as for example threshold or comparator, are considered here. A noiseless system would lead to a detection efficiency shaped like a step function.

The global threshold is defined in the configuration of the sensor and is adjustable with an 8-bit DAC (values from 0 to 255). Each pixel additionally has a tuning DAC to adjust the individual threshold. In general, a low threshold is desirable to make the sensor sensitive to small signals. However, too small thresholds lead to noisy measurements, as noise is then registered as a hit.

3.6.2. Detection Threshold Tuning

A threshold alignment of all pixels is desirable and therefore, a 3-bit tuning DAC (TDAC) is implemented per pixel. The impact of this parameter on the threshold, and therefore the S-curve of a single pixel, is shown in Figure 3.6.

The tuning procedure presumes a global target threshold voltage (blue line in Figure 3.7). During the calibration procedure this value is targeted for all pixels by searching the best TDAC value for each pixel. If no target value is given, the S-curves of a subset of pixels at

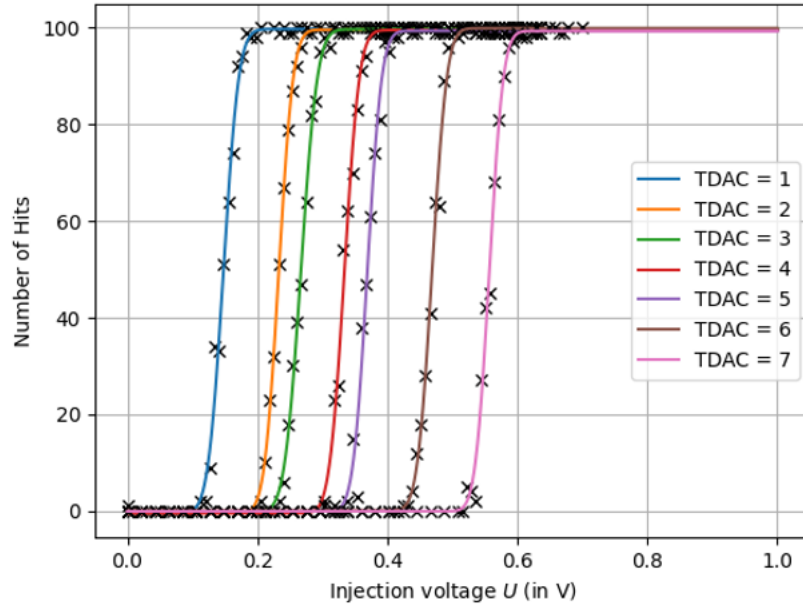


Figure 3.6.: S-Curves for different TDAC values – The S-curves follow the Gaussian error function. The point of symmetry is defined as threshold, the width of the transition is referred to as noise. The TDAC register, implemented on each pixel, can shift the threshold individually.

the highest possible TDAC = 7 are measured and the mean threshold μ minus three standard deviations of the threshold distribution 3σ , is selected as a target. During the tuning procedure, the S-curves of the pixels are measured and threshold and noise are determined. Figure 3.7 shows the narrow threshold distribution of the whole matrix after the tuning procedure. For comparison, the red curve shows the much broader threshold distribution of a subset of 40 rows before calibration at a TDAC value of 7.

3.6.3. Amplitude Information Calibration

The larger the collected signal, the higher the ToT of a hit. This makes the ToT valuable information for the generated charge in the pixel diode. But as the non-linear correlation between charge and ToT is not the same for each pixel, a calibration of the sensor matrix becomes necessary. The ToT calibration performs scans with several injections per pixel at varying signal sizes. The mean ToT value of the detected signals is determined and plotted against the injected signal size. This procedure is visualized in Figure 3.8. With this approach, a functional correlation between the signal size and the time-over-threshold ToT can be found. The edges of the generated signal motivate a function of the form:

$$ToT = a \cdot \log\left(\frac{V - V_0}{V}\right) + b \cdot x + c. \quad (3.2)$$

Here, V describes the injection voltage and V_0 , a , b , c , and d are the parameters determined in the fit. The relationship follows a logarithmic function with a linear term for high V . The individual pixel parameters are used for the calculation of a calibrated signal.

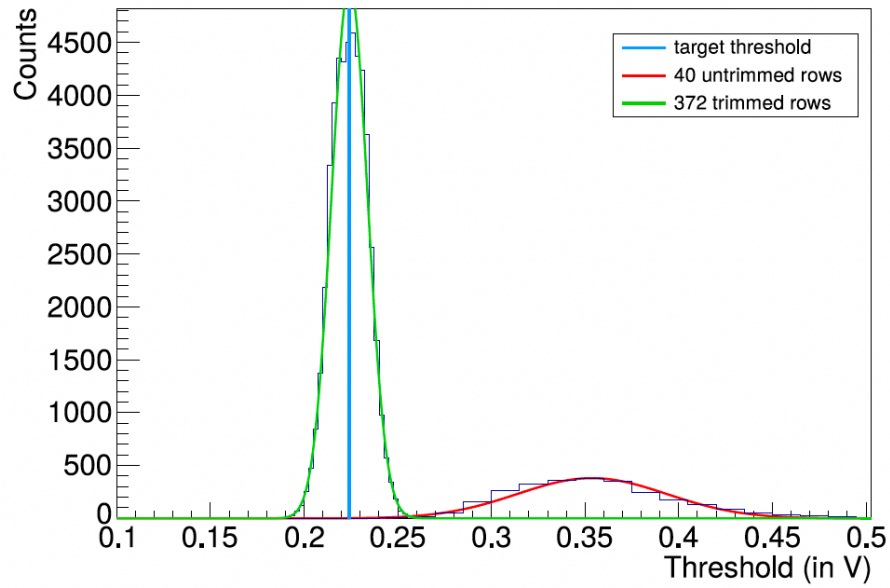


Figure 3.7.: Threshold values of tuned sensor matrix in comparison to thresholds of untrimmed region – Tuning of the matrix leads to a uniform threshold distribution. (from [Sch+21])

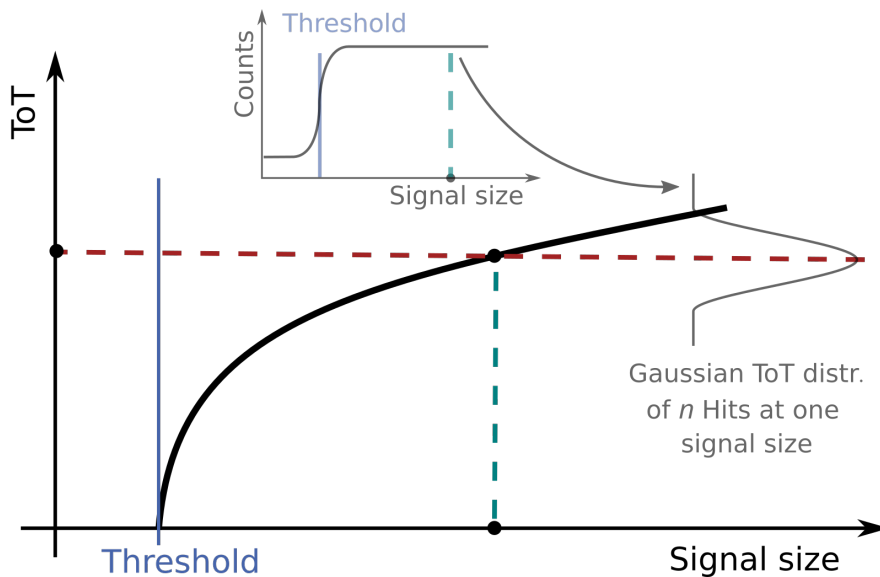


Figure 3.8.: Correlation between ToT and signal size for ATLASpix3 – During a ToT calibration, the parameters of a functional correlation between signal size and ToT are determined. A calibration compensates the different response of the individual pixels to a signal of a given size.

4

Applications of HV-CMOS Sensors

Due to their high spatial and energy resolution, silicon sensors are applied in many different domains. In this chapter, two very diverse fields are introduced. Both have in common that silicon sensors already are or could be an enrichment, compared to earlier detection approaches as e.g. ionization chambers.

Particle physics experiments have been using silicon sensors for a long time. The Large Hadron Collider, its upgrade and the development of a new type of silicon sensors for this purpose are described in 4.1. But also in medical physics silicon sensors enjoy growing popularity and further applications. Section 4.2 introduces the technique of ion therapy as a treatment method of various tumor types. The benefits that silicon sensors can bring as monitoring devices during medical treatments are discussed.

4.1. The Large Hadron Collider and its High Luminosity Upgrade

The internationally operated Large Hadron Collider (LHC) is located at the CERN research facility near Geneva, Switzerland. Section 4.1.1 will give a short introduction to the LHC. Section 4.1.2 describes the general-purpose detector ATLAS. The High Luminosity Upgrade was the reason for the development of a new generation of silicon sensors. This evolution is outlined in Section 4.1.3.

4.1.1. The Large Hadron Collider (LHC)

The LHC, world's largest and most powerful particle collider, has a circumference of nearly 27 km and is installed up to 175 m under ground. Protons are accelerated up to 7 TeV, first by a linear accelerator (LINAC 2), followed by three circular accelerators: the Proton Synchrotron Booster (PSB), the Proton Synchrotron (PS) and the Super Proton Synchrotron (SPS) [Brü+04]. Two bunched particle beams are injected into the ring accelerator in opposite directions. These particle beams are collided at four interaction points (IPs) around the ring, with a center of mass energy of up to $\sqrt{s} = 14$ TeV. Four large experiments – ATLAS, CMS, ALICE and LHCb – are located at these IPs. These detectors measure momenta, energies, and kinematic properties of the collision products. A sketch of the collider with the positions of the experiments is shown in Figure 4.1. The number of scattering processes in a certain time interval is given by the interaction rate

$$\dot{N} = \frac{dN}{dt} = \sigma \cdot \mathcal{L} \quad . \quad (4.1)$$

Here, σ denotes the interaction cross section which is dependent on the scattering process type and \sqrt{s} . The luminosity \mathcal{L} is dependent of the collider characteristics. For the study of rare processes in particle physics, high statistical significance and thus high luminosity is essential. The luminosity is evaluated as:

$$\mathcal{L} = \frac{n_1 \cdot n_2 \cdot f}{4\pi \cdot \sigma_x \cdot \sigma_y} \quad . \quad (4.2)$$

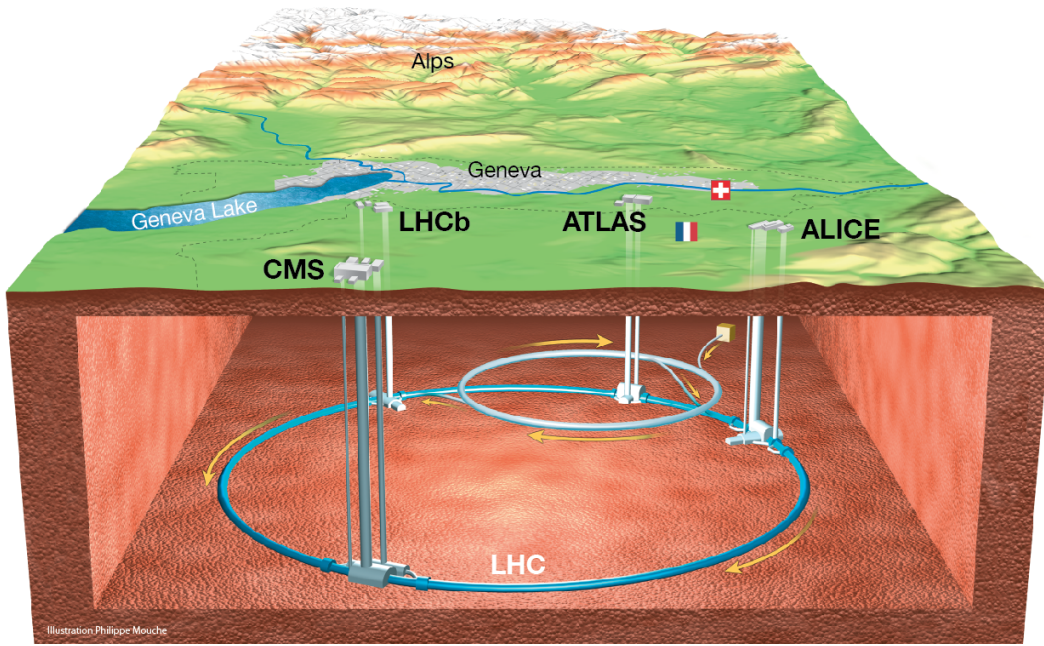


Figure 4.1.: The CERN accelerator complex – ATLAS and CMS are two large general-purpose particle detectors, located on opposite sides of the collider. The smaller experiments LHCb and ALICE are located in caverns of the former Large Electron-Positron Collider. (from [LHC12])

It depends on the number of particles in each bunch (n_1 and n_2), the bunch crossing frequency f and the cross sections σ_x and σ_y of the beams in x - and y -direction [W-M06]. The initial LHC was designed for a bunch crossing frequency of $f = 40$ MHz and a peak luminosity of $\mathcal{L} = 1.0 \times 10^{34} \text{ cm}^{-2}\text{s}^{-1}$ [Brü+04].

4.1.2. The ATLAS Experiment

The ATLAS experiment (**A** **T**oroial **L**HC **A**pparatu**S** – Figure 4.2) is the largest experiment located at the LHC and - next to the CMS (**C**ompact **M**uon **S**olenoid) - one of two general-purpose detectors. Both experiments were built to study the standard model and search for physics beyond it. The subdetectors of ATLAS are arranged cylindrically symmetrically around the interaction point, where the proton beams collide. The detectors are mainly used to determine the particle tracks, curved by a magnetic field. This provides information about the kinematic properties of the traversing particles and the energies. The subdetectors are arranged as described in the following.

The Inner Detector has a length of 6.2 m and a diameter of 2.1 m. It starts in a radial distance of 33 mm from the interaction point. Four layers with a coverage in pseudorapidity¹ of $|\eta_{\text{max}}| < 3.0$ and four pixel-disks as end-caps form the inner Pixel Detector [Cap+10]. The next detector system is the Semiconductor Tracker (SCT). The coverage of a larger area and the reduced particle rates due to the increased distance from the interaction point, allow strip

¹The pseudorapidity is defined as $\eta = -\ln \left[\tan \left(\frac{\theta}{2} \right) \right]$, where θ is the polar angle from the beam axis.

detectors with a length of 12 cm and a strip pitch of 80 mm. The SCT consists of four cylindrical barrel layers, 18 end-caps and covers an area of 60 m^2 with $|\eta_{\text{max}}| < 2.5$. [ATL14; ATL21a] Xenon filled drift tubes with a diameter of 4 mm and length of 1500 mm, build the outermost component of the Inner Detector – the Transition Radiation Tracker (TRT). [ATL+08]

Two sampling Calorimeters measure the energy of traversing particles by absorbing them. The higher the energy of the particle is, the further it will travel through the matter. Both calorimeters are arranged around the Inner Detector concentrically, and have an alternating structure of sensing and absorbing material. The absorber of the Electromagnetic Calorimeter (EMCal) is made from lead. Photons and charged particles interact electromagnetically and are stopped within. This calorimeter system uses liquid argon as sensing material.

Hadrons interact via strong force and are absorbed by steel layers in the Hadron Calorimeter (HCal), located behind the EMCal. Here, scintillating tiles sample the deposited energy. [ATL+08; ATL21a]

The Muon Spectrometer is the largest component of ATLAS and is almost exclusively reached by muons and neutrinos. The latter have very small cross sections and therefore cannot be detected in ATLAS. Thus, almost all particles detected in the muon spectrometer are in fact muons. The precise measurement of their momentum is important for the characterization of several processes of interest. A magnetic field is applied at the Muon Spectrometer to bend the tracks of traversing muons. Monitored Drift Tubes (MDT) measure the curvature of tracks with a high spatial resolution in the barrel and the end-caps. Also the Cathode Strip Chambers (CSC) have a high resolution and are located in the end-caps. Additional faster detectors ($\sim 1\text{ ns}$) with a lower spatial resolution are the Resistive Plate Chambers (RPC), located in the barrel, and the Thin Gap Chambers (TGC) in the end-caps. [ATL+08; ATL21a; Kob15]

Two Magnet Systems bend the charged particle tracks to allow momentum determination. A solenoid surrounding the Inner Detector induces a 2 T magnetic field. The magnetic field inside the Muon Spectrometer is produced by eight superconducting air-core coils and two end-cap toroid magnets.

Data Acquisition Up to 1.7 billion proton-proton collisions per second in the ATLAS detector produce data rates of more than 60 PB/s [ATL21b]. These huge data rates are reduced by zero suppression and triggering. The first stage in the triggers is a hardware level-1 trigger that selects events within $2.5\ \mu\text{s}$ and reduces the event rate from 40 MHz to 100 kHz [Sca10]. The level-2 trigger operates software based and reduces the data rate to 1 kHz.

4.1.3. High Luminosity and ATLAS Inner Tracker Upgrade

The High Luminosity upgrade (HL upgrade) aims for an operation at an instantaneous luminosity of up to $\mathcal{L} = 5 \times 10^{34}\text{ cm}^{-2}\text{s}^{-1}$ to further increase statistics [Bej+17]. Such high rates do not only require changes in the accelerator complex, but also introduce new challenges for the detector. Therefore, many components of ATLAS will be replaced during the long shutdown between 2025 and 2027.

A new Inner Tracker System was designed for the HL upgrade and will consist of silicon detectors only. In detail, the system will feature five pixel detector layers which cover a pseudorapidity range of $|\eta| < 4$ and four strip detector layers with $|\eta| < 2.7$. [ATL17; ATL19]

The monolithic HV-CMOS detector named ATLASpix1 – a predecessor of the ATLASpix3, used in this work – was developed as a prototype for a possible candidate for the outermost

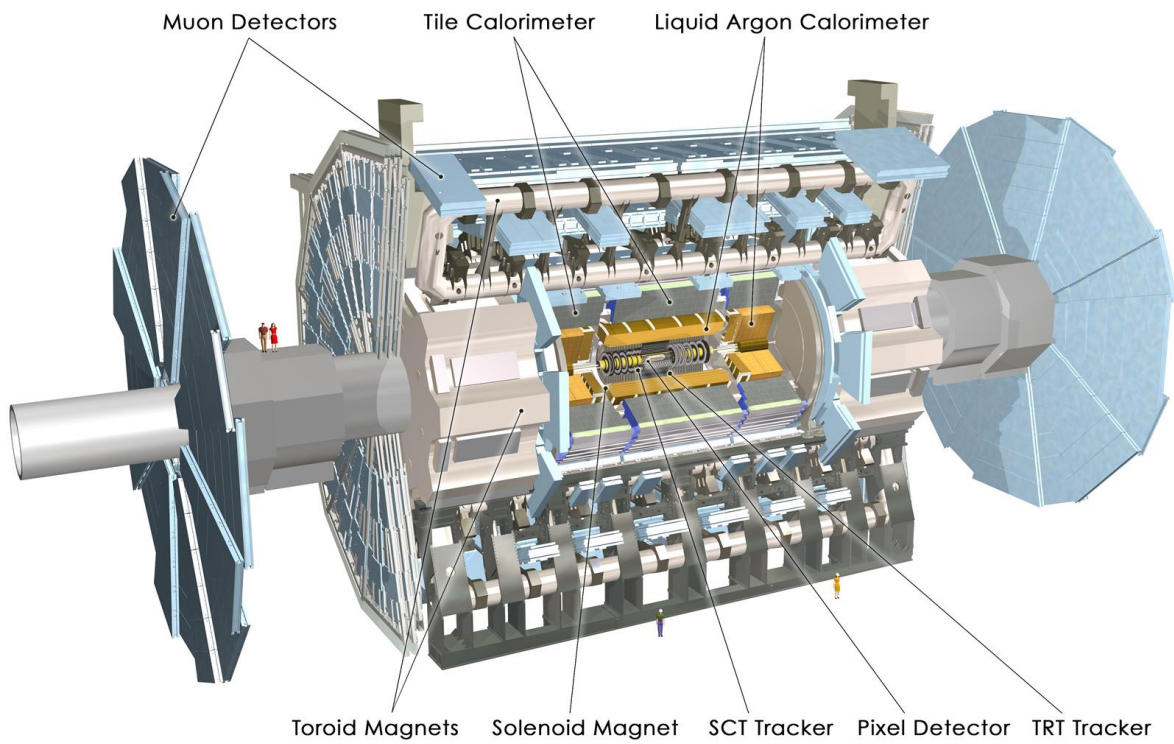


Figure 4.2.: Visualization of the ATLAS detector – ATLAS has a length of 46 m, a diameter of 25 m and weighs around 7000 tons. The subdetectors are arranged symmetrically around the interaction point. (from [Peq08])

pixel layer. The developed sensor ASIC of the ATLASp3x3 already fulfills the requirements concerning power consumption, detection efficiency, time resolution, response time and radiation tolerance. Even though the ATLAS collaboration decided against using HV-CMOS detectors in the next tracker of the ATLAS experiment, the technology itself is spreading. One of many possible application fields is described in the next section.

4.2. Monitoring of Medical Irradiation Treatments

Cancer is one of the main reasons for early deaths worldwide. In 2017, almost 490,000 people in Germany were diagnosed with cancer [Rob18]. To further increase their chances of survival, science is working tirelessly to improve the possibilities of cancer treatment. The three most widely used treatment methods are chemotherapy, surgery, and radiation therapy. Each method has its own benefits and drawbacks. Section 4.2.1 will introduce radiation therapy with ions. The Heidelberg Ion Therapy Center (HIT) is one example of a facility at which ion therapy is studied and applied. It is described in Section 4.2.2. Important monitoring methods in ion therapy are discussed in Section 4.2.3.

4.2.1. Therapy with Heavy Ions

Radiation therapy is widely used in tumor treatment and the most promising method in more than 50% of the cases [Del+05]. Cancerous cells have higher proliferation rates and regenerate less likely than healthy tissue [Bas+12]. The deposited energy in the cell can either lead to its instant death or can result in death from genetic changes. Typical doses are 1.5 – 3 kGy applied over several weeks [Bas+12]. Figure 4.3 shows the comparison of dose-depth distributions of ions and photons. Photons and electrons have rather broad depth-dose distributions and are applicable for tumors near the skin surface or in safe distance from sensitive organs. “Hadrontherapy [...] makes use of the precise relation between projectile energy and energy deposition along nearly straight trajectories inside matter.” [Kri+18] The integrated Bethe equation – only valid for charged heavy particles – results in a typically shaped energy deposit in the tissue, also referred to as Bragg curve. The penetration depth is well defined and also the biological effectiveness of hadrons is higher than for lighter particles as photons or electrons. This allows sparing of the surrounding tissue and reduces consequential damage. The fluctuation of energy loss can be approximated in a Gaussian distribution around the peak with a standard deviation σ_E , referred to as energy straggling. As a result, the range is also affected by straggling effects, which are defined by

$$\frac{\sigma_R}{R} \sim \frac{1}{2} \sqrt{\frac{m_p}{M}} \quad . \quad (4.3)$$

R describes the range of an incoming particle with mass M if m_p is the proton-mass [Ahl80]. This relation explains the dose depth of different particle types (Figure 4.3) and results in a sharper maximum for heavier initial ions. Apart from range straggling, inhomogenities in the initial beam energy² are a further reason for imperfect sharpness of the penetration depth. Because of the well defined and locally sharp energy deposition and the high biological effectiveness, hadrons are used to treat tumors in or near sensitive organs.

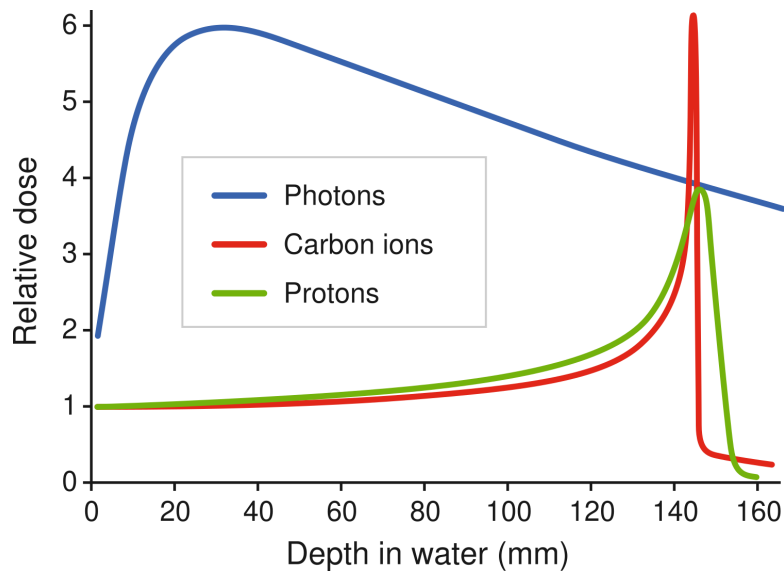


Figure 4.3.: Depth-dose curves of different particles in water – According to the Bethe equation, a sharp peak is expected in the dose distribution of charged particles (green and red). Photons, on the other hand, lose most of their energy near the surface (blue). The shape of the Bragg peak depends on the mass of the projectile particle. A tail in the dose of carbon ions (red) indicates to the presence of nuclear fragments. (from [Gra+20])

4.2.2. Irradiation Facility: Heidelberg Ion Therapy Center (HIT)

In 2009, the Heidelberg Ion Therapy Center (HIT) started as the first in Europe to perform medical irradiation of patients with ions. Possible nuclei for irradiation processes are protons, carbon, oxygen, and helium ions.

A sketch of the facility is shown in Figure 4.4. The different ion types are pre-accelerated by a linear accelerator. A synchrotron increases the energy up to 430 MeV/u. The 255 adjustable steps correspond to a penetration depth of initial 2 cm plus 1 mm in water for the first 193 steps and additional 1.5 mm per additional step. This results in a coverage of penetration depths in water equivalents from approximately 20 mm to 300 mm. Apart from energy steps, the intensity, and the focus can be adjusted. Also the number of ions per spill and its length with a maximum duration of 5 s is tunable. Table 4.1 shows the three parameter ranges resulting in over 60 000 possible combinations [KOW09]. The focus of the beam thereby describes the full width at half maximum (FWHM) of the gaussian-shaped beam at the iso-center. A high energy beam transport line (HEBT) directs the beam to four beam stations. Two treatment rooms have fixed horizontal beam positions. In 2012, a third treatment room was put into operation: The worldwide first 360° rotating beam delivery system can irradiate patients from optimal angles. A fourth beam station is important for quality assurance and is used for research experiments [Hab+04]. All experiments described in Chapter 6 were performed in this experimental room (8 in Figure 4.4) with varying beam settings.

At HIT, the irradiation of tumors is performed with a fully active dose-controlled raster scanning dose delivery system. Two magnets move the pencil-like ion beam point-by-point in iso-energetic slices (IES). Since the Bragg peak is sharp, a tumor with spatial expansion has to be irradiated layer-wise in several energetic steps, to cover the whole target volume. This overlay of Bragg curves in several irradiation steps leads to a spread-out Bragg peak (SOBP).

²Typically of the order of 1% of initial beam energy. [Lom09]

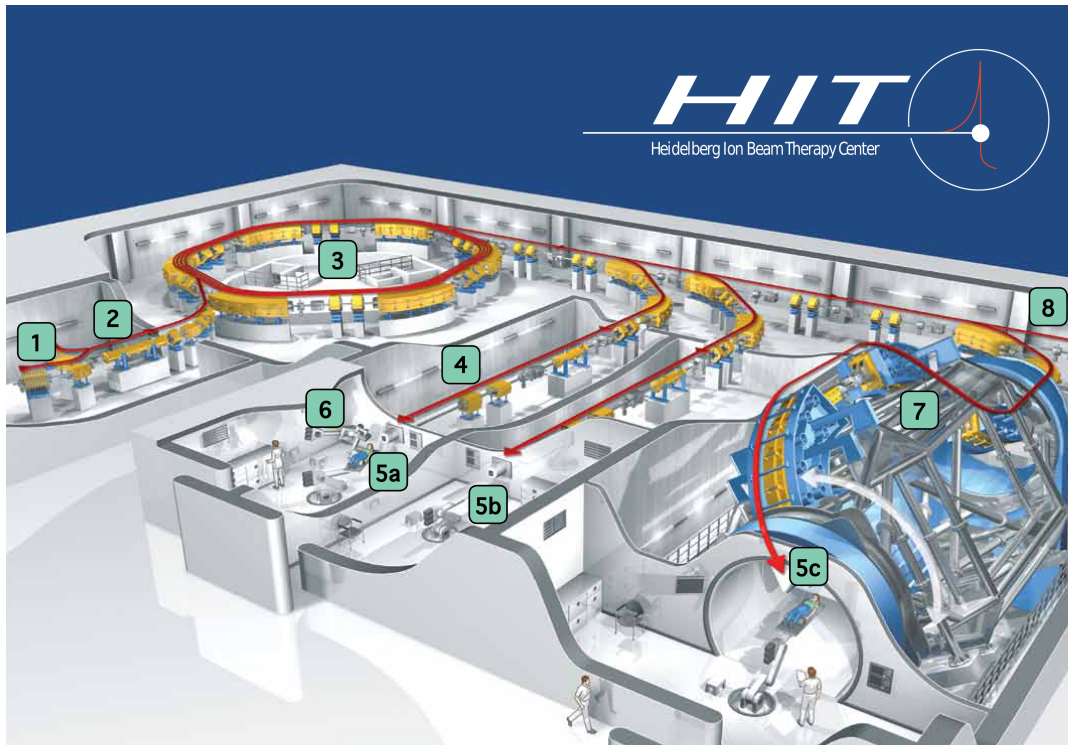


Figure 4.4.: Beam delivery of the Heidelberg Ion Therapy Center – From a source (1), ions of different types (protons, carbon, helium, oxygen) are accelerated with a linear accelerator (2) and passed on to a synchrotron (3). Magnets (4) focus and guide the fixed horizontal beam towards the treatment rooms (5a and 5b). Beam and patient are both monitored by systems during irradiation (6). The gantry – a 360° rotating beam delivery system (7) – enables irradiation of the patient from optimal angles in a third treatment room (5c). An experimental room (in extension of 8) allows quality assurance and research under real treatment conditions. A beam dump is located next to the experimental room. (adapted from [Cor12])

Table 4.1.: Ion beam parameters at the HIT facility – from [Pet20]

Parameter	Steps	Protons	Carbon
Energy	255	48 – 221 MeV/u	88 – 430 MeV/u
Focus	6	11 – 33 mm	3.5 – 13 mm
Intensity	10	$8 \cdot 10^7 - 2 \cdot 10^{10}$ 1/s	$2 \cdot 10^6 - 5 \cdot 10^8$ 1/s

Here, also the region before the Bragg peak has to be taken into account for calculations of the total energy deposition. An optional ripple filter can be used to smoothen the sharp energy distribution of particles and increase the longitudinal width of the Bragg peak [WK99]. This can be useful to reduce the number of IESs and treatment time. Complex and individual treatment plans are developed prior to each irradiation based on preliminary CT scans. The position, width, and intensity of the beam during treatments are monitored online by ionization chambers (ICs) and multi-wire proportional chambers (MWPCs). This monitoring system is described in Section 4.2.3.

4.2.3. Beam Monitoring

Since therapy with ions leads to a sharply localized energy deposit, mistakes in beam positioning can lead to fatal effects. Healthy tissue could be struck and consequentially damaged or parts of the tumor could receive an insufficient dose. To prevent such errors, different monitoring methods are applied in medical irradiation treatment. First of all, the positioning of the beam must be monitored sufficiently. Apart from this, errors may occur due to incorrect dose calculations or uncertainties during treatment [ZF13]. To reduce these mistakes, non-invasive and in-vivo monitoring methods are desirable. Different beam monitoring approaches, also via secondary particle detection, are introduced in the following section.

Monitoring of the Primary Ion Beam

Precise localization of the beam is a fundamental prerequisite for successful treatment. As shown in Figure 4.5, the Beam Application and Monitoring System (BAMS) at HIT consists of multi-wire proportional chambers (MWPCs) and ionization chambers (ICs) [Brä08]. The geometrical beam properties – position and width – are detected by two wire-proportional chambers with a resolution ≤ 0.2 mm. Three ionization chambers measure the integrated applied dose at one irradiation spot. A feedback system directly communicates misalignments to the scanner magnets and corrects the beam positioning angles. The position and intensity feedback systems require certain detection time scales. The typical irradiation time of one raster point is several milliseconds. The position measurement (250 μ s) is short compared to this raster frequency [Sch+15]. For redundancy purposes, all control systems exist at least twice.

Magnetic Resonance Imaging (MRI) during treatments would allow online diagnostics. ICs and MWPCs are not designed for operation in magnetic fields, whereas silicon detectors are used in magnetic fields in many projects. Furthermore, HV-CMOS sensors would be able to determine dose and beam position simultaneously and could be an addition to the BAMS unit in the future. Research into possible alternatives or supplements to the present monitoring

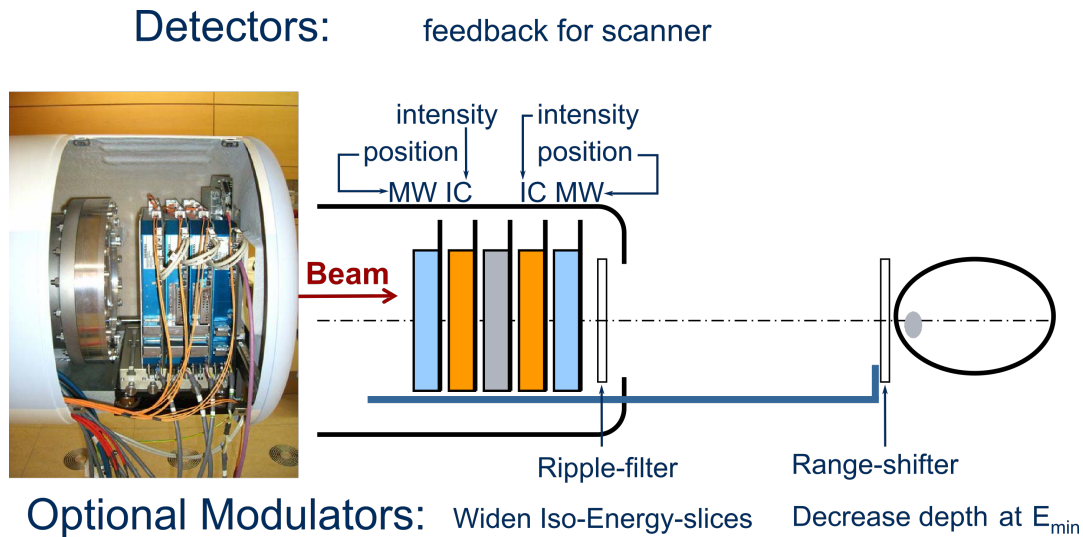


Figure 4.5.: Beam Application and Monitoring System (BAMS) at the HIT – The BAMS at HIT consists of redundant detectors to resolve position (multi-wire proportional chambers, MW) and intensity (ionization chambers, IC) of the beam. A feedback system passes information about misalignment to the scanner magnets where positioning can be corrected. Optional modulators are the ripple filter and a range shifter. The former widens the energy distribution for a smeared out Bragg peak for more homogeneous irradiations. The second brings additional material in the beamline to decrease the penetration depth in the target tissue at minimal beam energies. (adapted from [Brä08])

devices is currently in progress [Pet18] [Ehr21].^{3 4}

In the course of these studies, an HV-CMOS sensor – the ATLASpix3 – was installed at the HIT beam dump. To disentangle the effects of the irradiation with protons and carbon ions, the ionizing dose contribution has been emulated. In Chapter 5 of this thesis this contribution is studied with a inhomogeneous, iterative irradiation study at the X-ray tube of the ETP, KIT. The aim is to emulate surface damage and compare the effects of the annual dose of ionizing radiation with the results of the irradiated sensors at the HIT beam dump.

Monitoring of Dose Deposit - Secondary Particle Detection

Even with an excellent beam monitoring system uncertainties remain. These can already arise during the calculation of treatment plans: Statistical uncertainties in the Computer Tomography scan (CT), conversion methods in imaging processes and necessary approximations are some examples. Also, errors in the setup or in the positioning of the patient can occur. Organ motion or changes in the tissue structure (e.g. shrinkage of the tumor) are a further problem. All this leads to the necessity of safety margins, at the expense of treatment quality. To further improve treatments, a non-invasive and in-vivo detection method of the dose deposit in tissue is desirable.⁵[Kra15]

³ARTEMIS project (<https://www.dkfz.de/en/clinicianscientist/Research%20profiles/2021/ClinicianScientistFellowships2021-groupinfoE050.pdf>)

⁴HEIKA project (<https://www.heika-research.de/en/research/medical-technology-health-mth/particle-therapy-beam-monitoring-hv-cmos-sensors>)

⁵CT scans would lead to an increase of dose for the patient.

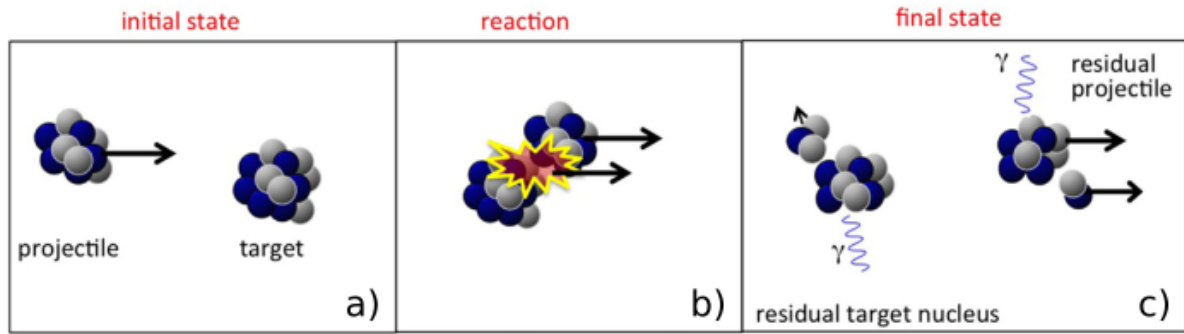


Figure 4.6.: Fragmentation process during nucleus-nucleus reaction – Lighter fragments - so called secondary ions - are produced during nucleus-nucleus reaction in heavy ion therapy. The abrasion-ablation model describes the fragmentation of the projectile and the target nucleus. (from [Kra15])

A promising way to achieve this is the detection of secondary particles. Figure 4.6 shows the typical fragmentation process taking place during irradiation with carbon ions. The nuclear reaction between the projectile and a target atom can be described with the abrasion-ablation model. During the fast abrasion (10^{-22} to 10^{-23} s), an excitation takes place. The ablation (10^{-18} to 10^{-16} s) describes the de-excitation and evaporation of secondary particles, like photons and light nuclear fragments [FS96]. The distribution of the secondary particle origin is correlated with the beam range in the tissue.

A problem caused by fragmentation is the modified dose deposition. A considerable energy dose is deposited in the buildup region in front of the Bragg peak by secondary particles. The reduced charge of the fragments also results in an increased range (from Bethe equation (2.8): $\sim A/Z^2$). In Figure 4.3, a characteristic tail behind the Bragg peak is visible in the depth-dose curve. The position of the Bragg peak is scarcely effected, but because of the fragmentation, energy deposition at the maximum is reduced by up to 50% [Cus11]. Therefore, the fragmentation has to be taken into account carefully for irradiation treatments. Medical physics, however, has taken advantage of these secondary particles, as the origin of the secondary particles is correlated with the range inside the tissue. Three approaches used for real-time monitoring in hadron therapy are explained in the following. [Kra15]

Positron emission tomography (PET) A commonly used imaging process is positron emission tomography (PET). Radioactive β^+ -emitters are thereby detected by the presence of annihilation photons with a characteristic energy. Maccabee et al. suggested this as an in-situ dose deposit detection method in 1969 [MMR69]. During ion irradiation therapy, radioactive fragments are produced in the tissue, and typical annihilation processes of positrons and electrons take place. The two photons, produced in the annihilation, have an energy near 511 keV and are emitted in dependence of the initial momentum of the system before annihilation [Ble13]. As the radioactive fragments stay in the tissue depending on their half-time, this method can be applied several minutes after treatment but a parallel monitoring is not possible this way. To avoid background from prompt irradiation products, at least 40 s have to pass during end of treatment and the PET [Sha+11]. Another problem (mentioned in [ZF13]) is called biological washout, which causes uncertainties in the measurement of the photon origin, especially in highly heterogeneous tissue regions.

Prompt-gamma monitoring The problematic γ -background during PET is useful for prompt-gamma monitoring in hadron therapy. Both, target nuclei and projectile primary ions, are

excited in the irradiation processes. With the de-excitation of the particles, photons are emitted. These products of inelastic scattering processes are produced on a very small time scale ($< 10^{-9}$ s) which suggests a prompt detection method [Tes+09]. The detection with e.g. Compton cameras is difficult due to a broad energy distribution [Kri+18], which leads to low reconstruction efficiencies. A world-first clinical application was tested in 2016 and research continues [Ric+16].

Detection of prompt charged secondary ion fragments A rather new attempt is the detection of charged secondary ion fragments. Initial studies were conducted in 2013 [Gwo+13]. The distribution of the particle origin is again correlated with the Bragg position inside the tissue and as the secondary fragments are emitted in prompt processes, this method is considered to be fast. Charged particles are only emitted in sufficient numbers during irradiation with heavy ions, such as carbon. In proton therapy, on the other hand, mainly neutrons are produced. Therefore, this method is only applicable for radiation therapy with heavy ions.

High detection efficiencies for the tracking of prompt charged secondary particles can be achieved with modern silicon sensors. Former studies were performed with a telescope with the TimePix1 and TimePix3 sensors as layers. Spatial resolutions, of the beam range in a homogeneous Polymethyl methacrylate (PMMA) cylinder, of less than 1 mm were achieved [Rei+17]. In 2021, [Fél+21] demonstrated that the precision of this method is potentially sufficient for clinical applications. More details on the implementation of former studies are given in Chapter 6.1.

In Chapter 6 of this thesis, the capability of an HV-CMOS sensor telescope for detecting secondary particle tracks is studied.

4.2.4. HV-CMOS Sensors as Beam Monitoring Device

ATLASPix3 was developed for the requirements of the fifth layer of the tracker of the ATLAS HL upgrade (Section 4.1.3). For this application, the expected fluence per area changes on the scale of meters [ATL17]. Consequently, the fluence on one sensor of $20 \times 20 \text{ mm}^2$ can be assumed constant. On the area of one sensor ($20 \times 20 \text{ mm}^2$) with $50 \times 50 \mu\text{m}^2$ pixels, a maximum hit rate of 12 hits/event is expected for an event rate of 40 MHz in the fifth layer [ATL17]. This equals a maximum hit rate of 4.88×10^8 hits per second and sensor.

This differs strongly from the environment encountered in beam monitoring: At HIT, the ion beam has a width range between 3.5 mm and 33 mm, depending on the beam settings [Pet20]. In addition, most of the time, the beam is directed to the same position in the middle of the detector. Hence, the received fluences differ strongly even between neighboring sensors in a beam monitor. Even on a single sensor, large gradients are to be expected. This is especially true for larger sensors as ATLASPix3 with dimensions of $21 \times 20.2 \text{ mm}^2$. Apart from this, the direct beam monitoring leads to particle rates up to 2×10^{10} particles/s at energies between 48 MeV/u and 430 MeV/u [Pet20]. This largely exceeds the numbers ATLASPix3 is designed for, requiring dedicated developments for medical applications as the HitPix prototypes [Web21]. Nevertheless, radiation damage and the behavior of parts of the electronics can be studied with ATLASPix3 to gain information for the development of the HitPix sensors [Sch21b].

For secondary particle monitoring, the expected particle rates are orders of magnitude smaller and less focused on one position. This application is more similar to the original tracking application and is studied in Chapter 6.

5

Irradiation Studies with ATLASpix3

ATLASpix3 was developed for the HL upgrade of the ATLAS experiment and therefore designed to tolerate the radiation exposure in that environment. With the new field of application in radiation therapy, the properties of these HV-CMOS sensors need to be examined under the new conditions, as the requirements in this application differ from the originally intended scope (Section 4.2.4).

Section 5.1 summarizes the measurements by R. Schimassek [Sch21b] after an strong inhomogeneous irradiation at the HIT beam dump with an equivalent to 1.5 annual doses of protons and carbon ions at HIT. The matrices of several ATLASpix3 sensors show reduced detection efficiencies of charged particles, an increase of noise hits, and higher leakage currents. To disentangle the effects causing the damage (Section 2.4), a different ATLASpix3 sample has been irradiated with X-rays iteratively as part of this thesis. For X-ray irradiation, bulk damage can be neglected so the focus is on damage in the pixel electronics. The measurement procedure is outlined in Section 5.2. Section 5.3 summarizes the results of characterization measurements before the irradiation. The dispersion effects discovered during the measurements with different signal types are described and discussed in Sections 5.4 to 5.6. A summary of the results is given in Section 5.7.

5.1. Motivation of Irradiation by Previous Studies

A stack of five ATLASpix3 sensors was placed in the beam dump of the Heidelberg Ion Therapy Center. The irradiation took place with protons and carbon ions, each at an energy around 110 MeV/u. With the expected annual fluences at the HIT facility, an energy deposition at the annual dose was estimated with stopping powers from NIST¹ by A. Dierlamm [Ber+17]:

$$\left. \begin{array}{l} \text{Carbon ions: } 6 \times 10^{12} \frac{1}{\text{cm}^2} \cong 210 \text{ kGy} \\ \text{Protons: } 6 \times 10^{11} \frac{1}{\text{cm}^2} \cong 60 \text{ kGy} \end{array} \right\} \text{Annual dose of 270 kGy}$$

The exact doses are unknown, as the study was of parasitic nature. Studies by R. Schimassek showed a reduction of the efficiency to detect charged particles and an increase of number of noise hits in the affected region [Sch21b]. The accumulated noise hits in the sensor matrix during a short measurement are visible in Figure 5.1. Also, an increase of the leakage current over three orders of magnitude was visible. The aim of this work is to estimate the contribution of surface damage to these results. As surface damage is mainly induced by ionizing radiation and to mimic the situation in previous studies, an inhomogeneous irradiation with X-rays was performed.

¹NIST – National Institute of Standards and Technology

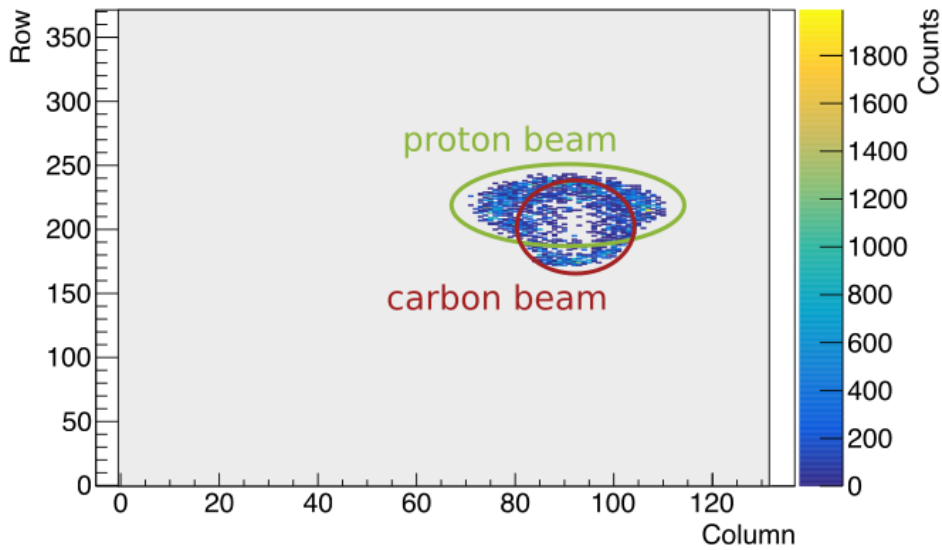


Figure 5.1.: Noise hit map of the ATLASpix3 matrix after irradiation at the HIT beam dump. – The plot shows the total number of noise hits per pixel of the sensor matrix ($> 150\%$ annual dose at HIT) during a short measurement with no high voltage applied. The shapes of each beam profile were confirmed by additional films that were placed in front of the sensors. (from [Sch21b])

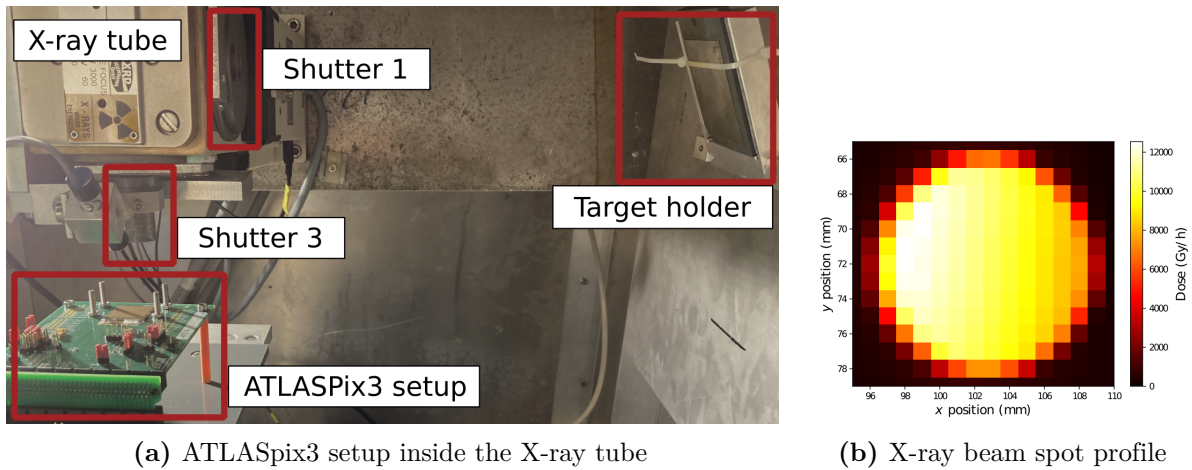


Figure 5.2.: ATLASpix3 setup inside the X-ray tube of the ETP and X-ray beam spot profile – (a) The whole ATLASpix3 setup is placed beneath the X-ray tube. The irradiations take place with shutter 3 opened. Additional energy calibration measurements were performed with shutter 1 opened. During the calibration, the X-ray particles excite atoms of a target which is kept in place by the target holder. (b) Reference beam profile for a tube voltage $V = 60$ kV and current $I = 30$ mA at a distance of 10 mm. (from [Mül21])

X-Ray Tube at KIT, ETP

The X-ray tube, used for the irradiation studies in this work, is located at the Institute of Experimental Particle Physics (ETP) at the Karlsruhe Institute of Technology. The X-ray tube is equipped with a tungsten cathode and typically operated at its maximum acceleration voltage of $V = 60$ kV. The adjustable electron current I has a range of $I = 2$ mA up to 50 mA. This results in a maximum power of $P = 3$ kW [Ins20]. The irradiations in this campaign were performed with $V = 60$ kV and $I = 30$ mA. A fluorescent disk provides information about the horizontal position of the X-ray beam and was used for the positioning of the setup.

Figure 5.2a shows the ATLASpix3 setup inside the tube. Three shutters control the output direction of the X-rays. Direct irradiation can be performed with shutter 3 open. The beam profile has a diameter of ~ 1 cm and is shown in Figure 5.2b. This size represents an upper limit of the irradiated area during the inhomogeneous irradiation. A second shutter (shutter 1) can be opened to irradiate a target, also placed inside the X-ray tube which in turn emits characteristic monoenergetic X-rays [May97]. This method was used for energy calibrations with a lower tube electron current of $I = 10$ mA. Dose calculations and irradiation planning can be controlled via the control software of the X-ray tube.

5.2. Measurement and Analysis Procedure

The following section summarizes the steps of the measurement procedure. Section 5.2.1 describes the mechanical setup. The applied doses are summarized in Section 5.2.2. S-curves were measured after each irradiation step and a threshold tuning was performed, explained in Section 5.2.3. An energy calibration with monoenergetic X-ray spectra allows the determination of the pixel amplifier gain. The required measurement is described in Section 5.2.4. Section 5.2.5 describes the measurement with electrons from a ^{90}Sr source. The format of the data and the analysis is covered in Section 5.2.6.

5.2.1. Mechanical Setup

All measurements have been performed inside the X-ray tube shielding box for safety reasons and to obtain a consistent environment. Hence, a complete single chip setup was used. A suitable mechanical construction had to be developed to realize the planned sequence of measurements, described in the following. To guarantee inhomogeneous irradiation, a lead shielding with 0.5 cm thickness was fabricated at IPE. A round opening with 5 mm diameter allowed the X-ray irradiation of the upper right sensor region.

Four M3 screws were attached to the sensor carrier board. These screws hold a 3D printed carrier in place, made from ABS. The carrier has a sensor sized opening below the Pb shielding and protects the sensor and the wire bonds from damage from handling. The lead shielding has four holes which keep it in place on top of the carrier during irradiation.

After each irradiation step, a measurement with charged particles from a ^{90}Sr source was performed. Therefore, a second carrier was designed and fabricated which held the source in place using the same screws. A circular notch inside the upper shielding indicated the correct position of the source for each of the different measurements. The position of the cutout in the carrier was shifted towards the upper right on the sensor matrix to collect more signal from the ^{90}Sr source in the irradiated region.

A third step involved illumination of different targets with X-rays. For these measurements, shielding and both printed carriers were removed.

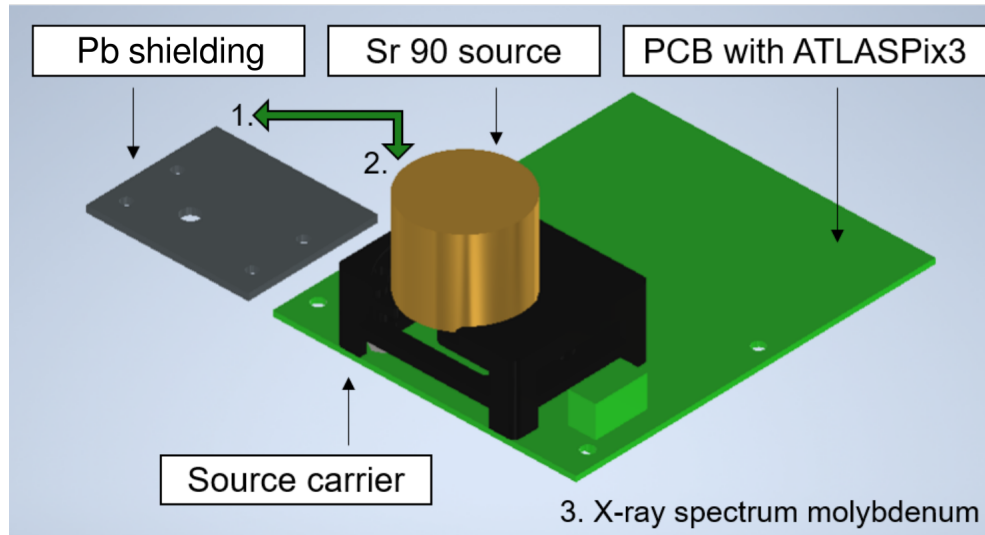


Figure 5.3.: Mechanical setup for the measurement procedure during the X-ray irradiation study. – This sketch shows the device used to perform the different measurements steps. (1) The inhomogeneous irradiation requires a Pb shielding which is carried by a carrier specially designed for this purpose. (2) To position the ^{90}Sr source over the irradiated region and keep a necessary distance, an additional source carrier was 3D printed and placed on top of the one for irradiation. (3) The shielding and the carriers have to be removed for the measurement of the X-ray spectra.

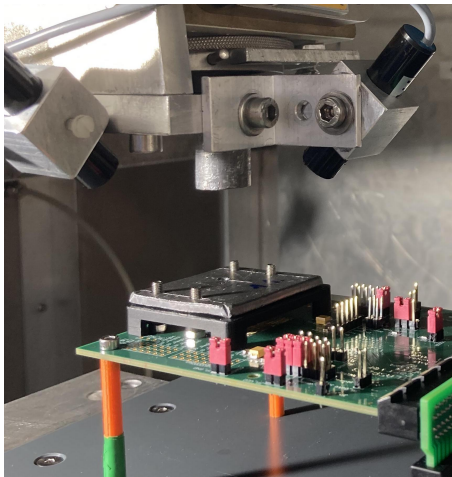


Figure 5.4.: Irradiation setup with Pb-shielding.

Table 5.1.: The iterative dose steps.

Step	Dose (in kGy)	Step	Dose (in kGy)
0	0	9	70
1	10	10	80
2	15	11	90
3	20	12	110
4	25	13	130
5	32	14	160
6	40	15	200
7	50	16	240
8	60	17	300

5.2.2. Irradiation

The advantage of an inhomogeneous irradiation is the possible direct comparison of irradiated and non-irradiated pixels from the same die. Like during the irradiation at the HIT beam dump, only a part of the matrix and not the periphery was affected. During the irradiations performed in this work, only the in-pixel readout electronics was affected, the periphery was shielded with a lead shielding. Therefore, components possibly exposed to the irradiation are

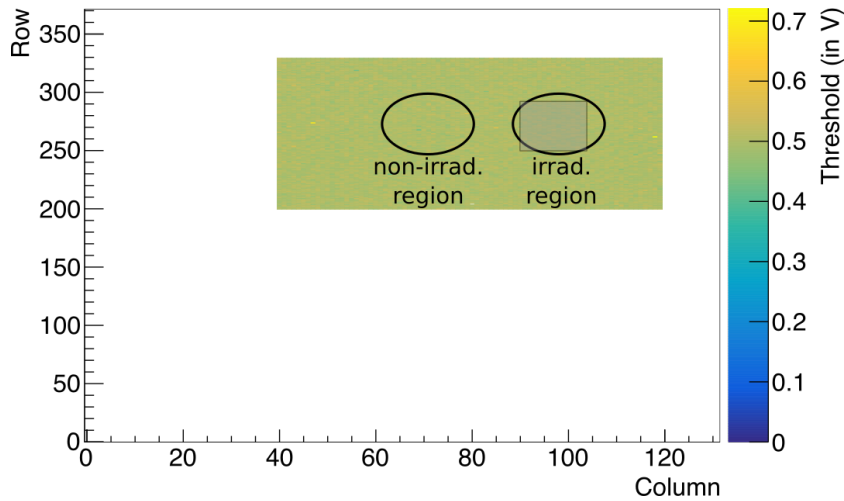


Figure 5.5.: Threshold distribution in the tuned region of the sensor matrix – Before each tuning of the large rectangular region, the S-curves in a smaller rectangular (marked gray) region inside the irradiated region were measured. The target value of the threshold tuning procedure was set to the mean transition voltage of the S-curves. The actual irradiated region is slightly larger than depicted in this plot. The circle (black) only describes the analysed subset of pixels which was chosen smaller than the irradiated region to neglect edge effects.

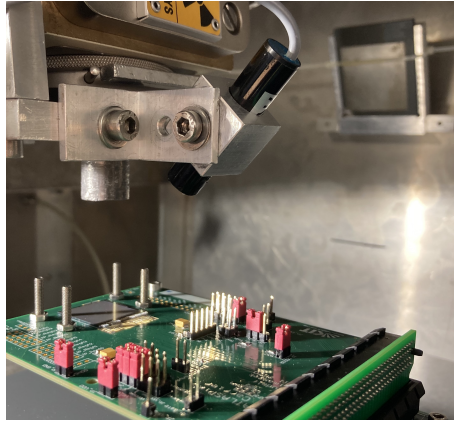
the amplifier with the feedback transistor belonging to the CSA, or the comparator in each pixel.

The irradiation was performed iteratively in the X-ray irradiation setup at ETP. Only small doses were applied at once, allowing a careful analysis of the dispersions of the characteristic properties of the sensor. In total, the expected annual dose of the HIT beam dump was accumulated in 17 sequential steps up to a total dose of 300 kGy (Table 5.1). In his work, F. Ehrler showed the effects of X-rays on different transistor types [Ehr15]. According to these studies, the largest dose effects are expected at doses between 30 kGy and 50 kGy. Therefore, the steps at lower doses are smaller and were adapted to the actual results during the irradiation. Unfortunately, strong effects in the matrix were already visible after the first applied dose of 10 kGy. Even smaller dose steps would have been favorable at the beginning.

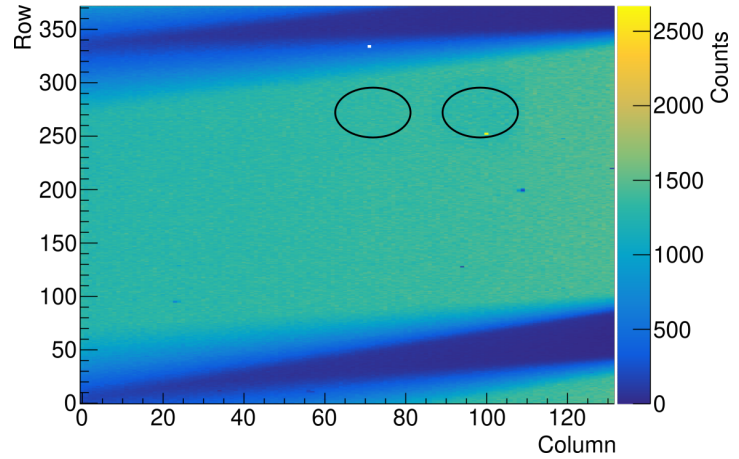
No voltages were applied to the setup during the irradiation and the FPGA was turned off. After each irradiation step, a cool-down time of 15 minutes was set to obtain reproducible measurements, following the advice of F. Ehrler. The irradiation study took several days. All measurements were performed at room temperature. During overnight measurement breaks, the sensor was stored at a temperature of -18°C to suppress annealing effects.

5.2.3. S-Curve Scan and Tuning

During irradiation, the electronics implemented in each pixel may change their properties. To still guarantee an optimal threshold distribution, a tuning procedure was performed after every irradiation step. After a significant drop in the detection efficiency of the irradiated region at a dose of 10 kGy, we decided to choose a target threshold suitable for the irradiated region. To find such a target, S-curves of a smaller rectangular range inside the irradiated round region were measured (Figure 5.5). The mean threshold of this region was determined by finding the mean transition voltage of the S-curves. If this value deviated strongly from the target value of the tuning procedure before, the mean threshold was chosen as the target value of the



(a) Indirect X-ray irradiation without shielding. The target material is visible on the right in the background.



(b) Hit map of indirect X-ray irradiation.

Figure 5.6.: X-ray spectrum measurement with a molybdenum target after an applied dose of 110 kGy – (a) The irradiation with photons from a molybdenum target is performed without any shieldings. (b) The shadows in the hit map with less signal result from the mounting screws on the PCB. These screws hold the carriers and the Pb shielding in place. The black circles visualize the analysed regions.

next tuning procedure. As we wanted to compare the properties of the irradiated pixels with non-irradiated ones, the rectangular tuning region – shown in Figure 5.5 – was larger than the actual irradiated region. For comparison, a second pixel subset with the same size was analysed. The black circles show the analysed pixel regions of the sensor matrix. Each subset contains 591 pixels.

The tuning procedure and the results of the measurements before irradiation are discussed in Section 5.3. Section 5.4 discusses the influence of the irradiation on these test signal measurements.

5.2.4. Energy Calibration with X-Ray Spectrum Lines

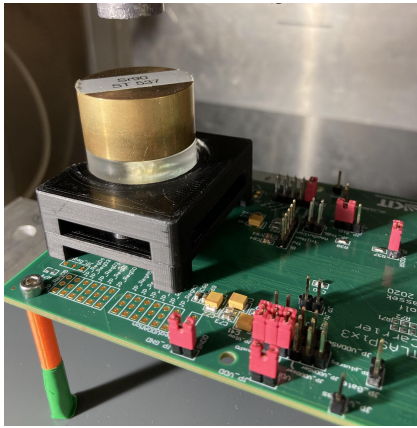
Inside the ETP X-ray setup, illuminating different target materials and irradiating the sensor with resulting characteristic X-ray energies is possible. For this step, all shieldings from the sensor were removed, as visible in Figure 5.6a. The dominant interaction process of X-rays with matter from the target plate is the photoelectric effect. Thereby, electrons in the outer shells of the target atoms are excited by the primary X-rays. During deexcitation, a photon with a characteristic energy is emitted. Table 5.2 provides the K_{α_1} energies of the three targets used in this study: molybdenum (Mo), silver (Ag) and indium (In). The monoenergetic photons either deposit their whole energy punctiformly in the sensor material or do not interact at all. Therefore, it can be assumed that the total energy of detected photons is used for the generation of charge carriers. In silicon, a mean energy of $E = 3.62 \text{ eV}$ is required to generate an electron-hole pair. Therefore, the expected number of charge carriers per photon generated in the sensor can be calculated for each target material:

$$N_e = \frac{K_{\alpha_1}}{3.62 \text{ eV}}. \quad (5.1)$$

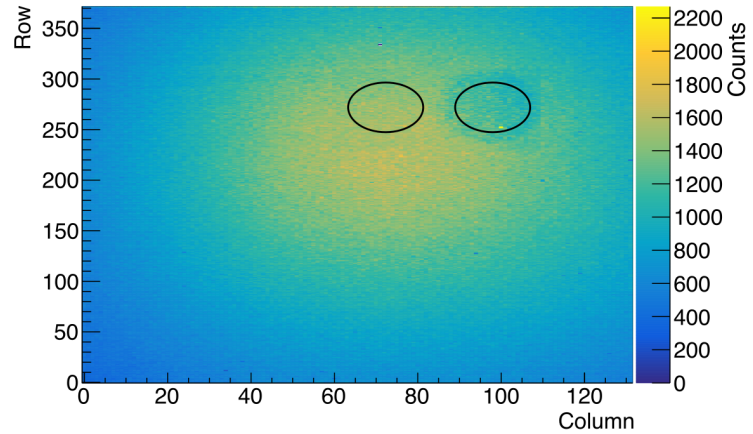
This expected number of electrons is then compared with the amplified signal. First, each ToT signal is converted into a voltage with the parameters from the ToT calibration. The

Table 5.2.: Energies of X-ray K_{α} emission lines – The table shows the photon energies (in electron volts) of the first K -shell emission line. The expected signal can be calculated with the required energy for electron-hole pair production in silicon, $I_0 = 3.62$ eV. [Kir+86]

Element (symbol)	$K_{\alpha 1}$ energy (in eV)	Expected signal (in e^-)
Molybdenum (Mo)	17479.34	4829
Silver (Ag)	22162.92	6122
Indium (In)	24209.7	6688



(a) Measurement with ^{90}Sr source.



(b) Hit map of ^{90}Sr measurement.

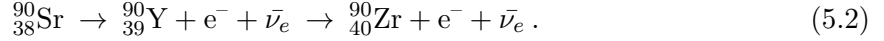
Figure 5.7.: ^{90}Sr measurement with a source carrier after a dose of 110 kGy – (a) The measurement with a strontium source is performed after each irradiation step. (b) The hit map of the ^{90}Sr measurements: Two noisy pixels were masked during the whole analysis, as they already showed noise hits before irradiation. After an applied dose of 110 kGy the irradiated region is less sensitive towards the signals.

resulting voltage distribution is approximated by a Gaussian distribution. The correlation of the mean of these Gaussians for the three target materials and the expected signal in electrons follows a linear function. The determined slope is referred to as gain (in $\mu\text{V}/e$) and describes the induced signal voltage per generated electron-hole pair in the sensor bulk. This procedure can be repeated for every pixel in the irradiated region and a reference region. The number of generated electron-hole pairs is expected to be constant over the applied dose, as ionizing radiation does not effect the sensor bulk, primarily. Therefore, this method allows the investigation of the amplification of the signal during the irradiation study.

The hit map of the sensor during this irradiation is shown in Figure 5.6b. The shadow regions on the sensor matrix with less signal are shielded by the screws which hold the source holder and the lead shielding in place during the other measurement steps. The measurement ran for about 15 minutes for each target material to get about 1000 hits per pixel. Two pixels inside the irradiated region showed many noise hits during the whole study, also before irradiation. Both pixels were therefore masked during the whole analysis procedure.

5.2.5. Strontium-90 Measurement

The measurements with charged particles in this study were performed with a β^- emitter: a ^{90}Sr source with an activity of $2.87 \cdot 10^7$ Bq (status 10.11.2021). During the radioactive process, the radioactive strontium isotope decays into yttrium emitting an electron (0.546 MeV) and a neutrino [Lab05]:



As a neutral particle with vanishing cross section, the neutrino is not detected by the sensor. The yttrium mainly decays fast under emission of a highly energetic electron (2.282 MeV) into a stable zirconium isotope. The energy deposition of the charged electrons follows a Landau distribution, described in Section 2.2.1. As the sensor electronics influence the signal, the distribution has to be fitted with a convolution of a Gaussian function with a Landau distribution.

The measurements with the ^{90}Sr source were performed with the additional source carrier (shown in Figure 5.7a). The carrier led to an increased distance and therefore a broader distribution of the electrons on the sensor matrix. Data was recorded until a majority of the irradiated pixels measured ~ 1000 hits for enough statistics during the analysis. This normally took about 10 minutes. Figure 5.7b shows the hit map of the measurement. After an applied dose of 110 kGy a reduced detection rate is visible. The two noisy pixels inside the irradiated region were masked throughout the analysis.

5.2.6. Analysis Procedure

The analysis considered only data from the irradiated region and an adjacent area trimmed to the same threshold. Each region contained 591 pixels. The unirradiated region is also referred to as shielded region. Each hit of the collected data from the entire sensor matrix includes hit position (column and row), time stamp and ToT information. To minimize the necessary computing capacity, sorted data files were analysed, each containing only the pixel data from the analysed region at the respective dose step. Figure 5.8 shows the two analysed regions during a measurement with molybdenum. Each of the 18 measurement steps included:

- the S-curve measurements for each pixel in the analysed region,
- files with results of tuning procedure with TDAC, threshold, and noise parameters,
- data of three X-ray measurements with different targets (Mo, Ag, and In),
- data of ^{90}Sr measurement.

Masking of noisy pixels, the conversion of the ToT data with the parameters of the ToT calibration and a clustering algorithm are required for the analysis.

5.3. Characterization before Irradiation

As we aim to investigate the dose effects of ionizing radiation, a careful characterization before the irradiation is necessary. Sections 5.3.1 and 5.3.2 outline the tuning procedure and ToT calibration. R. Schimassek implemented both procedures and described them in [Sch21b].

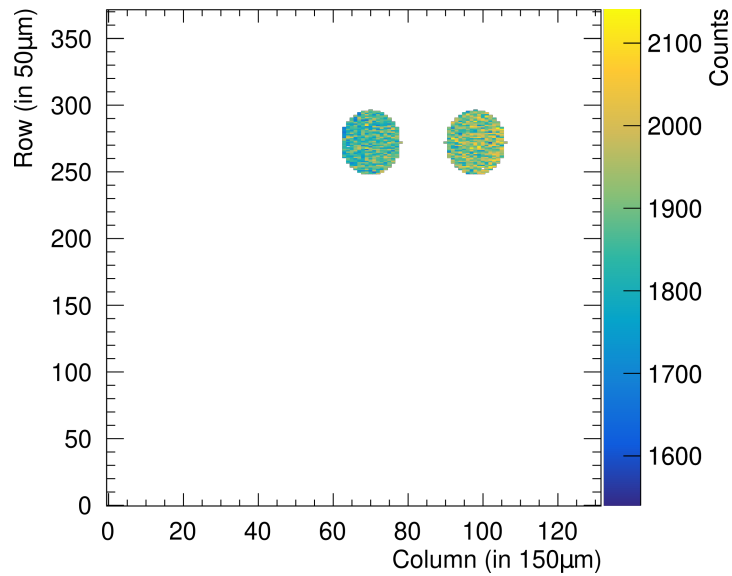


Figure 5.8.: Hit map of the analysed regions on the sensor matrix – During the evaluation of the data, two regions trimmed to the same threshold were analysed. Here, the pixels of these regions are shown during a Mo measurement at a dose of 0 kGy. The gradient in the rate can be explained by the distance of each region to the molybdenum target.

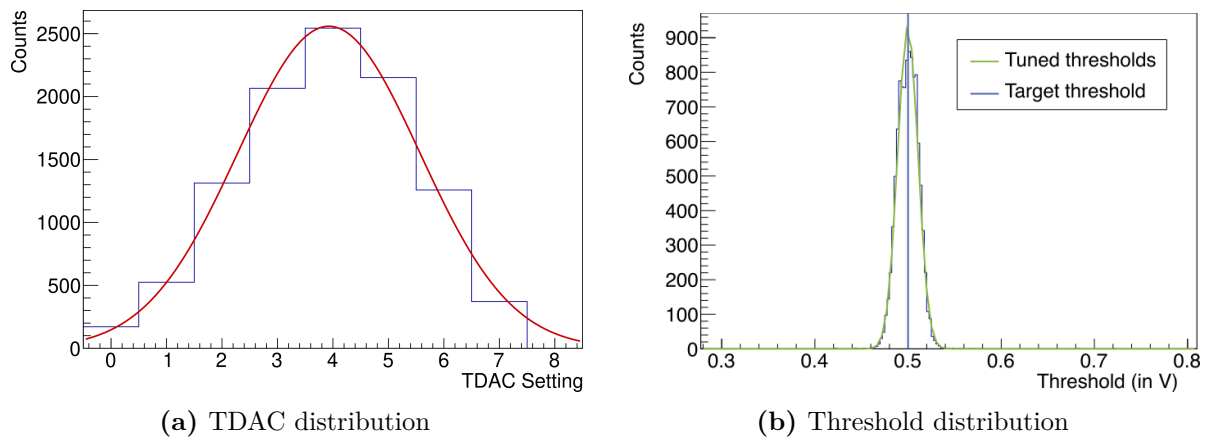


Figure 5.9.: Threshold tuning procedure: TDAC and threshold distribution – The plots show the distributions after the tuning procedure: (a) Distribution of TDAC values in trimmed region with mean $\mu = 3.93$ and standard deviation $\sigma = 1.64$. (b) Threshold distribution with a target value of 0.5 V.

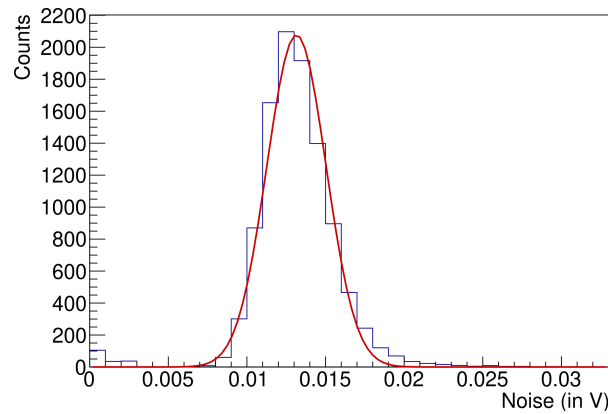


Figure 5.10.: Noise distribution after tuning procedure – The noise of a pixel is measured as the transition width of the S-curve. In this plot, the distribution of the noise before irradiation is fitted with a Gaussian function. This leads to the parameters of mean μ and standard deviation σ : $\mu = 13.15$ mV, $\sigma = 1.88$ mV.

5.3.1. S-Curve Detection and Tuning

The measurement of the ToT value is sensitive to the threshold. As the matrix consists of 49 104 pixels, a careful calibration has to be performed to get similar threshold values throughout the matrix. An 8-bit register in the configuration file regulates the value of the global threshold of the sensor. Additionally, each pixel of the ATLASpix3 has a built-in 3-bit tuning DAC (TDAC) that is adjusted during the tuning procedure, trying to reach threshold values close to the set target threshold. To guarantee sensitive pixels throughout the irradiation, the tuning procedure was performed after every irradiation step. As a scan of the whole matrix can take 16 hours or more, only the irradiated and an adjacent region for comparison were tuned. Figure 5.5 shows this rectangular region.

To achieve a uniform threshold distribution, the tuning procedure adjusts the TDAC value of every pixel. The TDAC allows values from 0 to 7. Figure 5.9a shows the expected Gaussian shaped distribution in this range. A mean of $\mu = 3.93$ – near the parameter average of 3.5 – and the full usage of all TDAC values hints to a reasonable configuration and measurement. For the primary characterization, the global threshold had a value of 180 and Figure 5.9b shows the sharp threshold distribution around the set target threshold value of 0.5 V. The width of the transition of a measured S-curve gives the noise of the pixel. The initial noise distribution in Figure 5.10 of the trimmed region has a mean of $\mu = 13.15$ mV.

The dispersion of these parameters during irradiation is part of this studies and is discussed in Section 5.4.

5.3.2. Time over Threshold (ToT) Calibration

The ToT calibration was performed only once before irradiation, as the procedure has a duration of several hours for the whole matrix and the dispersion in this property is expected to be neglectable. The parameters of the single measurement were used to calibrate the sensor signal throughout the irradiation procedure.

During the calibration, a correlation between the induced voltage signal and the generated ToT signal is found for every pixel. The following logarithmic function describes this correlation:

$$ToT = a \cdot \log\left(\frac{V - V_0}{V}\right) + b \cdot V + c. \quad (5.3)$$

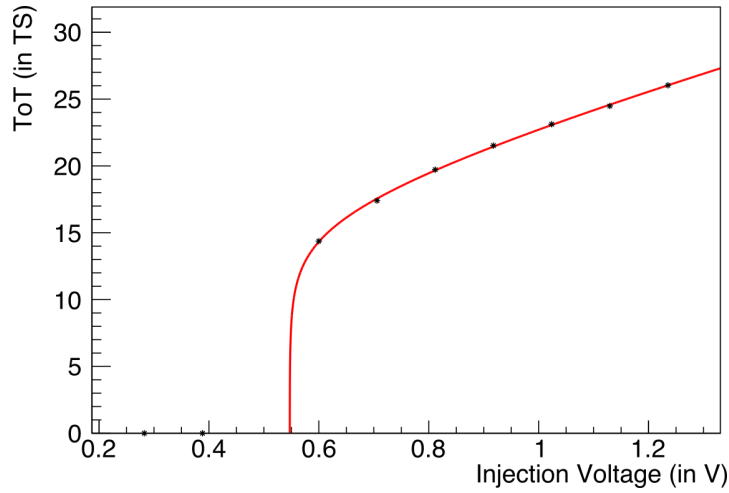


Figure 5.11.: ToT calibration curve of pixel (0|0) – The correlation between the injected voltage and the ToT for every pixel is important for the conversion of a signal’s ToT into a charge.

Figure 5.11 shows an example fit for pixel (0|0) with the following fitting parameters:

$$\begin{aligned}
 \text{voltage offset : } & V_0 = 0.547 \text{ V} \\
 \text{log scale : } & a = 1.904 \text{ TS} \\
 \text{linear scale : } & b = 10.739 \text{ TS/V} \\
 \text{y-offset : } & c = 12.331 \text{ TS} .
 \end{aligned}$$

The unit TS stands for the timestamp unit and depends on the configuration settings for the sensor. During the following studies, one timestamp had a length of 200 ns. The ToT signal must be converted into a voltage with these parameters. Here, V describes the signal voltage which we are interested in. The Lambert W function describes the branches of the inverse relation of the function

$$f(w) = w \cdot e^w, \quad (5.4)$$

and is needed to compute the signal in volts:

$$\text{signal (ToT; in V)} = \frac{a}{b} \cdot W \left[\frac{b \cdot V_0}{a} \cdot \exp \left(\frac{\text{ToT} - c - b \cdot V_0}{a} \right) \right] + V_0. \quad (5.5)$$

A numerical implementation in C++ to perform the calculations with the Lambert W function is used in the analysis [Veb12].

The conversion of the voltage signal into electrons can be based on correlations determined in earlier measurements. In a measurement with a ^{55}Fe source, [Sch21b] finds the linear correlation to be:

$$\text{signal (ToT; in } e^-) = \frac{\text{signal (ToT; in V)}}{0.211 \text{ V}} \cdot 1638 e^-. \quad (5.6)$$

This correlation is used for the calculations in Chapter 6. In this chapter, emitted photons with defined energies of different K_α -lines are used to calibrate the signal voltage.

$$\text{signal (ToT; in } e^-) = \frac{\text{signal (ToT; in V)}}{\text{gain (in } \mu\text{V}/e^-)}. \quad (5.7)$$

The determined gain (in $\mu\text{V}/e^-$) describes the correlation between the signal voltage and the generated electrons in the sensor. Section 5.2.4 describes the implementation and the results of this energy calibration.

For a hit in the sensor, only the ToT is measured and not directly the signal height. Therefore, the ToT properties have to be known precisely. The ToT depends on many factors in the readout chain and – during irradiation with ionizing particles – several components could be affected. As damage of the sensor bulk is not expected by ionizing radiation, no change in the signal height is predicted. Thus, one can assume surface damage as a cause of possible dispersions in the characteristics.

5.4. Test Signal Measurements

After every irradiation step and a 15-minutes relaxation time, an S-curve scan for pixels inside the irradiated region was performed. The target threshold of the tuning procedure was compared to the mean threshold of this scan and adapted if necessary. This tuning procedure was performed in both analysed regions, so the results can be compared. The decrease in the threshold values in the irradiated region is described in Section 5.4.1. The corresponding TDAC values are discussed in Section 5.4.2. As expected, increased noise is visible in the irradiated region, addressed in Section 5.4.3.

A large decrease in the detection efficiency of X-rays and electrons from a ^{90}Sr source in the irradiated region was visible after an applied dose of 10 kGy. To increase the detection efficiency, the global threshold was changed from originally 180 to 177. This reduction of the global threshold after the first irradiation step has to be considered throughout the discussion of results.

The tuning of the depicted area in Figure 5.5 took 1 hour and 31 minutes. To save time, this region was reduced during some measurement steps. Therefore, the statistics of the test signal measurements is reduced at some dose steps. This reduction only is relevant for the shielded region and not for the irradiated part, as those pixels were fully analysed at every dose step. At the dose of 20 kGy, the test signals for the left region are missing completely.

All uncertainties of this section were calculated with σ/\sqrt{N} . Here, σ is the standard deviation of each Gaussian fit to the respective distribution and N is the size of each data set.

5.4.1. Dispersion of Threshold Values

Figure 5.12 shows the development of the threshold over the dose. The histogram of the upper plot shows the distribution of the threshold values after the tuning procedure. The mean of this distribution, compared with the mean values of the non-irradiated region is depicted in the lower plot.

A decrease of the threshold values for both regions is visible throughout the irradiation study, as the threshold follows the target values. The target values were chosen to be lower throughout the irradiation steps, as the mean of the S-curve transitions in the rectangular small region inside the irradiated are (Figure 5.5) suggested decreasing threshold values. The stepwise course is explained by the target values which did not change at every dose step.

The mean threshold of both regions is similar for every irradiation step, as they were tuned to the same threshold value. The irradiation does not seem to disturb the tuning procedure. The same development of the threshold of both regions is an important finding for later analyses and allows the comparison of the results in the two regions.

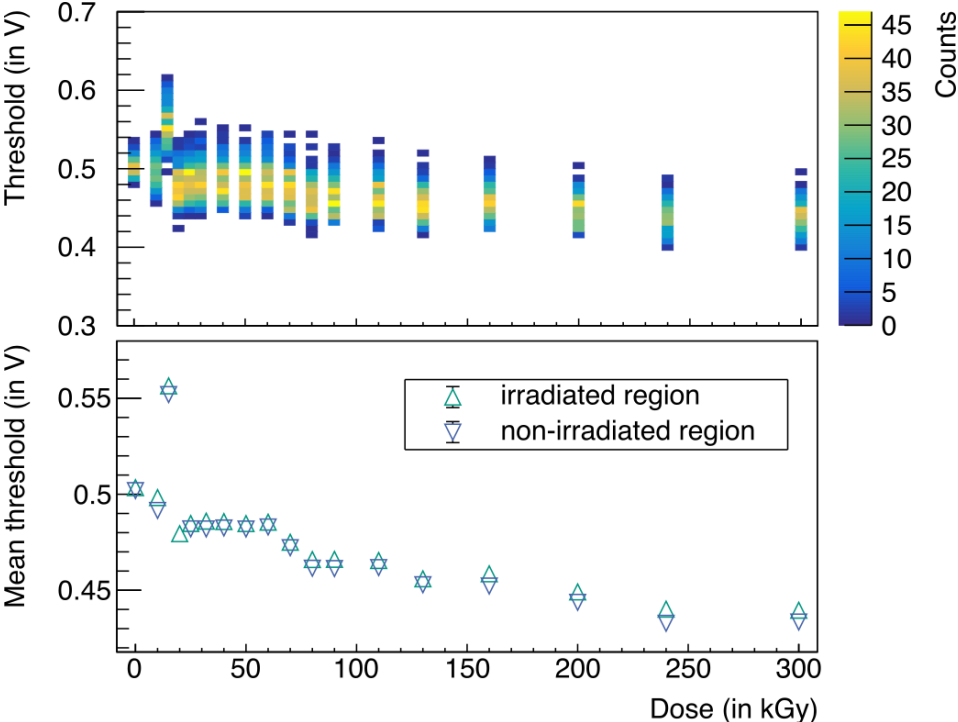


Figure 5.12.: Threshold dispersion in comparison with non-irradiated region – The upper plot shows the distribution of threshold values in the irradiated region for each irradiation step. The lower plot compares the mean threshold values of the irradiated and the shielded region. All uncertainties are estimated by error propagation of the standard deviations.

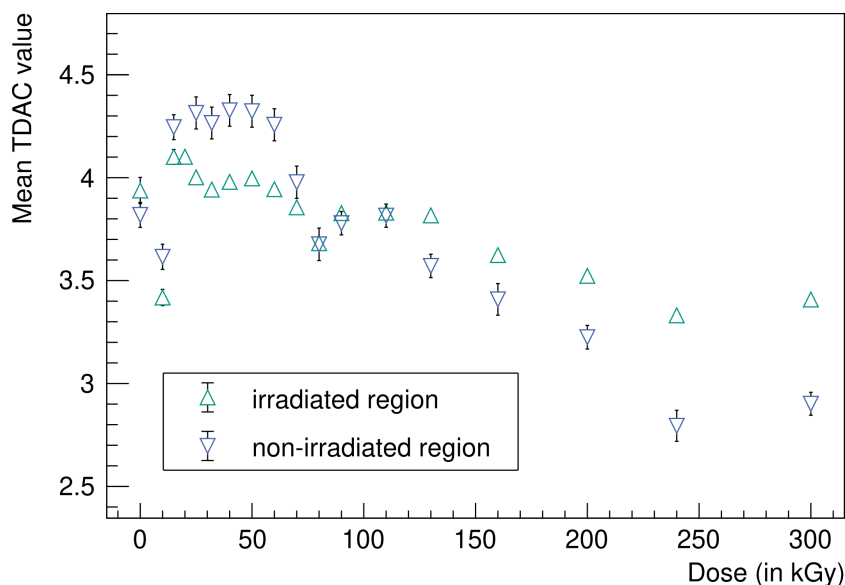


Figure 5.13.: TDAC dispersion in comparison with non-irradiated region – A steady decrease in the mean TDAC values is visible due to reduced threshold target values. The larger uncertainties for the shielded region are explained by smaller datasets. To save time, the size of the tuned region was reduced occasionally. Therefore, the statistics in the unirradiated region is smaller for some steps. The tuning measurement at a dose of 20 kGy did not consider any pixels of the non-irradiated region. All uncertainties are estimated by error propagation of the standard deviations.

5.4.2. Dispersion in Tuning Values

The TDAC value is responsible for the optimal adjustment of the local threshold of each pixel. The decrease of the target threshold voltage is therefore reflected in a reduction of the mean TDAC value. This effect is visible in the non-irradiated region (blue), as shown in Figure 5.13.

In the irradiated region, a decrease of TDAC values is observed as well but the effect is smaller. This indicates that the irradiation has a coincident effect as lowering the TDAC values. A lowering of the thresholds seems to have occurred by the irradiation.

The uncertainties on the mean TDAC values of the shielded region are higher than in the irradiated region. This is a result of the lower statistics in this region, as explained above.

5.4.3. Dispersion of Noise

The upper plot in Figure 5.14 shows the noise distribution in the irradiated pixel region. The width of the distribution hardly changes. As discussed before, the pixel noise is determined by the transition width of the S-curves. An increase of the noise is visible in the irradiated region, whereas the noise in the shielded region stays constant. The increase of noise seems to be a local effect, caused by the ionizing radiation.

5.5. Measurements and Calibration with X-Rays

In the previous section, all signals were injected via the injection circuit and are passed on to the amplifier from there directly. The measurements for this section were performed with photons from an X-ray illumination via three target materials: molybdenum (Mo), silver (Ag)

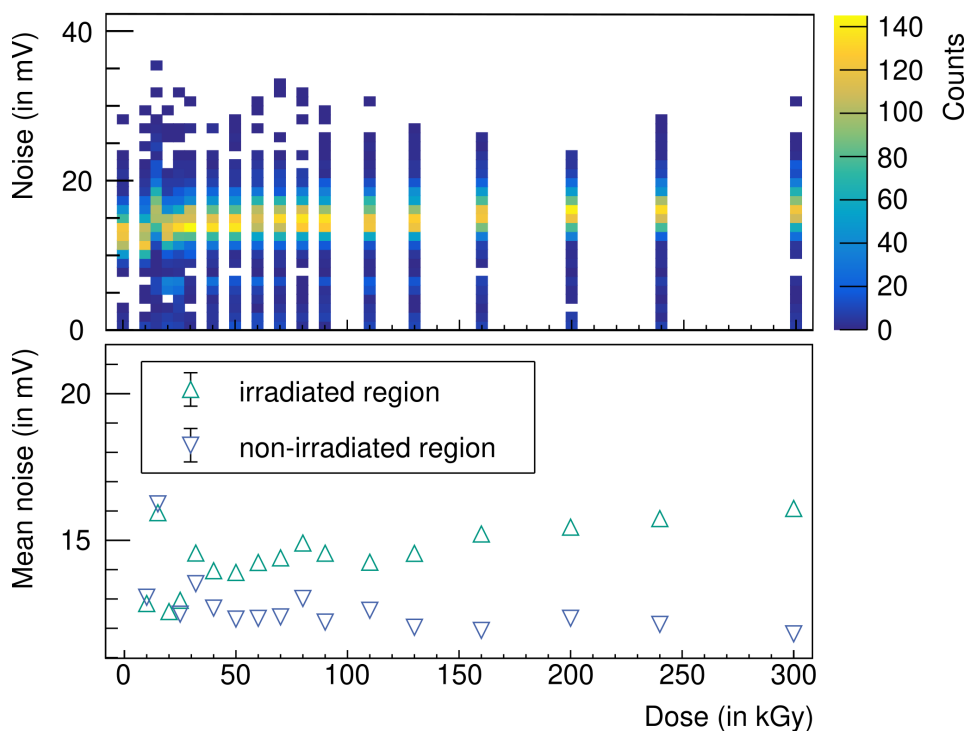


Figure 5.14.: Noise dispersion in comparison with the non-irradiated region – The upper plot shows the distribution of noise values in the irradiated region for each irradiation step. The lower plot compares the mean noise values of the irradiated and the shielded region. All uncertainties are estimated by error propagation of the standard deviations.

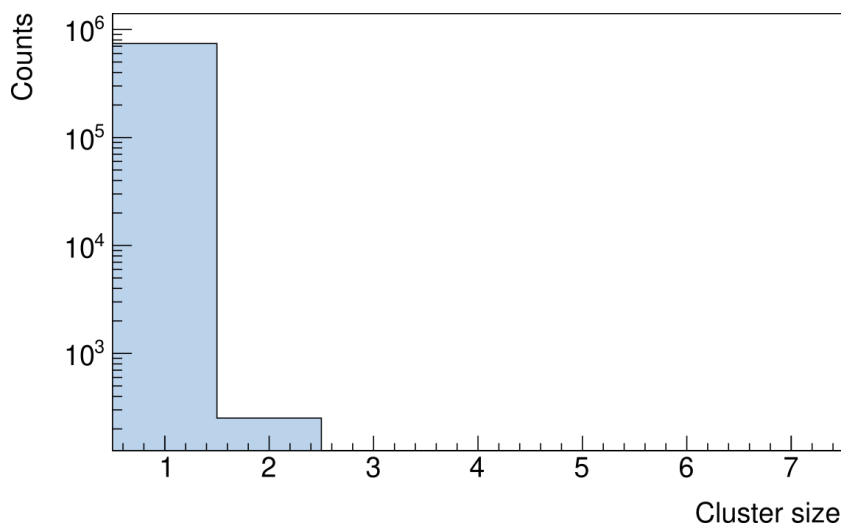


Figure 5.15.: Cluster size distribution of photon signals – The punctiform energy deposition of photons results in a maximum cluster size of two. No clusterization of the data is performed, as the rate of single pixel hits is three orders of magnitude higher.

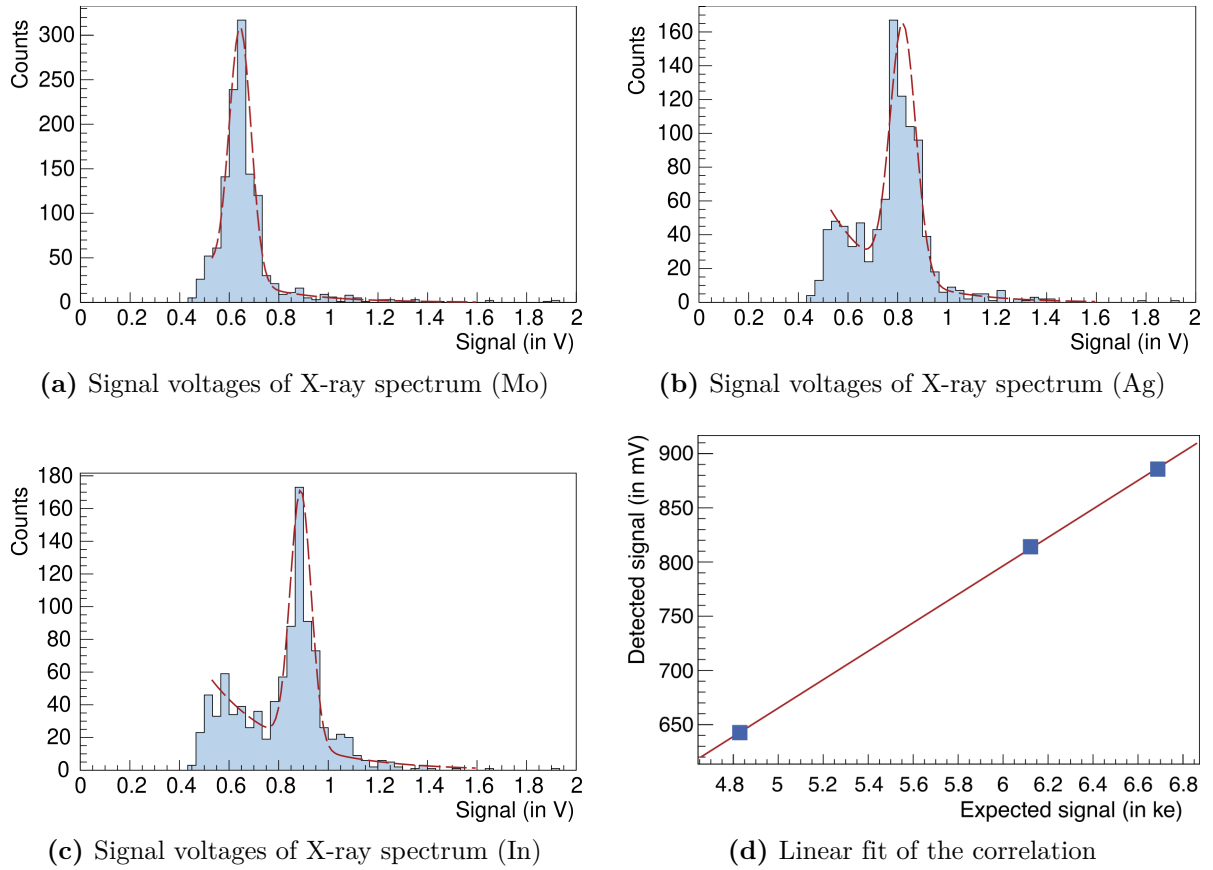


Figure 5.16.: Example of calibration procedure for pixel (72|252) – The mean values of the Gaussian fits are plotted as a function of the expected signal in electrons. The slope of the linear fit is the individual pixel gain (in $\mu\text{V}/e^-$). Systematic uncertainties in the ToT calibration are expected to only shift the linear function in (d) up and down which does not affect the slope. Therefore, these uncertainties are not regarded for this analysis.

and indium (In). Photons interact electromagnetically with the atoms of the silicon lattice and generate signals in form of electron-hole pairs in the sensor diode. The separation and collection of the charge took place at a depletion voltage of 20 V, corresponding to a depletion depth of $38.5 \mu\text{m}$ [Sch21b].

For energy calibration, the induced voltage signal was compared to the expected signal in electrons. Due to the photoelectric effect, an emission of monoenergetic photons from the target is expected. The approach of the energy calibration for the analysed pixels is described in Section 5.5.1. The dispersion of the determined gain is described and discussed in Section 5.5.2. Also, a change in the detection rate was visible in the irradiated region, addressed in Section 5.5.3.

5.5.1. Energy Calibration

The energy desposition of a photon in the silicon sensor is highly punctiform. Therefore, a clusterization of the hits was not necessary. Figure 5.15 illustrates the cluster size distribution during a measurement and motivates this approach. The following section explains the procedure of the energy calibration, using a single pixel (72|252) at a dose of 40 kGy as an example. Figure 5.16 is provided as a summary of this procedure.

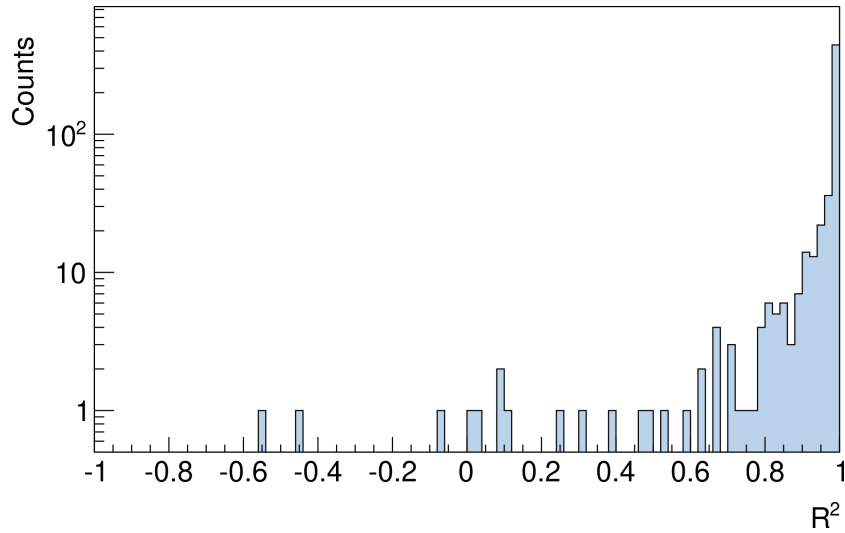


Figure 5.17.: R^2 value distribution of linear gain fits (40 kGy) – The exemplary R^2 value distribution of the 591 gain fits in the irradiated region after an applied dose of 40 kGy shows an accumulation close to one.

Each pixel had seen ~ 1000 hits per measurement. The ToT value from each measured hit was converted into a signal voltage with the parameters from the ToT calibration for the individual pixel. Then, a histogram with the signal voltage distribution for each pixel was created. Figure 5.16a shows the exemplary signal voltage distribution for the indirect X-ray illumination via a molybdenum target in the exemplary pixel. Next to the expected Gaussian shape of the monoenergetic photons, also an exponential noise background was visible in the distribution. Therefore, a combination of a Gaussian and an exponential function was fitted to the distribution. This was repeated for the target materials silver and indium (example plots in Figures 5.16b and 5.16c). A more sophisticated analysis of the background is desiderabile but could not be performed in the scope of this thesis.

As expected, the position of the signal voltage is the lowest for molybdenum and the highest for indium. The mean of the Gaussian share of each histogram is plotted over its respective expected signal in electrons (from Table 5.2). The uncertainty of the mean value is estimated with σ/\sqrt{N} . Here, N is the number of detected signals per pixel and σ is the standard deviation of the Gaussian fit. The resulting linear correlation can be fitted, visualized in Figure 5.16d. The slope thereby corresponds to the searched gain (in $\mu\text{V}/e$).

This procedure is performed for each of the 1182 pixel minus two noisy pixel and for all 18 irradiation steps. To check the quality of the linear fit, the coefficient of determination, referred to as R^2 value was considered. The R^2 value is defined as:

$$R^2 = 1 - \frac{\sum_i (y_i - \hat{y}_i)^2}{\sum_i (y_i - \bar{y})^2}, \quad (5.8)$$

and is used for evaluating the goodness of a regression [Fah+16]. Here, y_i describes a measured value and \bar{y} the mean value. \hat{y}_i is the estimated value of the fit function. R^2 values close to one indicate a good fitting result, as the deviation of the actual and the estimated value is small. Figure 5.17 shows the distribution of R^2 values in the irradiated region after a applied dose of 40 kGy. The distribution shows a concentration close to the value one, for all irradiation steps. Therefore, this method seems valid for most pixels.

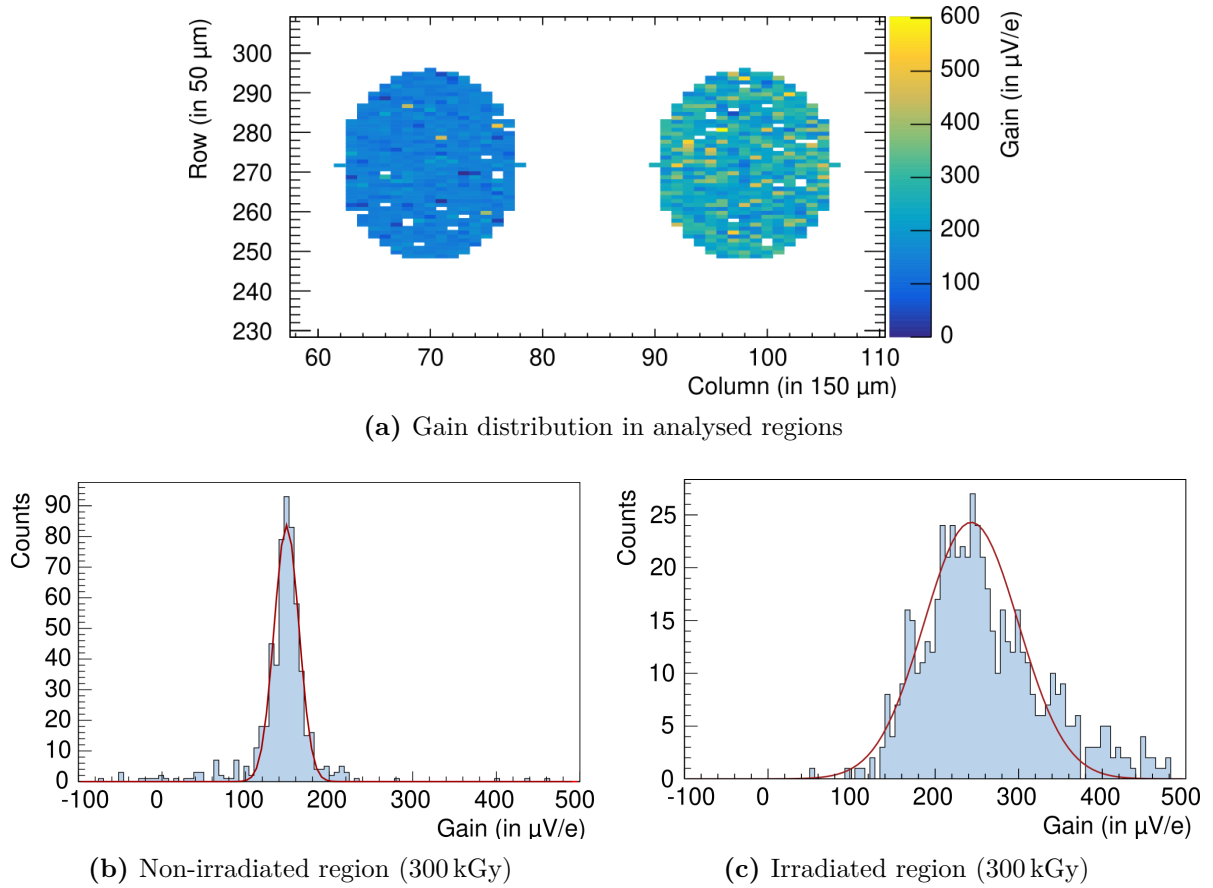


Figure 5.18.: The gain distribution after an application of 300 kGy – (a) The gain distribution after the full applied dose of 300 kGy is illustrated for both regions, the non-irradiated (left) and the irradiated on the right. White bins in the matrix correspond to excluded pixels due to negative values of fitted gain. For better visualization, only positive gain values were taken into account. – (b, c) Due to several outliers a Gaussian fit was performed to determine the mean value.

5.5.2. Gain Dispersion

The determined gain describes the induced signal voltage in the sensor per generated electron-hole pair. No bulk damage is expected by ionizing radiation, so the number of generated charge carriers is expected to be constant over the irradiation steps. Therefore, the dispersion of the gain is of great interest, as it can be related to induced damage in the pixel electronics.

For each irradiation step, the gain values of the analysed pixels were determined, using the method described above. Figure 5.18a visualizes the gain value distribution in the irradiated and the shielded pixel region after the full applied dose of 300 kGy. For a better visualization, the color map only shows pixel with gain above zero, pixel with values below were not taken into account for this plot. Reasons for negative linear fitting results were e.g. high noise peaks in the signal voltage distribution and due to this a wrong determination of the Gaussian means for silver or indium. The computed gain distributions for both regions are visualized in the Figures 5.18b and 5.18c for the same applied dose. These plots show a variation of the gain values in the left and the right region and motivate a change in the system due to irradiation. The gain distribution in the irradiated region shows a higher mean and a higher

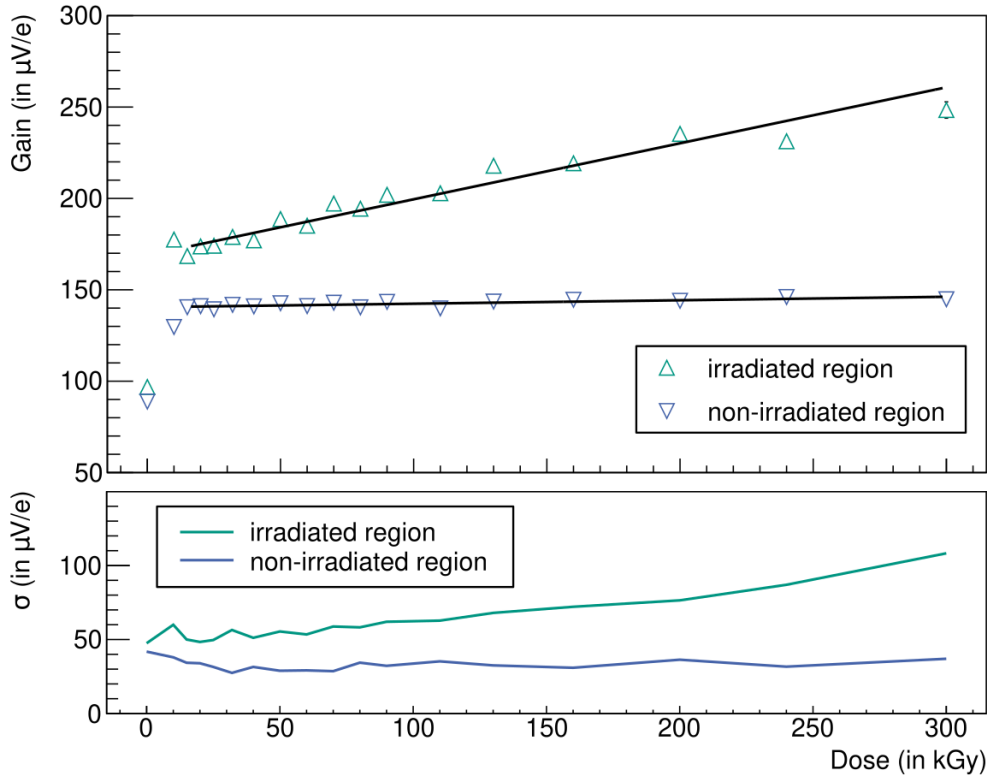


Figure 5.19.: Gain Dispersion with standard deviation – The upper plot visualizes the increase of the mean gain in the irradiated region for increasing radiation doses. The linear fit is only applied for doses above 15 kGy, as the global threshold was changed there. Also, the standard deviation – shown in the lower plot – rises compared to the values of the shielded region.

spread. Because of outliers and to determine the most probable gain more reliably, a Gaussian fit was performed for each gain distribution.

The mean values of these fits in both regions and for every irradiation step are illustrated in the upper plot of Figure 5.19. The lower plot in Figure 5.19 shows the development of the standard deviation of the Gaussian fit with the applied dose. An increase in the values of the irradiated region is visible whereas the standard deviation in the shielded region stays constant.

The initial gain before irradiation lies around $90 \mu\text{V}/e$ in both regions. The applied radiation dose of 10 kGy leads to a strong increase of the gain in both pixel regions. After lowering the global threshold from 180 to 177, the gain value stays almost constant in the shielded region. In the irradiated region, the gain rises with the applied dose. Both progressions were fitted linearly to compare the trends:

$$gain(dose) = m \cdot dose + c. \quad (5.9)$$

As we lowered the threshold at a dose of 15 kGy, the dose steps below were ignored for the linear fit. Table 5.3 presents the linear fit parameters for the gain dispersion and also the fitting uncertainties are given for both regions. An increase of the gain by $0.306 \mu\text{V}/e^-$ per dose step (in kGy) is visible. As expected, the shielded region shows hardly any change. This hints at an increase of the gain and changes in the signal processing due to ionizing radiation. The possible causes for the slope change were analysed. Figures 5.20a and 5.20b compare the development of the signal voltage of the three target materials in both regions. The increase of

Table 5.3.: Fit parameters of the gain dispersion with uncertainties

Region	m	c
Shielded	0.306 ± 0.010	168.890 ± 0.943
Irradiated	0.019 ± 0.004	140.493 ± 0.520

the gain has its origin in an amplification increase, depending on the signal size. The signals in the non-irradiated region have a uniform small increase for all three target materials. This can be explained by a decrease of the threshold, visible in Figure 5.12, as the ToT depends on the threshold height (Figure 3.5).

The increase of the signal voltage in the irradiated region is steeper and in addition, the large signals of the indium X-ray spectrum are amplified stronger than the smaller signal of the molybdenum spectrum. This leads to the increase of the slope during the energy calibration, referred to as gain. Therefore, the dispersion of the amplification depends on the signal strength.

Discussion of Results The observed change in the amplification could have several reasons. The number of collected electrons is expected to stay constant during irradiation with X-ray photons. Due to a large fill factor design a reduced efficiency in the pixel edges is not expected and has not been observed in earlier studies [Aug+19]. Therefore, the increase of the gain is expected to be a result of changes in the amplification inside the pixel electronics. Still, this could result from three origins:

1. Decrease of the threshold in the comparator.
2. Change of the amplification (related to the signal height).
3. Shift of feedback current (related to the signal length).

A change of the comparator properties should result in a change of the threshold. As no dispersion of the threshold is visible if both regions are compared, this seems not likely. Instead, the increase in gain indicates a change of the signal amplification which could have either of the following causes:

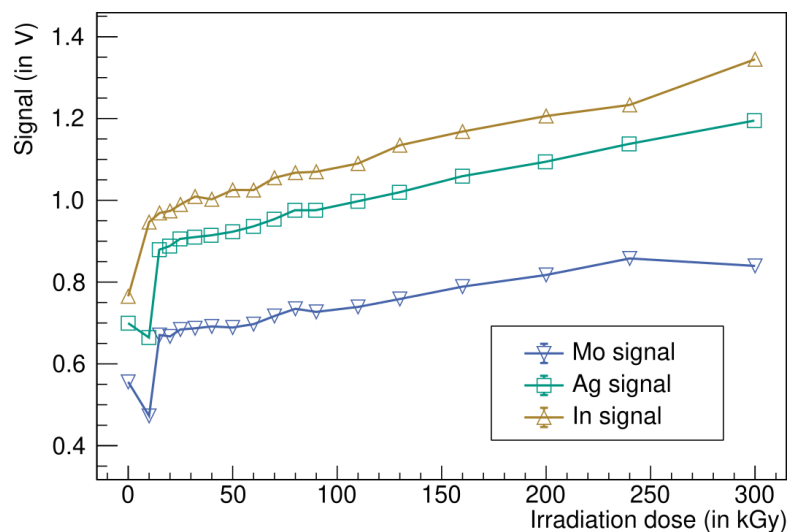
- The feedback circuit in the amplifier regulates the length of a signal and therefore the determined ToT. Larger ToT values due to change in the feedback would lead to an increased calculated signal voltage, and therefore to an increased gain.
- The amplifier itself regulates the height of the signal. Changes in the characteristics of the amplifier could lead to a larger signal and increased ToT values. This increase of amplification could also explain the course of TDAC values in Section 5.4.2.

Further analyses that are beyond the scope of this thesis can be done partially with the existing data to further narrow down the cause.

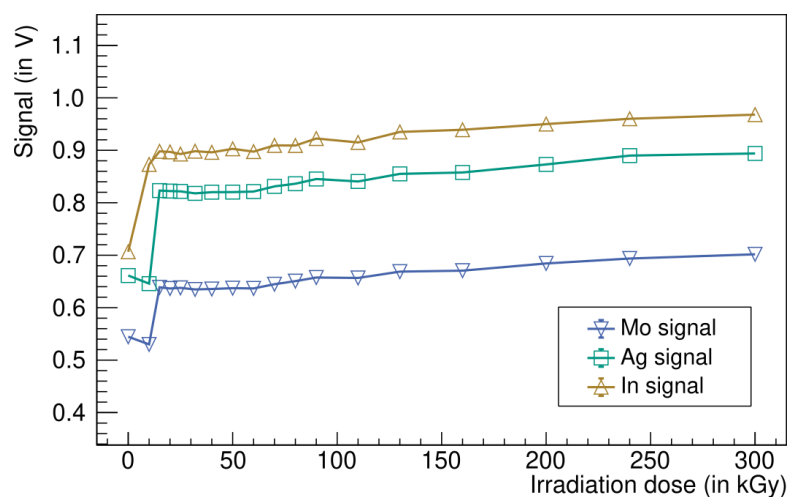
5.5.3. Dispersion of Detection Rate – Indirect X-Ray Irradiation

In addition to the increase of the gain, a decrease in the detection rate is visible in the hit maps of the measurements (Figure 5.6b). To quantify this reduction, the ratio of hits per pixel of the two regions was compared.

The left region showed a reduced signal rate before the actual irradiation. The hit map in Figure 5.8 shows a slightly higher rate in the right region at a dose of 0 kGy. This difference



(a) Dispersion of the reconstructed X-ray signal voltage in the irradiated region



(b) Dispersion of the reconstructed X-ray signal voltage in the shielded region

Figure 5.20.: Dispersion of X-ray signal voltages – (a) An increase in the signal voltages of the irradiated region is visible. The increase in amplification depends on the size of the signal: The increase of large signals (indium) is stronger than for smaller ones (molybdenum). This results in an increase of the gain over the dose. (b) A slight increase in the signal is due to a lowered threshold. The increase in the shielded region is less distinct than in the irradiated region and independent of the signal size. All uncertainties are estimated by error propagation of the standard deviations.

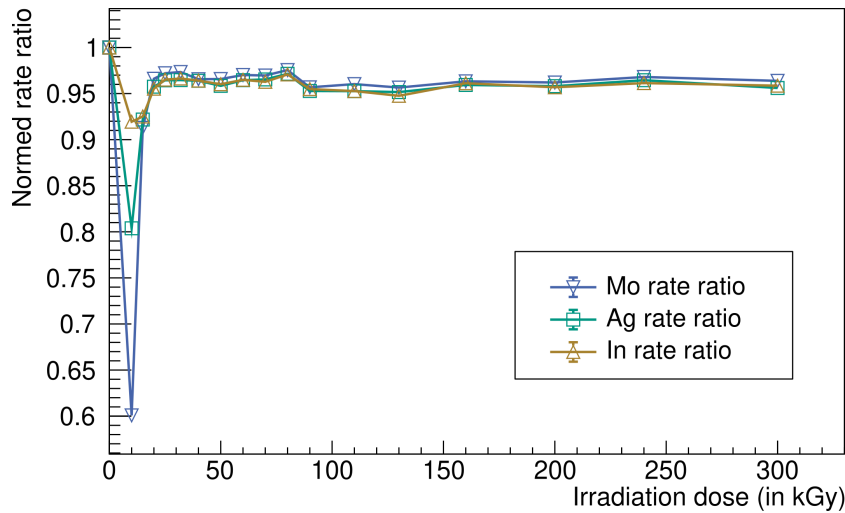


Figure 5.21.: Detection rate ratio of X-ray signals at different irradiation steps. – The plotted value describes the ratio of hits per pixel in irradiated region to the hits per pixel in the shielded region. A value of 1 indicates the same result as before irradiation. Values below one indicate a reduced detection rate in the irradiated region. A sharp drop in the detection rate ratio is visible for all three target materials at a dose of 10 kGy. Then the ratio stabilizes. All uncertainties are estimated by error propagation of the standard deviations.

is probably geometrical and due to the smaller distance to the target of the right region. Therefore, all computed rates were normalized to the ratio of the values before irradiation. In the irradiated region two noisy pixels were masked throughout the analysis, so only 589 pixels were considered for the number of hits per pixel.

At a dose of 0 kGy, the plot in Figure 5.21 then shows a ratio of one for all target materials. At a dose of 10 kGy a large decrease in the detection rate of the irradiated region is visible for all three target materials. After setting a new threshold value, a reduction at 15 kGy is still visible. For higher doses, the detection rate ratio is relatively constant but still reduced. The full detection rate is not recovered again. During the measurement, all pixels remained active and no excessive noise was registered.

As pointed out in 5.2.2, anormal behavior for similar doses was registered with another sensor chip by F. Ehrler. There, it is pointed out that a possible cause is the generation of surface charges in the sensor which are compensated by interface traps at higher doses [Ehr15].

5.6. Measurements with Charged Particles

A ^{90}Sr source allowed the signal measurement with charged particles. The results of this study are presented in the following section. The expected and the actual outcome of the measurements are summarized in Section 5.6.1. Section 5.6.2 describes the measured dispersion in the detection rate ratio. Changes in the cluster size distribution are discussed in Section 5.6.3, and Section 5.6.4 summarizes the evolution of the leakage current.

5.6.1. Strontium-90 Signal Detection

As the energy deposit of MIPs in thin HV-CMOS sensors is Landau-distributed, charge sharing effects between pixels cannot be neglected. Low energetic particles deposit a high energy

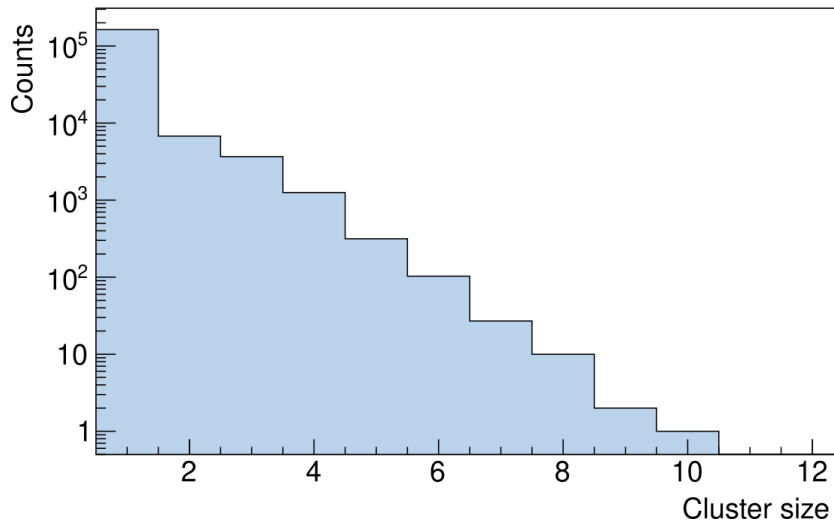


Figure 5.22.: Cluster size distribution – We implemented a clustering algorithm to find typical cluster sizes during the ^{90}Sr measurement.

amount while traversing the sensor and can lead to signals in several pixels. Figure 5.22 shows the cluster size distribution in the right region at 0 kGy. The necessity of hit clustering for further analyses is clear, as more than 10 % of the charged particles deposit energy in more than one pixel. The clustering algorithm takes into account the time and position of the hit occurrence. Hits in adjacent pixels with similar timestamps are combined to a cluster. Spatial and time cuts in the clustering algorithm were set to $\Delta x \leq 450 \mu\text{m}$ (three column widths), $\Delta y \leq 150 \mu\text{m}$ (three row widths), respective $\Delta t \leq 400 \text{ns}$ (two timestamps). The ToT values of all hits in a cluster are converted to a signal voltage. The sum is then considered as the signal voltage of this clustered hit. All analysis steps with the ^{90}Sr data were performed after hit clustering.

The initial idea behind the measurement with charged particles was to prove the neglectable bulk damage by X-ray irradiation. After a conversion of the signal voltage into the number of generated electrons with the gain determined, a stable MPV of the Landau Gaussian distribution is expected. On the other hand, a visible increase of the amplification by a shift in the signal voltage MPV could have supported the results from the X-ray measurements (Section 5.5). A validation of these expectations was not possible, as the chosen threshold unintentionally was too high to measure the maximum of the distribution. Figure 5.23 shows the signal voltage distribution in the exemplary pixel (98|255) after the full applied dose of 300 kGy. The black curve describes the S-curve with the fit parameters for this individual pixel from the tuning procedure, described before. The MPV of the possible Landau distribution is cut off by the threshold. In his work, R. Schimassek predicts an MPV of 0.292 V for ^{90}Sr signals at a depletion voltage of 20V [Sch21b]. The predicted MPV value is drawn in green. To measure the full Landau Gaussian distribution, including the MPV, the threshold would have had to be below the 0.292 V. Instead, with a mean of 0.45 V, the threshold configuration was too high. The attempt to only fit the upper edge of the distribution fails due to low statistics and the missing MPV. The original goal of proving the negligibility of bulk damage could not be achieved. Instead, attention was put to the charged particle detection efficiencies, cluster sizes, and leakage current dispersion in the following.

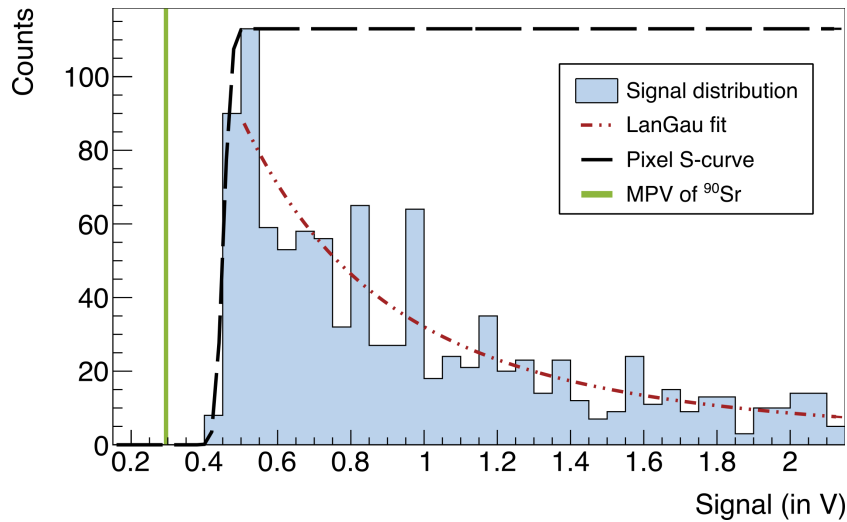


Figure 5.23.: Signal voltage distribution of ^{90}Sr signals – The histogram (blue) shows the signal voltage distribution of an exemplary single pixel (98|255) during an ^{90}Sr measurement after an applied dose of 300 kGy. The S-Curve of this pixel is known due to the tuning procedure. The threshold of the pixel cuts off the distribution. The expected MPV of ^{90}Sr is drawn in green at 0.292 V [Sch21b]. A Landau Gaussian fit (red) is not reasonable due to the small range and low statistics.

5.6.2. Dispersion of Detection Rate – Charged Particles

The hit map in Figure 5.7b shows the detected signals per pixel after an eleven minute measurement with ^{90}Sr at an applied dose of 110 kGy. Again a reduction of the rate is visible in the irradiated region.

In a first attempt, the same method as in Section 5.5.3 was used to determine the detection rate ratio. A strong oscillation in the rate ratio is visible in the red curve in Figure 5.24. To analyse this behaviour, the hit maps of the signals at the maximum and the minimum of this distribution were compared. The determined rate ratio has a peak at the dose of 60 kGy and a minimum at the dose 110 kGy. A comparison of the two hit maps shows an offset between the mean strontium source positions in these measurements. The 2D Gaussian fits applied to the hit maps revealed an offset of at least 2 mm (Figure A.1). The printed source carrier (Figure 5.7a) should have prevented a movement of this scale. Therefore, it can be assumed that the active part of the source is not symmetrically positioned inside its protective housing.

In the second attempt, the Gaussian profiles of the hit map of the ^{90}Sr measurements at the different doses were considered. To determine the fit parameters of the 2D Gaussian distribution we rejected the trimmed area, including the irradiated region. This was because of the inconsistent rate over the hit map. The fit parameters were then used to determine the expected rate in the center of each analysed region:

$$f(x, y) = \exp\left(-\left(\frac{(x - x_0)^2}{2\sigma_x^2} + \frac{(y - y_0)^2}{2\sigma_y^2}\right)\right). \quad (5.10)$$

This value was used to normalize the rate. As this method is not exact, only the ratios for dose steps with significant maxima and minima in the red curve were calculated this way. For a further analysis, the full profile of the Gaussian distribution should be used to norm the hit rates of each pixel. Nevertheless, the blue curve in Figure 5.24 shows that the effect described

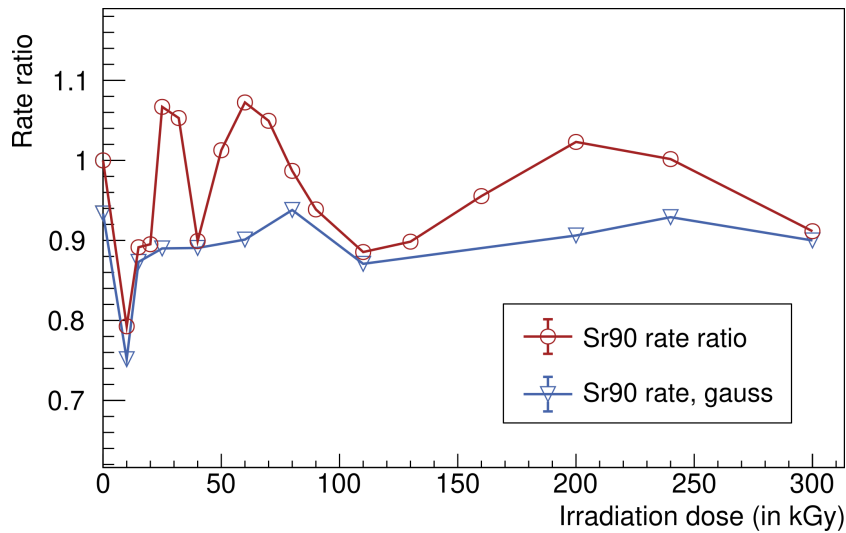


Figure 5.24.: Detection efficiency of ^{90}Sr signals at different irradiation steps. – For the red curve, the rate ratio was determined as for X-ray signals in Section 5.5.3. A strong oscillation is visible due to the non-symmetrical ^{90}Sr source. For the blue curve, at every dose step a 2D Gaussian was fitted to the ^{90}Sr profile. The values of this fit were used to normalize the rate in each region. All uncertainties are estimated by error propagation of the standard deviations.

before is mainly canceled out by this procedure. Again, a significant drop of the rate ratio is visible at the dose of 10 kGy and the ratio is stable for larger doses.

No pixels got insensitive for charged particles throughout the irradiation study. Also, no additional noisy pixels were found.

5.6.3. Cluster Size Dispersion

Additionally, we studied the cluster size dispersion through the irradiation, as this provides information about the sensitivity of the pixels. Figure 5.25 depicts the ratio of clusters with size two to single pixel hits at different dose steps.

At a dose of 15 kGy, a global threshold reduction was performed, thus a higher sensitivity for clusters with charge sharing would be expected. Instead, the plot shows a significant drop of the ratio at this step. This can be explained by a lower threshold resulting in the detection of more particles with a lower energy deposition. Therefore, the probability for hits with charge sharing effects decreases. The Landau distribution with two different thresholds in Figure 5.25 visualizes this effect. Apart from the drop at 15 kGy, a higher cluster size ratio is visible for the irradiated region. This speaks for a slightly higher threshold in this region, confirmed by the results from Figure 5.12.

5.6.4. Leakage Current

Leakage current occurs due to charge generation in the sensor diode. This can be strongly supported by bulk defects, building additional energy levels in the band gap of the semiconductor. In a non-irradiated state, HV-CMOS sensors show very low leakage currents. ATLASpix3 has a leakage current of about 60 nA at a depletion voltage of 20 V. This property is important for the characteristic low power consumption of HV-CMOS sensors and low noise in the sensor. Figure 5.26 shows an increase of the leakage current with a maximum value of 280 nA during a ^{90}Sr measurement. During the measurement with charged particles, the leakage current is

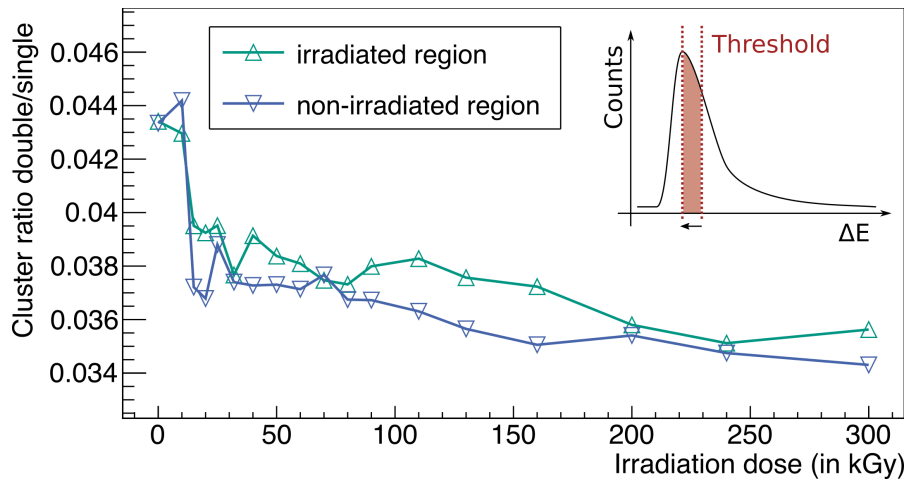


Figure 5.25.: Dispersion of the cluster size ratio with ^{90}Sr – The plot shows the ratio of clusters with size two to clusters with size one. A drop in the cluster size ratio at 15 kGy can be explained with a lower threshold. More signals with a lower energy deposit are detected and therefore, the contribution of clusters with size two becomes less likely.

higher due to the charge generation in the substrate. The increase over the dose corresponds to an increase by a factor of five. The sensors from the beam dump at the HIT Heidelberg show a leakage current three orders of magnitude higher after a similar energy dose deposit of hadrons [Sch21b]. As expected, the share of additional leakage current induced by ionizing radiation is small compared to the effect of heavy particles that lead to bulk damage. Also, a saturation, typical for surface defects, is visible in the curve. For bulk damage, a linear increase of the current with the fluence would be expected [Mol99].

Apart from irradiation, the leakage current is highly sensitive to temperature. The dip at a dose of 130 kGy could be evoked by a direct measurement after cooling the sensor to -18°C . This could lead to an increased leakage current during the tuning procedure due to electronic activity in the matrix. Still, the curves in Figure 5.26 show a higher leakage current during the ^{90}Sr measurement, as there, charged particles generate electron-hole pairs throughout the matrix.

5.7. Summary and Comparison with Beam Dump Studies

In earlier studies, a stack of sensors was irradiated with protons and carbon ions at the beam dump of the HIT facility and later investigated by R. Schimassek [Sch21b]. The irradiation led to the visible effects in the matrix of the ATLASpix3 sensor: A decrease in the detection efficiency of MIPs from a ^{90}Sr source, an increase of the leakage current by three orders of magnitude, and a high noise hit rate in the irradiated region was found for unoptimized settings. The presented study aims to disentangle the radiation-induced effects with ionizing radiation.

In the course of this work, an iterative irradiation procedure for the HV-CMOS sensor ATLASpix3 at the 60 kV X-ray tube of the ETP, KIT, was developed and performed. The collected data was analysed and a comparison of the irradiated region and an adjacent shielded region was performed.

After the full applied dose of 300 kGy, the sensor was still fully sensitive to X-ray photons in the range of 20 keV and MIPs from a ^{90}Sr source. Not a single pixel lost functionality. Also, the tuning procedure remained functional throughout the irradiation.

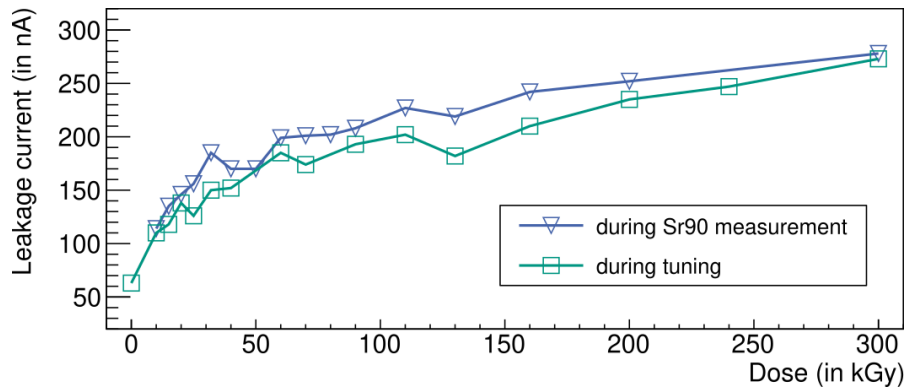


Figure 5.26.: Leakage current at room temperature during ^{90}Sr measurement and tuning procedure over radiation dose – An increase of the leakage current is visible over the applied dose. As an additional current is produced by the generated charge carriers in the sensor bulk during the ^{90}Sr measurement, the leakage current during this measurement is slightly higher. For some dose steps, the leakage current measurement was not performed.

Several smaller dispersions were investigated: The pixel noise increased steadily in the irradiated region and had risen by a factor of 1.45 after the full applied dose. Which is not problematic considering the signal to noise ratio of 26 [Sch21b] for the used depletion voltage of 20 V. Additionally, an increase of the leakage current was visible with a maximum of 278 nA from originally 60 nA. An energy calibration with the X-ray spectra of three different target materials allowed the investigation of an individual pixel gain. A visible gain increase for rising doses speaks for slightly variable amplifier characteristics. This could either have its origin in a change of the amplification, leading to a larger signal or in a dispersion in the feedback current, leading to a change of the signal length. The results show a higher amplification increase for large signals. A comparison of the amplification behaviour for test signals with these results is pending.

At a dose of 10 kGy, a significant decrease of detection efficiency was visible. Smaller dose steps in this region would have been beneficial for further understanding of this phenomenon. In the course of these problems, the global threshold was lowered. An even lower measurement with a threshold below 0.292 V would have allowed further analysis of the ^{90}Sr data.

For further studies, an increase in statistics would be favorable. During the study, the size of the recorded files with a high percentage of hit data from outside the analysed region was problematic. An additional feature in the readout software could directly discard irrelevant data in future studies. Further, a constant target threshold during the trimming procedure would have simplified the analysis of the results. Though, a tuning of the threshold seemed necessary after the large effects seen at the first dose step.

All in all, the effects of the irradiation with hadrons have not been observed with ionizing particles. Therefore, the problematic effects encountered in the HIT beam dump irradiation by R. Schimassek seem to be caused by radiation damage in the sensor bulk.

6

Beam Test – Secondary Particle Tracking

ATLASpix3 (Section 3.4) is a monolithic HV-CMOS sensor with promising technical properties. With this work, an attempt has been made to prove the suitability of ATLASpix3 for secondary particle tracking during medical irradiation treatments (Section 4.2.3). An ATLASpix3 telescope built by R. Schimassek for ([Sch21b]) is used for this effort. To test its suitability for secondary particle tracking, the aim was to test the setup under operating conditions. Therefore, a mechanical setup was designed, constructed, and tested at the beam test area of the Heidelberg Ion Therapy Center (HIT), following the routines of previous studies [Gwo+13]. Attention has been paid to the estimation of particle and data rates at different angles and distances, and the performance of the telescope at tracking secondary particles. The setup was designed in regard to low cost and high availability.

Section 6.1 wraps up the previous studies concerning secondary particle tracking. The new mechanical setup and the properties of the four-layered ATLASpix3 telescope are described in Section 6.2. Additionally, the results of a pre-characterization of the individual sensor layers are given in Section 6.3. The measurement procedure at the beam test at the irradiation facility HIT is described in Section 6.4. The framework *Corryvreckan*, used for the analysis of the beam test data, is outlined in Section 6.5. The steps required to prepare the beam test data for analysis are discussed in Section 6.6. Section 6.7 describes the analysis of the beam test data, performed using *Corryvreckan* framework, as possible in the scope of this thesis. The last Section 6.8 summarizes the results.

6.1. Previous Studies on Secondary Particle Tracking

As discussed before in Section 4.2.3, a real-time and non-invasive monitoring system would improve medical irradiation treatments. Successful studies on secondary tracking have been already performed with the hybrid pixel sensor TimePix in several studies [Gwo+13]. TimePix3 has a pixel pitch of $55 \mu\text{m} \times 55 \mu\text{m}$ and achieved spatial resolutions of up to 1mm^3 in the image reconstruction of the secondary tracks [Poi+14; Rei+17].

For the studies, a polymethyl methacrylate (PMMA) cylinder was used to emulate tissue, as PMMA ($(\text{C}_5\text{O}_2\text{H}_8)_n$) has similar scattering properties to water and therefore, human tissue. Before the development of the Bethe equation (2.8), considering relativistic terms, a classical approach for energy deposit of charged particles in matter was described by W. H. Bragg in 1905 [BK05]:

$$\frac{dE}{dx} \approx \frac{E^{1-p}}{\alpha \cdot p} . \quad (6.1)$$

Here, E is the energy of an incoming beam, and p and α are fit parameters, depending on the scattering material and are very similar for water and PMMA [NZ15]. As PMMA is in addition easy to handle, the energy deposition inside a cylindrical PMMA phantom is studied.

Figure 6.1 shows the schematic of the experimental setup with the cylinder and a multi-layered sensor telescope. Secondary ions are created in nuclear fragmentation processes inside the phantom, and their tracks are measured by the telescope. The origin of the track is correlated to

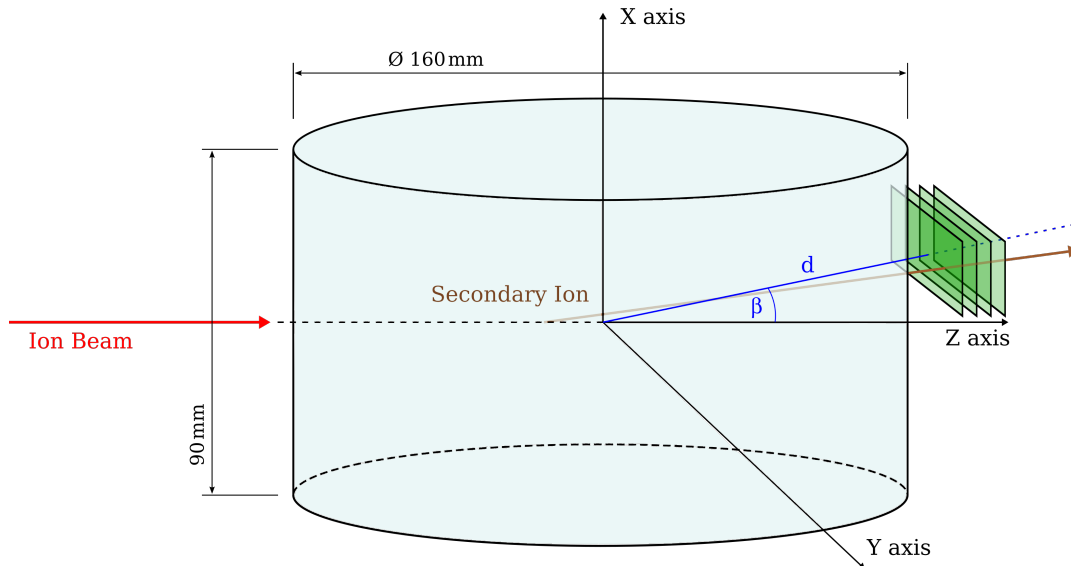


Figure 6.1.: Schematic illustration of experimental setup with PMMA cylinder and sensor telescope. – The primary ion beam runs along the z axis, while the center of the homogeneous cylindrical PMMA phantom is located in the center of the cartesian coordinate system. Throughout the experiments, the four sensor layers of the ATLASpix3 telescope are placed at varying distances d from the center and angles β with respect to the z axis. Fragments which are produced by ions interacting with the PMMA cylinder are mainly scattered in forward direction. (based on [Rei+17])

the Bragg position inside the tissue. Several approaches can be made to determine this secondary origin inside the PMMA cylinder. A. Reinhart uses a three-dimensional reconstruction tool based on maximum likelihood expectation maximization in [Rei+17]. A simpler way to find the origin of the secondary tracks are back-projection methods. In [Sch21c], the track position with the least distance to the expected beam axis is assumed as track origin. K. Gwosch performs a 2D projection on a plane spanned by the beam axis and the x axis. Both methods require an a priori assumption of the beam position.

The predicted shape of the 2D back-projection distribution of secondary tracks is shown in Figure 6.2. [Gwo+13] describes two methods of finding a correlation between the shape of distribution and the position of the Bragg peak. A decrease of the rate throughout the tissue is visible for the distal edge of the back-projection distribution, shown in Figure 6.3. A change of the slope (pink line) in this distribution indicates the position of the Bragg peak. A clear correlation is also visible between the position of the Bragg peak and the position where the linear fit of the distal decline reaches 50% of the maximum (light blue dashed line). Here, the Bragg peak is illustrated by a red curve.

The studies performed in this thesis were guided by these studies, and their results. However, the development of a sophisticated reconstruction algorithm was beyond the scope of this thesis.

6.2. Experimental Setup

The distribution of secondary ions from a ion beam interacting with a PMMA cylinder and the origin of their tracks are measured with a silicon sensor telescope. A sketch of the required setup is shown in Figure 6.1. A mechanical setup for automated positioning the telescope behind the PMMA cylinder had to be developed and built for the studies, and is described in

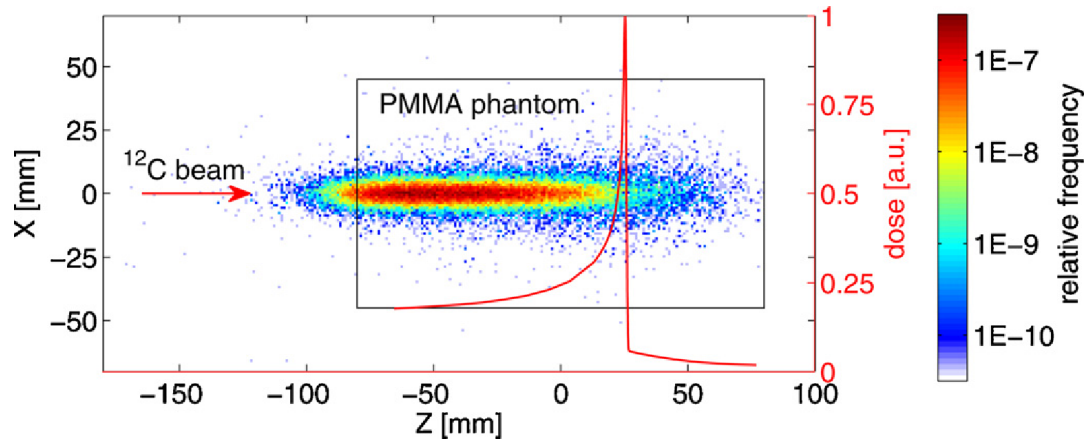


Figure 6.2.: Distribution of back-projected secondary ions throughout the PMMA cylinder. – In the studies of K. Gwosch et al, tracks of the secondary ions originating from the primary ion beam in the PMMA cylinder were back-projected onto the vertical beam plane. The plot shows the distribution throughout the PMMA cylinder (black rectangle). A clustering of the distribution can be observed at the outer area of the cylinder. Initial carbon ion beam parameters for this plot were: $E = 250.08 \text{ MeV/u}$, $\text{FWHM} = 4.3 \text{ mm}$. (from [Gwo+13])

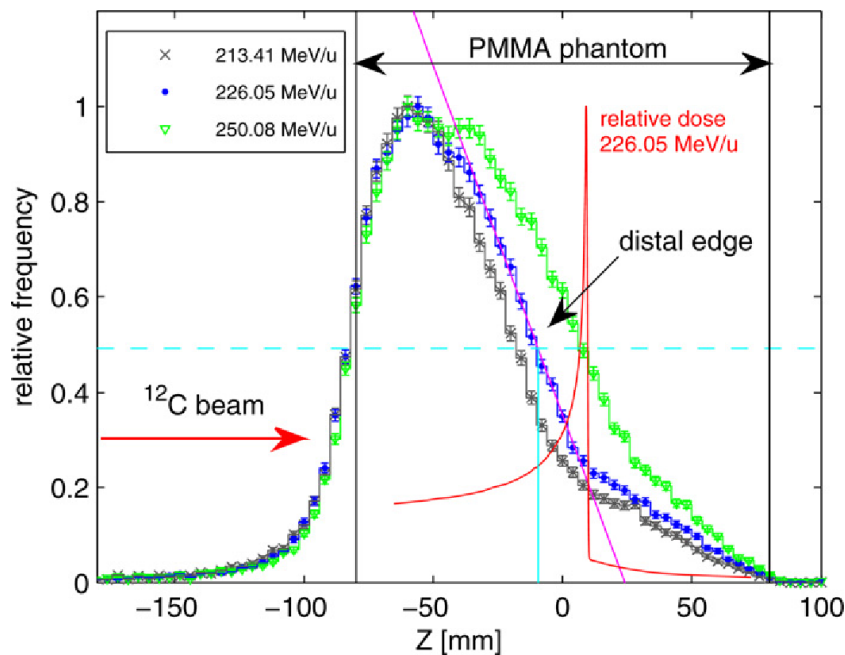


Figure 6.3.: Relative frequency of secondary ions originating the PMMA phantom along the z axis – The PMMA volume is shown by vertical black lines at $z = -80 \text{ mm}$ and $z = 80 \text{ mm}$. A change in the slope (pink line) of the distal edge distribution indicates the position of the Bragg peak (in red). A more stable measure of the Bragg peak position is a drop of the maximum to a value of 50 % at the distal edge (light blue dashed line). (from [Gwo+13])

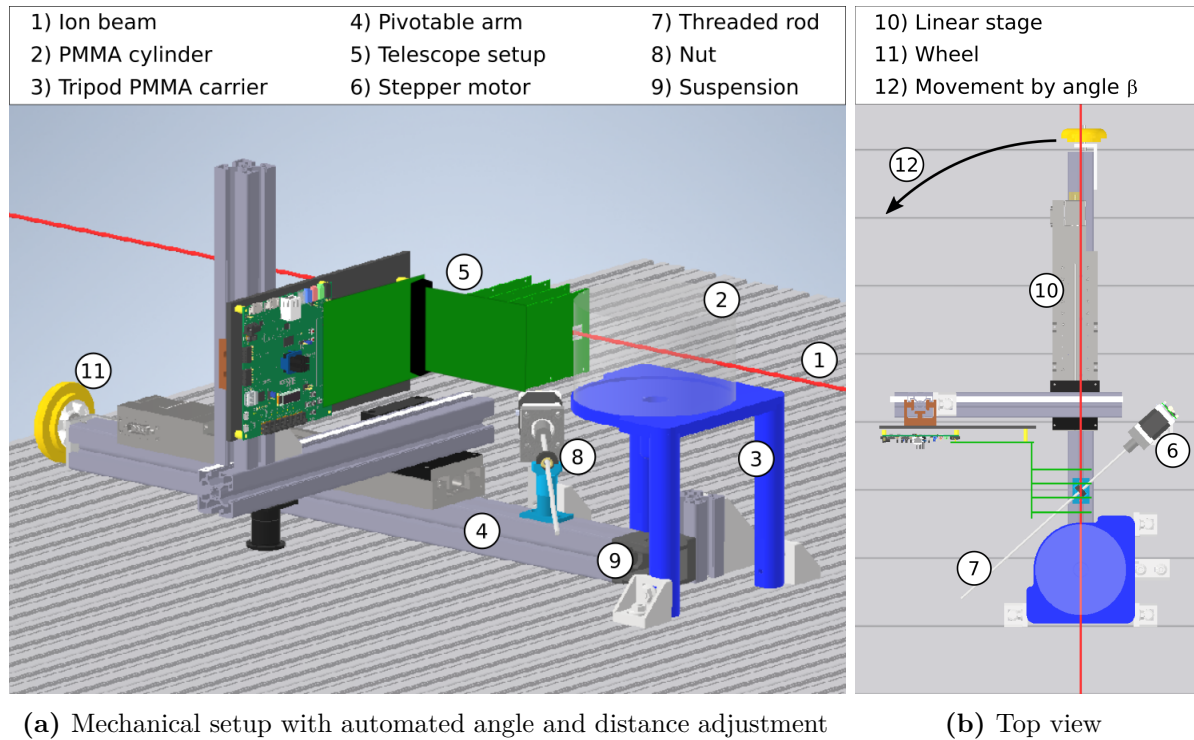


Figure 6.4.: Mechanical setup for secondary particle tracking – The mechanical setup automates the positioning of the telescope setup. The angle towards the beam axis (1), as well as the distance of the first telescope layer to the PMMA cylinder (2) center are adjustable within a certain range. The tripod cylinder carrier (3, blue) is 3D printed and attached to the table. A movable arm (4) carries the telescope setup (5, green). The angle β is adjusted via a stepper motor (6), turning a threaded rod (7). This rod is attached to the movable arm via a nut (8). The rod rotation leads to a movement of the arm around the suspension in the center (9), beneath the PMMA cylinder (in origin of yz plane). The arm is additionally beared on the yellow wheel (11). The distance d is adjustable via a linear stage (10).

Section 6.2.1. The properties of the telescope used for the beam test with four layers of the HV-CMOS sensor ATLASpix3 are described in Section 6.2.2.

GEANT4 simulations were performed to estimate scattering angle distributions and main types of secondary particles. The simulations showed a high amount of uncharged neutrons which are not detectable with the silicon sensors used in the setup. Therefore, a converter for slow neutrons made from polyethylene was included in the design of the measurement setup and data was taken with the converter in place. These studies could not be further pursued and are only briefly summarized in appendix B.1. The topic of neutron conversion during secondary particle tracking is studied in [Jak+11].

6.2.1. Mechanical Setup

An ideal future application realizes full 3D-coverage of the irradiated tissue with secondary particle detectors. As our aim was to test the ATLASpix3 sensor for this purpose, variable angles were a requirement for the mechanics of the system. Due to unknown secondary rates, a variation of the particle rates and therefore, of the distance between the first sensor layer and

the center of the PMMA cylinder was desirable. A suitable cost efficient setup with variable telescope positions was developed and built. The setup is shown in Figure 6.4, the sketch will guide through the following explanations.

The measurements took place at the beam test area of the HIT facility. There, a table with adjustable position and height was available. The table had a size of $100\text{ cm} \times 120\text{ cm}$. The notches of the profile table surface had a distance of 40 mm . The isocenter of the ion beam has a height of approximately 1.29 m and is marked via a laser system. The mechanical setup was developed taking the given geometries at HIT into account.

The PMMA cylinder has a diameter of 160 mm and a height of 90 mm with a total mass of $\sim 2\text{ kg}$. A stable mount of the cylinder at a suitable height in the iso center had to be ensured during the measurements. For this, a tripod carrier was 3D printed (blue in Figure 6.4) with a recess to keep the cylinder in place. A cylindrical hole in the center of the PMMA cylinder allows central alignment of the carrier. Beneath the cutout, a pivoted joint can be attached to profile table and allows a 180° rotation of an arm. At this point, accurate alignment at the symmetry axis of the PMMA cylinder is important for later calculations. A wheel at end of the arm and a metal plate beneath allows smooth movement of the setup without jolting in the profile notches of the table. Two further profiles are attached to the movable arm. The telescope setup (green in Figure 6.4) is screwed onto the vertical profile over a polyvinyl chloride (PVC) plate. The x - and y -positions are manually adjustable.

The minimal distance of the first telescope layer to the center of the PMMA cylinder is 89 mm . A linear stage by Physical Instruments (PI), connecting the rotating arm with the second horizontal aluminium profile, allows adjustment of this distance d . The linear stage is remotely controllable via a software written by R. Schimassek for different projects. The linear stage allows measurements with a maximum distance of $d = 289\text{ mm}$.

Also, the angle β of the telescope setup towards the beam axis is adjustable in a range of $0^\circ - 75^\circ$. A stepper motor is pivoted on the profile table on the right, next to the setup (Figure 6.4b). An M5 threaded rod¹ is connected to the stepper motor and rotated by it. The connection of the rod with the rotating profile arm is realized by a screw nut. The rotation of the rod in the thread of the nut pushes or pulls the arm when the motor moves. The NEMA 17 stepper motor by Trinamic (Figure 6.5) is remotely controlled via a MeasurementControl device, written by U. Elicabuk for a different project [Tri21; Eli21]. A selfwritten software package and GUI translates the angle into a number of steps. For the calculations, the position of the stepper motor, the rotation point of the profile arm, and the distance between the nut, and the rotation point have to be known. Before the measurements at the beam test, a check of the angular positions was performed. Here, an angular uncertainty of $\pm 2.5^\circ$ is assumed. The mechanical setup allows for fast data acquisition at different positions from remote with moderate angular accuracy. A referencing of the angle is done via a limit switch. A second limit switch at $\sim 80^\circ$ increases the safety of the setup.

6.2.2. Properties of four-layer ATLASpox3 Beam Telescope

The centerpiece of the system is the four-layer ATLASpox3 telescope, shown in Figure 6.6. It was designed by R. Schimassek [Sch21b] for the detection of particle tracks. Each sensor layer has a sensitive area of the size $20.2 \times 19\text{ mm}^2$ which is formed by 132×372 pixels with a pitch of $150\text{ }\mu\text{m} \times 50\text{ }\mu\text{m}$ each. With these parameters, a spatial resolution can be estimated for columns and rows, respectively x and y direction:

$$\sigma_x = \frac{150\text{ }\mu\text{m}}{\sqrt{12}} \approx 43.3\text{ }\mu\text{m} \quad \text{and} \quad \sigma_y = \frac{50\text{ }\mu\text{m}}{\sqrt{12}} \approx 14.4\text{ }\mu\text{m} . \quad (6.2)$$

¹M5 thread pitch: 0.8 mm/revolution

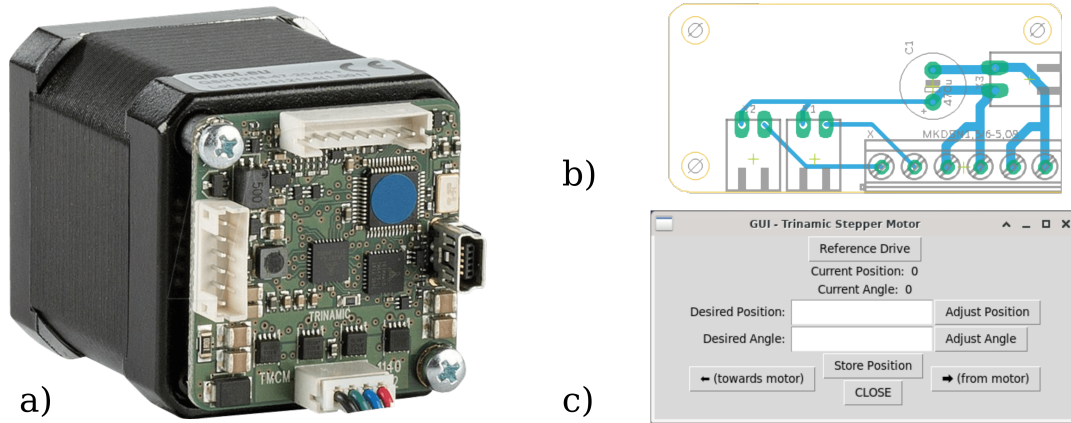


Figure 6.5.: A stepper motor in combination with a threaded rod is used to rotate the telescope setup remote controlled. – a) The NEMA 17 stepper motor by Trinamic. (from [Tri21]) b) The layout of the circuit which was designed to control the stepper motor. The components from left to right are: Two limit switches, a 6-pin connection to the motor driver, a smoothing capacitance and a connection to the power supply. c) The graphical user interface was written to set angle and correlating number of steps for the stepper motor.

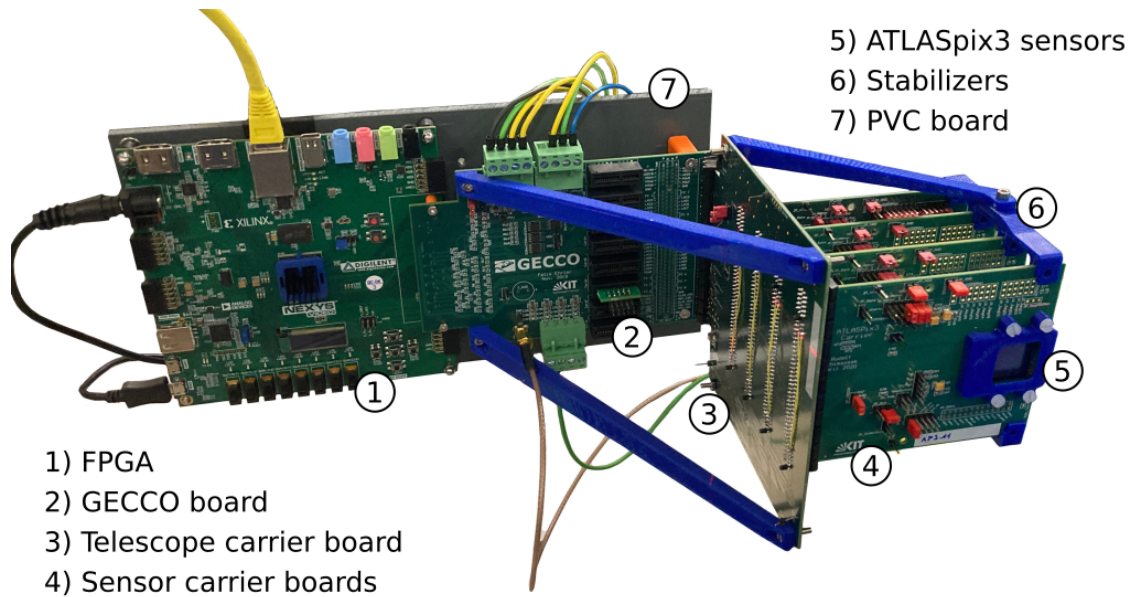


Figure 6.6.: Four-layer ATLASpix3 telescope as used for beam test – The four-layer telescope is connected to power, FPGA (1), and hence the computer via the GECCO board (2). The PCIe connectors of the telescope carrier board (3) hold the four sensor carrier boards (4) with the ATLASpix3 sensors (5) in place. Additional stabilizers (6) prevent movements and keep a distance of 25 mm between the layers. The telescope is mounted on a PVC board (7) during the measurements.

The carrier boards of each layer are connected to a telescope PCB via PCIe connectors. Stabilizers, connecting the GECCO board and the telescope PCB, prevent movements. Additional stabilizers in the outer region of the chip carrier boards and the placement of the PCIe connectors keep a distance between each layer at 25 mm. During the beam test, the telescope was mounted on a PVC board (grey in Figure 6.6) via holes in the FPGA board and the GECCO board.

The sensors are provided with power and configuration data via the GECCO board. The firmware and the data format are both based on the single-chip setup. This enables synchronous readout of all sensor layers. Formerly unused bits in the binary data format now contain the layer information. One time bin of ATLASp3, referred to as time stamp, was set to 50 ns during the measurements.

Rate Limit Estimations

An estimation of data transmission limit was made by R. Schimassek and is briefly summarized here for later comparison. With the firmware used during the beam test, a data transmission rate from chip to FPGA of 200 Mbit/s was used. By design, a transmission rate of up to 1.6 Gbit/s is possible [Pra20]. At high rates, one hit consists of 8×10 bit-blocks leading to a maximum layer hit rate of:

$$\Phi_L = 200 \text{ Mbit/s} \cdot (8 \cdot 10 \text{ bit/Hit})^{-1} = 2.5 \text{ MHit/s} . \quad (6.3)$$

The data multiplexer is responsible for the data transmission from the layer FIFOs to the readout FIFO with a frequency of 100 MHz. For the transmission, the hit data is transferred from 8×10 bit-blocks into three 64-bit words. With a sorting rate of 10^8 words/s and three necessary words per hit, the hit rate of $\Phi_{DM} = 33.3 \text{ MHit/s}$ lies above Φ_L and is therefore no limiting factor for data transmission.

During data transmission via the user datagram protocol (UDP), packages consisting of 127 words are sent from the readout FIFO to the computer via an ethernet physical interface running at a frequency of 125 MHz. One package consists of 1018 byte. Two bytes store the Package ID counting the number of sent packages. Between each package, a pause of 10 cycles is set. Here, the effective data transmission rate can be calculated to $\Phi_{UDP} = 5.148 \text{ MHits/s}$ for all four sensor layers. The bottleneck of this data readout is therefore located in the data transmission via UDP.

More information about the data format of ATLASp3 is provided in [Sch21b].

6.3. Pre-Characterization of the Telescope Sensor Layers

For each of the four layers, threshold tuning and ToT calibration measurements were performed. Table 6.1 summarizes the sensors, the order in the telescope with layer number i , the distance d_i to the center of the PMMA cylinder, the target threshold for the tuning procedure, and the status of the ToT calibration.

For a uniform response of the pixel matrix, a threshold tuning was performed. The results of these scans, as the distribution of threshold values, the TDAC values, and the noise, are provided in Section B.2. The measured TDAC values are stored in configuration files, used later during the beam test measurements. One designated sample (AP3.10) showed problems with the supply of depletion voltage. Therefore, this sensor was replaced with sample AP3.4, characterized before by R. Schimassek [Sch21b]. This is the reason for the different target threshold value. During the measurements, a defect of column 64 of sensor AP3.11 was detected. The tuning procedure therefore was split into two steps, visible in Figures B.5a and B.6a.

Table 6.1.: Sensor layers, used for the measurements – The sensor positions i and labels are noted. Distance d_i is given by the the distance between the layer and the center of the PMMA phantom at the smallest distance. Additionally, the target threshold from the tuning procedures and the status of the ToT calibration are listed. For sensors with (\checkmark), a ToT calibration was performed but not implemented in the analysis. AP3.10 showed damage when applying high voltage and was replaced with sensor AP3.4.

Sensor layer i	Sensor	Distance d_i (in mm)	Threshold (in V)	ToT calibration
1	AP3.11	89	0.365	(\checkmark)
–	AP3.10	–	0.365	–
2	AP3.9	114	0.365	\checkmark
3	AP3.8	139	0.365	\checkmark
4	AP3.4	164	0.224	(\checkmark)

The ToT calibration allows a conversion of the measured ToT values into signal charge. The calibration measurements were performed for each sensor layer. Due to time constraints and technical problems, the calibrations of the sensors AP3.4 and AP3.11 could not be performed in time and were therefore not used in the analysis. The tracking only weakly depends on the absolute generated charge in the sensor pixel as the center of mass of clusters is determined by the generated charge. But as for ATLASpix3 the main share of hits is expected to have cluster size one, this is no problem for the further analysis.

6.4. Measurement Procedure

All presented measurements were carried out in the experimental room of HIT irradiation facility. The wide variety of adjustable beam parameters at HIT has already been addressed in Section 4.2.2. For our measurements, a plan with realistic treatment energies of the carbon ion beam was put together by J. Naumann. All settings of the applied treatment plan are summarized in Table 6.2. This treatment plan allowed an automated energy scan with two spills per energy setting. The first spill has a length of ~ 5 s, the second of ~ 1.5 s. The beam diameter at the isocenter depends on the energy setting. The intensity was constant. The range inside a material depends on the energy of the traversing particle. The penetration depth of the Bragg peak increases with energy by approximately 1 mm per energy setting step (see Table 6.2).

Besides a variation of the energy, an automated setting of the position was permitted by the mechanical setup. From the control room, the measurements were monitored. Interruptions of the measurements were kept down to a minimum by a remote adjustment of angle β and distance d . The scaled sketch in Figure 6.7 visualizes positions of the first telescope layer during the measurements. At each position, the energy scan with two spills per energy setting was performed, leading to eight different energies per position.

Table 6.2.: Beam parameters of carbon ion beam – A range of realistic ascending treatment energies was combined to a treatment plan to enable fast data acquisition. Focus and range in the PMMA material depend on the energy. The intensity was chosen to be constant throughout the measurements.

Energy setting E	Energy (in MeV/u)	Focus (in mm)	Intensity (ions/s)	Range (in mm)
40	161.55	6.1	$3 \cdot 10^6$	60
50	176.56	5.7	$3 \cdot 10^6$	70
60	190.75	5.3	$3 \cdot 10^6$	80
70	204.27	5.0	$3 \cdot 10^6$	90
80	217.25	4.8	$3 \cdot 10^6$	100
90	229.76	4.6	$3 \cdot 10^6$	110
100	241.84	4.4	$3 \cdot 10^6$	120
110	254.71	4.3	$3 \cdot 10^6$	130

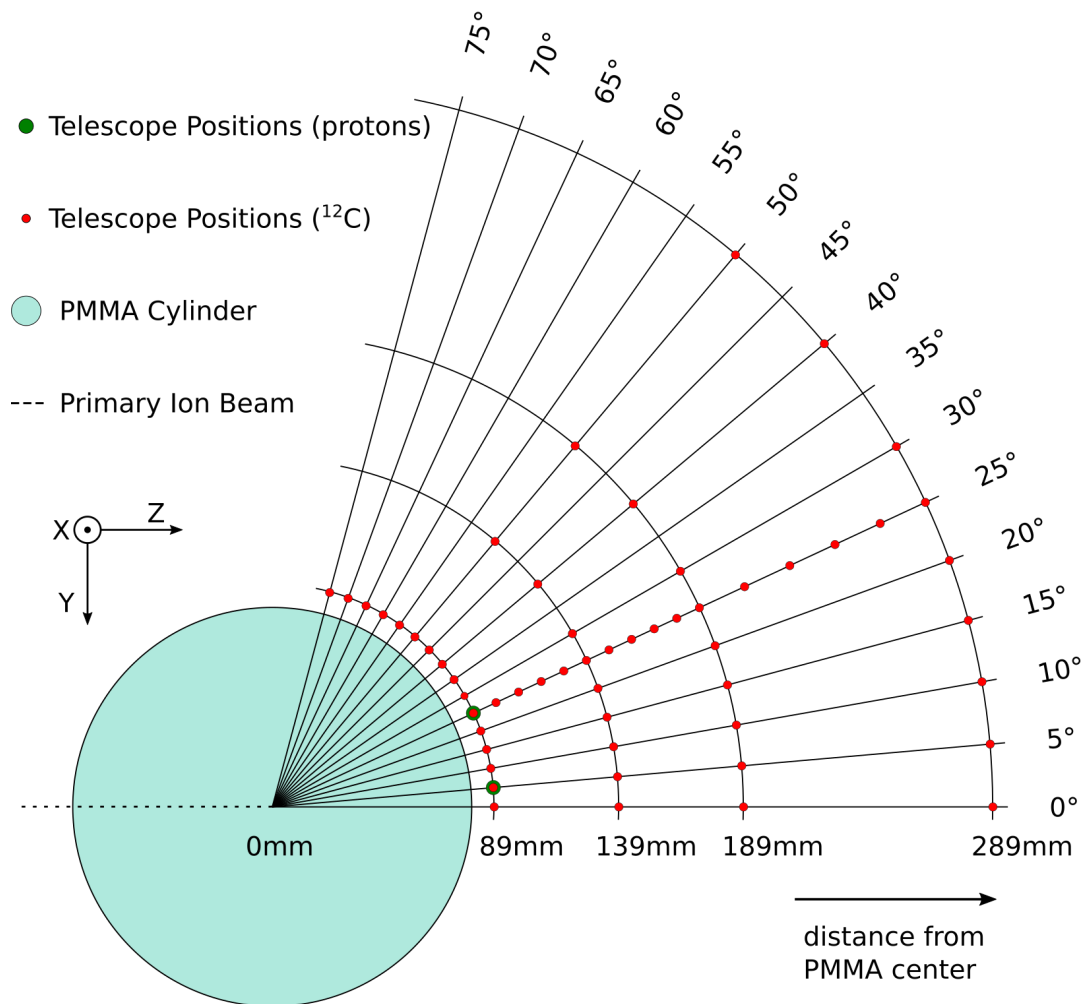


Figure 6.7.: Sketch of telescope positions during beam test – The scaled top view schematic of the setup shows positions of the measurements. At every position, the secondary ions of eight different carbon ion beam energies were recorded. For the calculations, a cartesian coordinate system with the origin in the center of the cylinder is used.

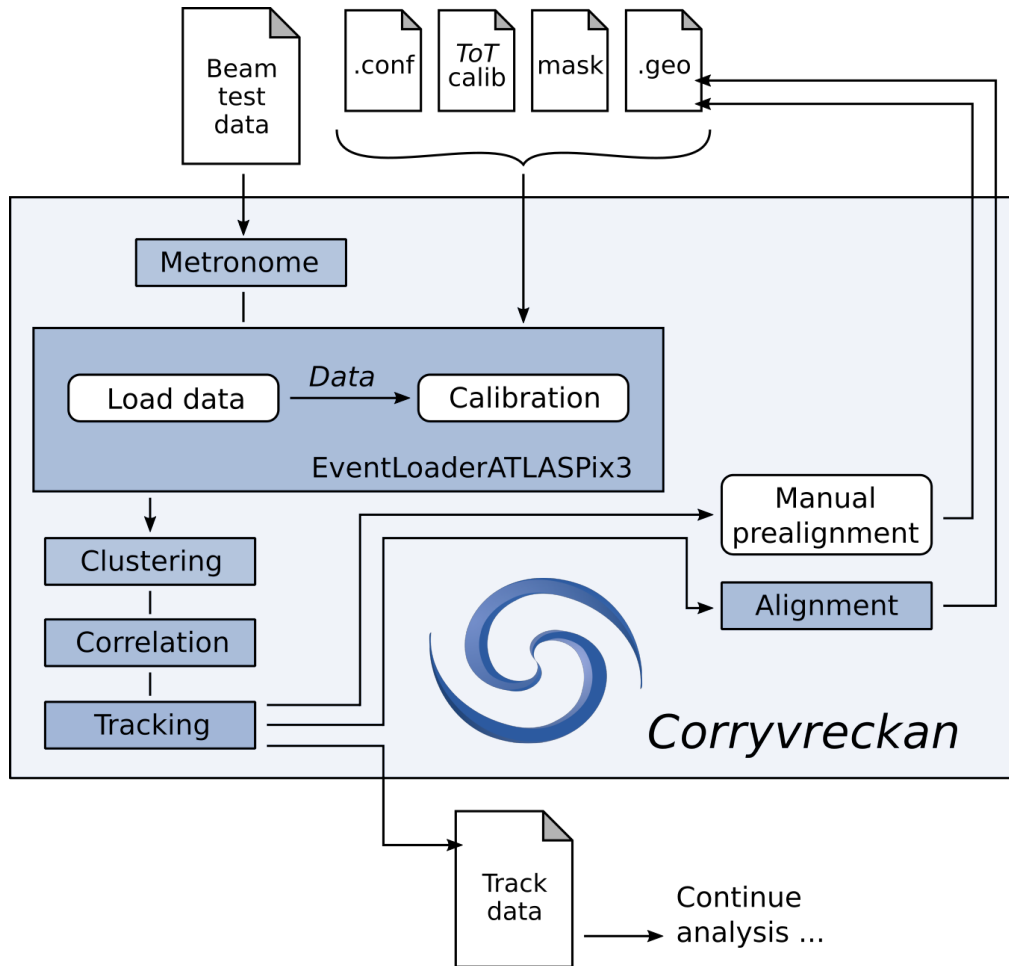


Figure 6.8.: Modules and processing steps of the *Corryvreckan* framework – The flowchart visualizes the data analysis of the beam test data using the *Corryvreckan* framework. The beam test data is loaded in batches by the self-written module [EventLoaderATLASPix3]. The batch length is defined by the metronome. A file with the parameters of the ToT calibration is used for the conversion of the pixel signal data to charge. Masked pixels, defined in the masking file, are ignored in the analysis. The configuration and geometry files provide important information for the following analysis steps, as clustering, correlation, and tracking. The information obtained by the alignment procedure with track residuals is stored in the geometry file and used for further analysis steps.

6.5. Corryvreckan Framework

For the analysis of the beam test data, the flexible, fast, and lightweight data reconstruction framework *Corryvreckan* was used [Dan+21]. The following section summarizes the analysis steps and the functions of the individual framework modules, as the framework analysis is based on a set of modules given in the configuration file (`.conf`). The execution of the modules is performed in the order of appearance. All modules used during the analysis and their order of execution are summarized in the flowchart of Figure 6.8. An exemplary configuration file, as used during the analysis, is provided in File B.1. Further and more detailed information on the core modules is provided in the manual [WSK21].

[EventLoaderATLASPix3]

The module [EventLoaderATLASPix3] was written by the author of this thesis and R. Schimassek. Either binary or decoded data from an input file is read and processed with the data from a masking file (example in File B.2) and the results of the ToT calibration (example in File B.3). Masking was necessary, for example for the defective column 64 of sensor AP3.11. Spatial information about the detector layers and the spatial offsets are given in the geometry file (`.geo`). Data reading is done in batches based on the time intervals of given events. The module [Metronome] provides information on the event definition. For the given rates, an event length of $5 \mu\text{s}$ was chosen. In a sequential loop, data of each event is further analysed with the other modules of *Corryvreckan*. The analysis of each module is configured via arguments in the configuration file.

[Clustering4D]

A clustering algorithm is provided by the module [Clustering4D]. The clustering is performed based on the hit timestamps and spatial proximity. Spatial and timing cuts are set in the configuration file. A `Cluster` is an object of the framework and defined as a collection of hits (stored as an object `Pixel`) with an additional center position. By default, the cluster center is determined as the charge-weighted mean. Several output histograms, as cluster size, seed charge, time differences of cluster pixels, and more, are provided by the framework.

[Correlations]

The correlations between the layers are evaluated by the module [Correlations]. Again, spatial and timing cuts can be set in the configuration file. As secondary particle tracks are not parallel, no sharp angle bisecting correlation is expected.

[Tracking4D]

The module [Tracking4D] tracks the data with a straight line algorithm. Effects of multiple scattering are neglected in the following, as the HV-CMOS sensors are thin. Further studies should consider this effect. The framework object `Track` stores a collection of `Clusters`, the parameters of the straight line, and the χ^2 value as a measure of fit quality. The χ^2 values are thereby determined as [Cor21]:

$$\chi^2 = \sum_{p=0}^N \left(\frac{r_{p_x}^2}{\sigma_{p_x}^2} + \frac{r_{p_y}^2}{\sigma_{p_y}^2} \right). \quad (6.4)$$

Here, index p counts the number of N hit layers. r_{p_x} and r_{p_y} are the track residuals, defined as the difference of the found hit position and the fitted track position. The estimated uncertainties

σ_{p_x} and σ_{p_y} depend on the direction, as the pixels are of rectangular shape. By a modification of the default module, the found tracks are stored in files, separated by measurement settings, for further processing.

[AlignmentTrackChi2]

Shifts of the sensor positions against each other have great influence on the quality of the tracking results. *Corryvreckan* therefore provides several alignment modules to determine the spatial displacements and rotations to feed them into further calculations. Iterative shifts and rotations are performed to align the individual sensor layers to a reference layer. Here, the first sensor layer is chosen as **reference** with a number of iterations set to 4 per alignment step.

It is important to understand that the correlations depend on the physical displacement of the sensor layers and the direction of the incoming particles. Therefore, the correlations can not be forced to be centered around zero. Instead, the manual prealignment, performed in these studies, is based on the residual displacement of the tracks.

The actual alignment module [AlignmentTrackChi2] performs an optimization of the track χ^2 . The rotational and translational offsets of the sensor layers are determined this way. Few iterations are required for good results. All coordinates are specified in a right-handed cartesian coordinate system with origin located in the center of the PMMA cylinder.

6.6. Preparation of Beam Test Data

This section describes the preparation steps for the beam test data analysis. The separation of the zero-suppressed data format for the individual parameter settings is described in Section 6.6.1. The separated data files are then analysed with clustering and correlation modules of the *Corryvreckan* framework (Section 6.6.2 and 6.6.3). The alignment of the telescope and the results are described in Section 6.6.4.

6.6.1. Spill Structure and Separation of Data Files

The data acquisition during the beam test took place for the whole energy scan. Each data file contained two spills for each of the eight energy settings. For analyses, the data files therefore first had to be separated into files for the individual parameter values. Figure 6.9a shows the evolution of the number of recorded hits over time during an energy scan. The increasing energy after two spills is visible in the increasing hit rate. Since some hit timestamps were faulty, a sorting of the data, based on this parameter, was difficult to realize without complex filtering. The 16-bit package ID (Figure 6.9b), stored in the binary format of each hit, was a simpler to implement parameter for a separation algorithm. During the readout process, packages containing 127 words are transmitted, each hit consisting of three words. After a maximum of 43 completed hits, the package is full and the following hits are transmitted in a new package with new package ID. After 134 ms without data being added, non-empty packages are sent without filling them up completely. Therefore, a dip in the distribution indicates a pause of the beam. The separation algorithm took into account possible multiple overflows of the 16-bit package ID counter, for large amounts of data at high rates.

6.6.2. Clustering

The clustering of the data from the individual layers and determination of the cluster centers are necessary to optimize the quality of the tracks. Figure 6.10 shows the clustering results of layer 2 (AP3.9), as the ToT calibration was implemented for this sensor plane and a calculation

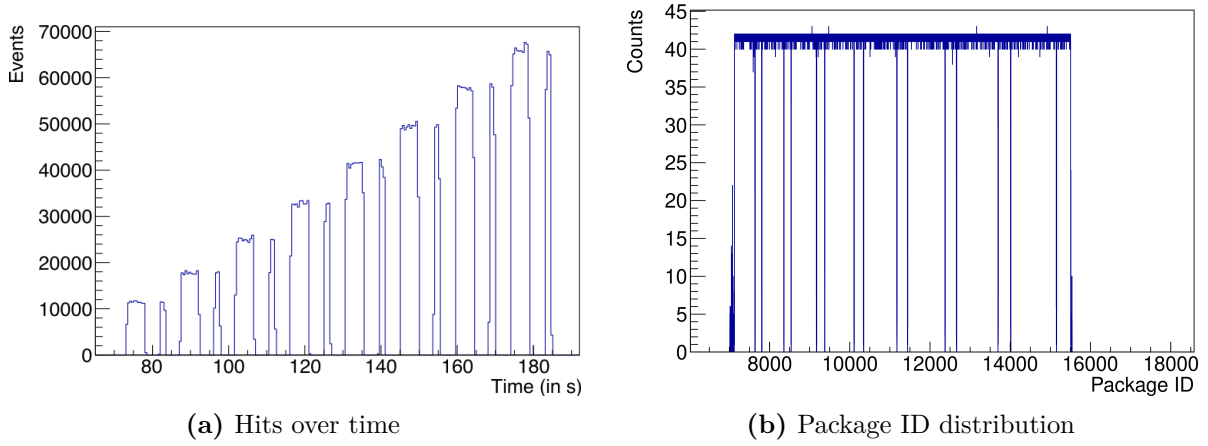


Figure 6.9.: Different visualization methods of the spill structure – Spill structure at parameter settings: $E = 40$, $\beta = 20^\circ$, and $d = 89$ mm. – (a) The increase of the energy is visible in the increasing hit rate. For each energy, two beam spills of different lengths were applied. (b) The separation of spills is based on the Package ID. Each hit is assigned the ID from the package it was sent in via the UDP data transmission. Dips in the distribution of this quantity indicate very low beam intensity – hence a time span without beam.

of the charge deposit was possible. The cluster size distribution in Figure 6.10a shows a dominant share of single pixel events. Nevertheless, the clusters of the charged secondaries cannot be neglected as for e.g. X-ray photons as in Chapter 5 for which a punctiform energy deposit is expected. The cluster charge is calculated with the parameters of the ToT calibration and the conversion factor from Equation 5.6. The distribution is fitted with a Landau-Gaussian function, expected for charged particles traversing thin silicon layers. The Gaussian share is explained with uncertainties due to pixel electronics. Larger pixel counts in the cluster show an increasing MPV value, as larger signals are more likely to generate signal in more pixels. The MPV values of the distributions with cluster size one, two, and three pixels are given in Table 6.3.

6.6.3. Correlations

Correlations are complex to interpret because they are influenced by many factors. Especially the alignment of the sensor positions to each other and the direction of the incident particles contribute. Still, correlations provide important information about quality of the data.

Figure 6.11 shows correlation plots between different telescope layers, with layer 1 as reference layer. The correlation distribution in x direction (columns) between the first two layers, visualized in Figure 6.11a, has a larger shift to negative values than the distribution of y correlation (rows), shown in Figure 6.11b. This allows the assumption that the angles of incidence are larger in x direction, which could be explained by a downward shift of the setup from the correct x position of the isocenter.

The y correlations for more distant layers (Figure 6.11c and 6.11d) show a broader distribution. This may result from multiple scattering effects and a smearing out of the particle trajectories. Also, the large distance between the sensor layers may be a problem, as particles arriving at large angles may leave the sensitive phase space of the telescope after few layers. Additionally, a larger shift from the center is visible in the distributions, probably resulting from an angle of incidence not equal to zero. This leads to an increasing difference in position for further distances.

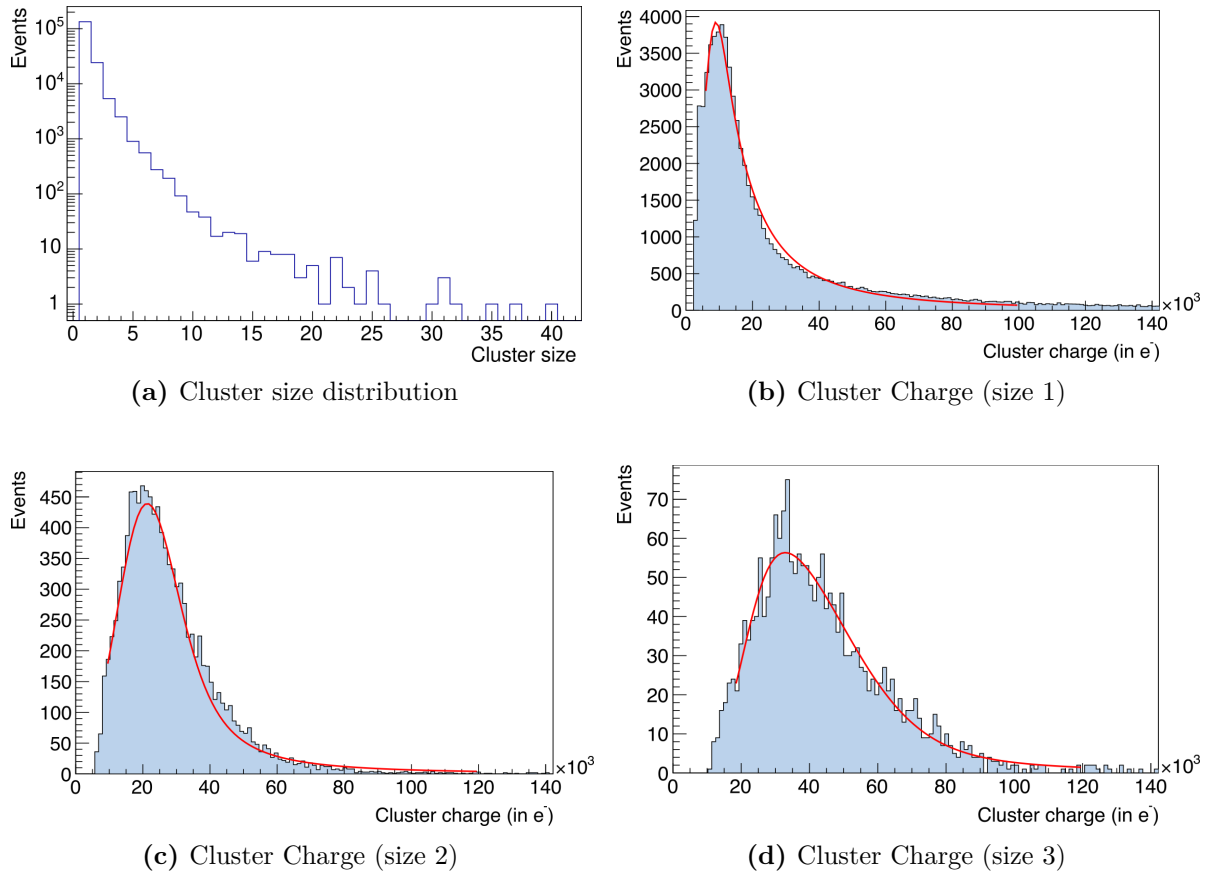


Figure 6.10.: Analysis of hit clusters in the second telescope layer (**AP3.9**) – Settings $E = 110$, $\beta = 25^\circ$, and $d = 89$ mm. The cluster charge in electrons is calculated with the hit’s ToT and the results of each pixel’s ToT calibration parameters. (a) A cluster size up to 40 is visible in the data. (b-d) The cluster charge distributions approximately follow a Landau-Gaussian distribution (red fit curves). An increase in the MPV is visible for larger cluster sizes.

Table 6.3.: MPV of charge deposition for different cluster sizes – The most probable value (MPV) of charge deposition depends on the size of clusters.

Cluster size	MPV (in ke^-)
1	9.0
2	21.3
3	32.9

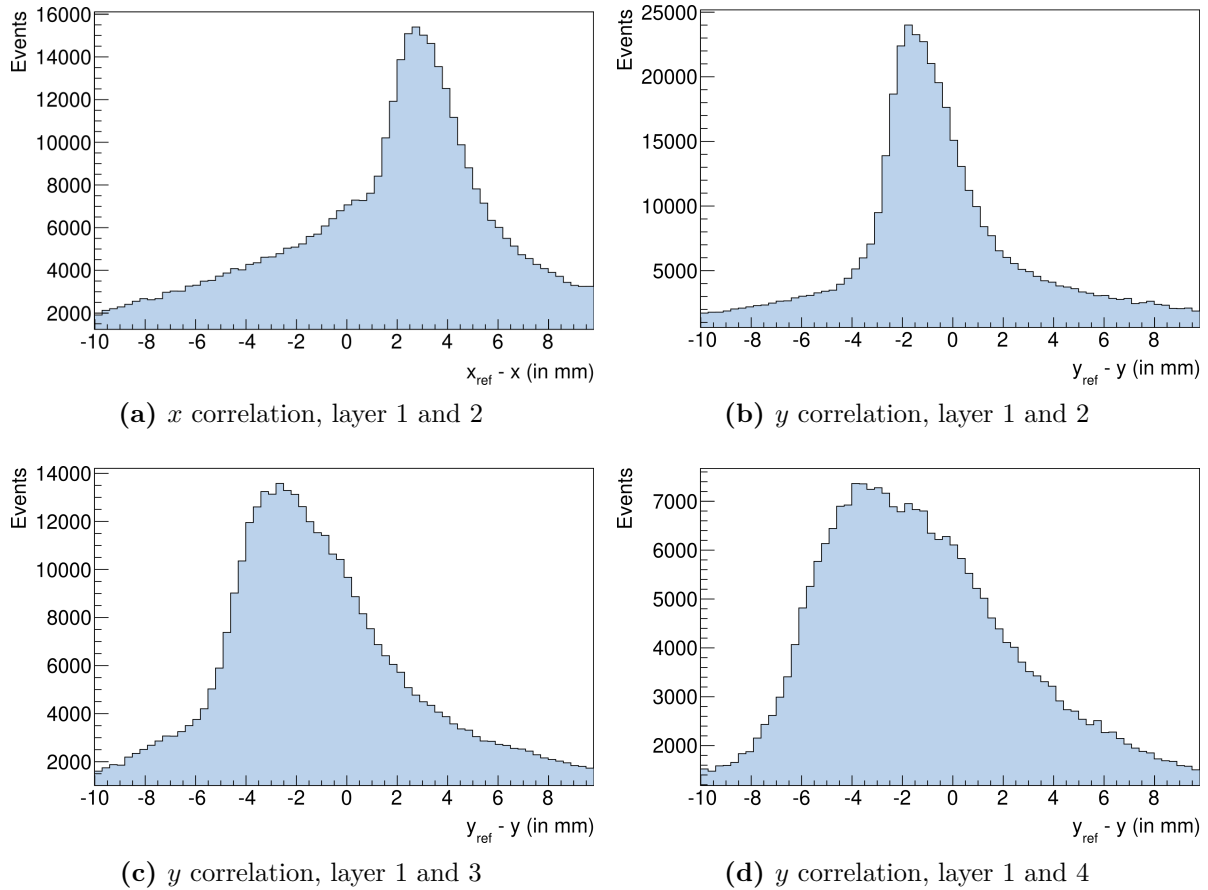


Figure 6.11.: Layer correlations of beam test data – Layer correlations with settings $E = 110$, $\beta = 10^\circ$, and $d = 89$ mm – (a) The x correlation distribution of layer one and two shows a large offset from zero, probably due to non-parallel particles traversing. (b-d) The y correlation distributions are shown for different sensor layers. A widening of the distributions and increasing offsets are visible for more distant layers.

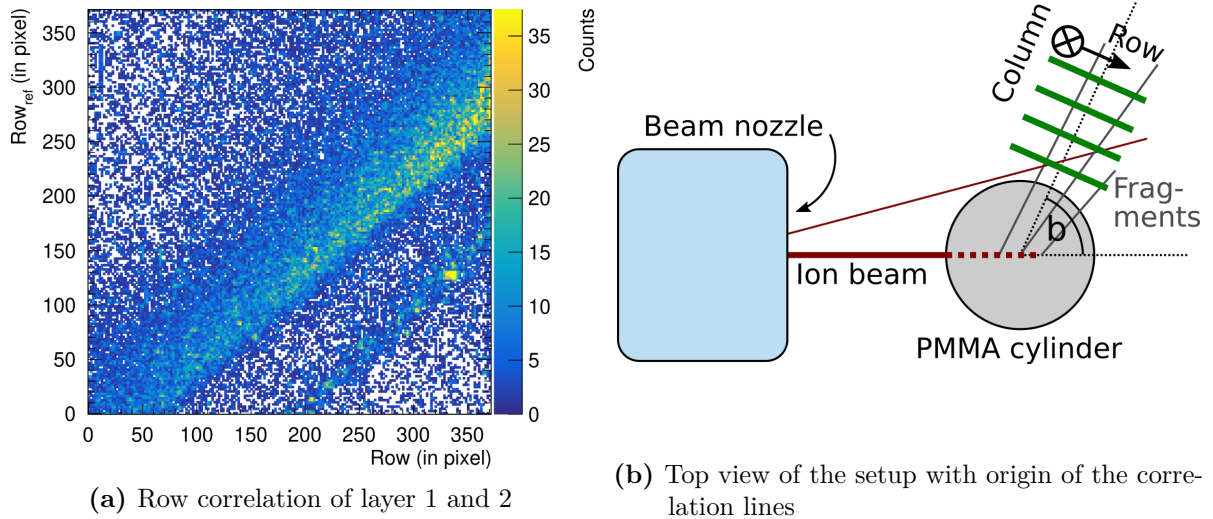


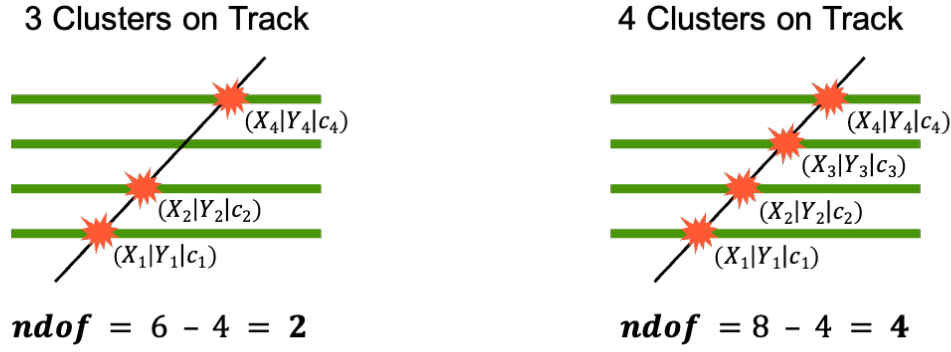
Figure 6.12.: Layer correlations of beam test data – (a) Row correlation of layer 1 and 2 with settings: $E = 110$, $\beta = 25^\circ$, and $d = 89$ mm – The second diagonal, visible below the main row correlation line, can be explained by particles, originating from the beam nozzle. This diagonal is only visible under certain angles β . (b) The sketch visualizes the origin of the particles responsible for the second diagonal in the correlation plot and is not to scale.

The row correlation plot in Figure 6.12a shows an additional correlation line for low row numbers in layer 1 and high row numbers in layer 2. This additional diagonal matches particles directly from the beam nozzle. A sketch (Figure 6.12b) illustrates the scattered particles traversing the first two sensor layers at certain angles β . This hints to tails in the angle distribution of the particle beam that are small but not always negligible.

6.6.4. Sensor Alignment

As the [Prealignment] module could not provide the expected results because of non-vertical particle incident, a manual prealignment was performed. Therefore, the positions of residuals in x - and y -directions were determined, and the investigated offsets of the peaks from zero were set as translational offset in the .geo file. After a few iterations the actual alignment is performed with the determined offsets. Rotations are not included in the prealignment.

For the alignment, data recorded at the settings $E = 110$, $\beta = 0^\circ$, and $d = 89$ mm was used, as here the rates are the highest and the tracks of particles traversing the sensors most parallel. During the iterative alignment procedure [AlignmentTrackChi2], the χ^2 values of the tracks are optimized. Thereby, each track has to consist of clusters in at least three sensor layers. The expected shape of the χ^2 distribution differs for the number of degrees of freedom (ndof) k . This in turn depends on the number of clusters assigned to the track (Figure 6.13). The parameterization of a track needs four parameters (x and y value of two coordinates), as the z coordinates are fixed by the sensor layer positions ($z_i = c_i = \text{const}$). Therefore, a track consisting of three clusters has $k = 2$, whereas $k = 4$ for tracks based on four clusters.



(a) Track with hits in three layers

(b) Track with hits in four layers

Figure 6.13.: Number of degrees of freedom (ndof) for different tracks – The ndof depend on the number of assigned hits per track. c_i are constant values, defined by the sensor layer.

To verify the alignment results, the distributions of χ^2 were observed for tracks from three clusters (Figure 6.14a) and tracks from four clusters (Figure 6.14b). The drops in the histograms are due to spatial cuts in the tracking procedure of *Corryvreckan*.

A fit was applied to the distributions with a and b as rescaling parameters. The distributions show the expected shapes of the χ^2 distributions with k degrees of freedom:

$$f(\chi^2; k) = \frac{a}{2^{k/2} \cdot \Gamma(k/2)} \cdot (b \cdot \chi^2)^{k/2-1} \cdot \exp\left(\frac{-b \cdot \chi^2}{2}\right). \quad (6.5)$$

Here, Γ is the gamma function. a is a scaling constant, depending on the number of entries in the histogram, and b a factor to compress the χ^2 values. The fit parameters of both distributions are given in Table 6.4. $1/\sqrt{b}$ can be considered an estimation of a correction factor on the chosen uncertainty σ . For the alignment and further analysis, σ was chosen as declared in Equation (6.2). With values slightly above one, the fit parameters b both suggest a slight underestimation of the uncertainties.

The geometry file after the alignment procedure is printed in File B.4.

6.7. Analysis of Beam Test Data

The measurements were performed to test the suitability of ATLASpix3 and the telescope in detecting secondary particle tracks. In the following, the track quality is considered in terms of the track residuals and their direction, in Section 6.7.1. In Section 6.7.2, first attempts of the reconstruction of the particle origin and the dispersion of the origin with varying energies are described. The capability of the telescope is discussed regarding the detection rates of the telescope and the secondary particle rates in Section 6.7.3.

6.7.1. Secondary Particle Tracking

With the translational and rotation offsets from the alignment procedure, the tracking procedure was repeated for several data sets. Exemplary, the residuals at parameters of $E = 110$, $\beta = 25^\circ$, and $d = 89$ mm are visualized in Figure 6.15. The track residuals after alignment show narrow distributions with:

$$\sigma_{x, \text{res}} = 29.61 \mu\text{m}, \quad \sigma_{y, \text{res}} = 12.92 \mu\text{m}, \quad (6.6)$$

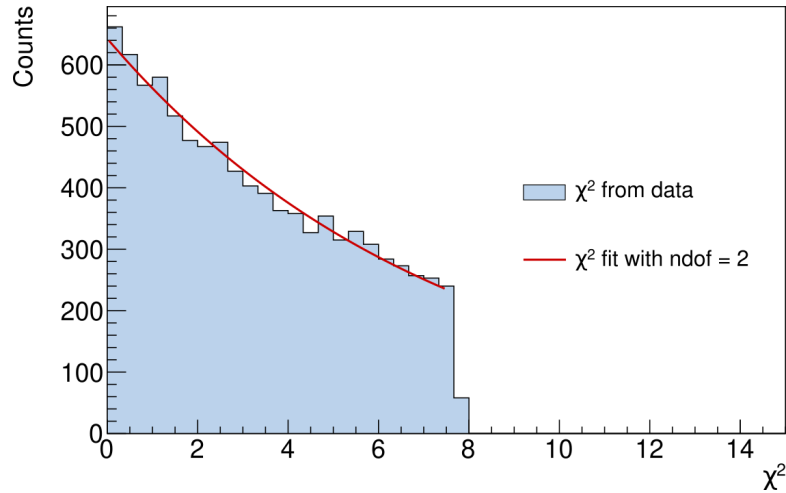
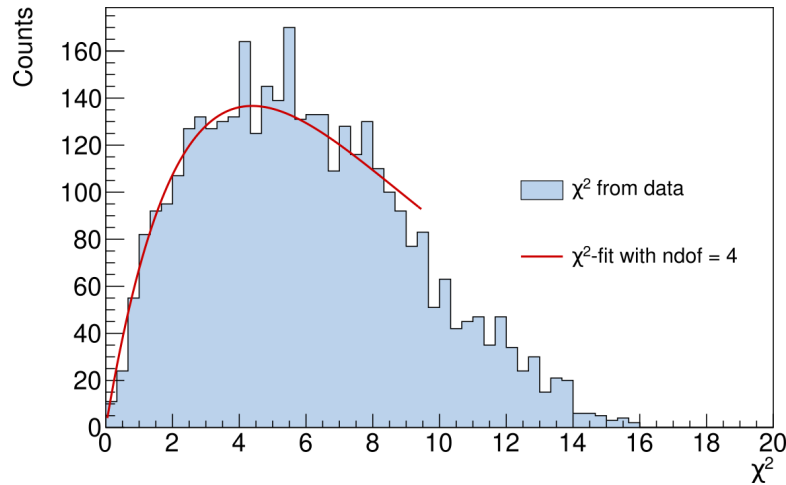
(a) χ^2 value distribution for tracks containing three clusters(b) χ^2 value distribution for tracks containing four clusters

Figure 6.14.: χ^2 distributions of tracks after alignment – Depending on the number of degrees of freedom, the shape of the χ^2 distribution varies. A drop in the distribution is explained by spatial cuts in the tracking procedure.

Table 6.4.: Fit parameters of the χ^2 distribution – In principle, the χ^2 distribution only depends on the number of degrees of freedom. a is required as a scaling constant of the non-normalized histogram. $1/\sqrt{b}$ can be considered as an estimated correction factor on the uncertainty σ , used for the calculations of χ^2 .

ndof k	a	b	$1/\sqrt{b}$
2	1291.08	0.27	1.91
4	743.04	0.46	1.48

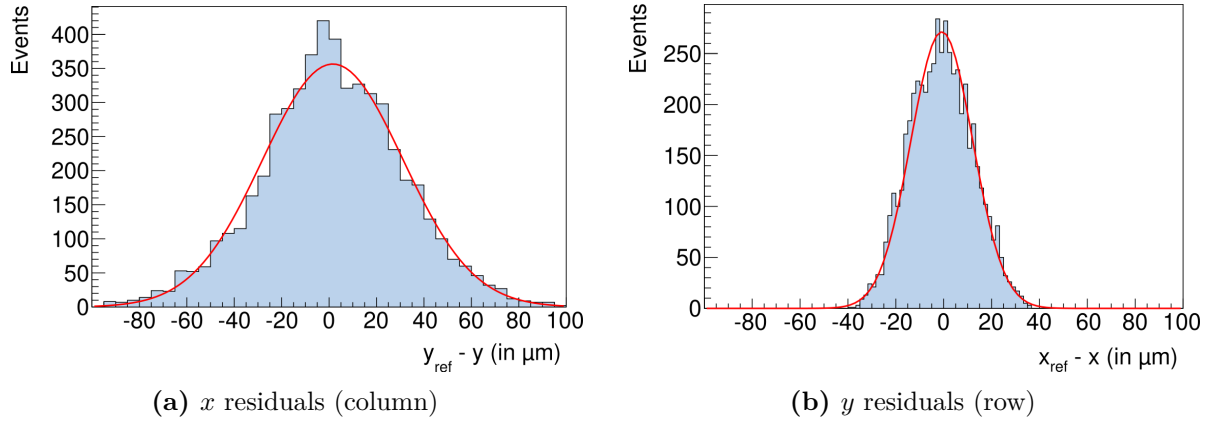


Figure 6.15.: Residual distributions of tracks – Residuals of secondary tracks with settings $E = 110$, $\beta = 25^\circ$, and $d = 89$ mm: The Gaussian fits applied on the residual distributions in x and y direction show deviations below the expected value of $p/\sqrt{12}$.

and are below the estimated spatial resolutions for single hits due to the tracking. With $\mu_x = 1.6 \times 10^{-3} \mu\text{m}$ and $\mu_y = -0.8 \times 10^{-3} \mu\text{m}$, the distributions of the residuals are well aligned around zero.

For a visualization of the tracks, a 3D plot was created, shown in Figure 6.16a. A constriction is visible at the position of the sensor planes. Still, the projection plots on the different layers in Figure 6.16 motivate a low track rate in the outer regions, and a focus of the tracks in the expected beam region. The origin of tracks is expected inside the PMMA cylinder, which is confirmed by the projections. Here, the PMMA cylinder is depicted at its position around the origin of the cartesian coordinate system. Figure 6.16c shows an incline of the tracks along the z axis. This can be explained by a slightly negative offset of the whole setup towards the isocenter position in x direction, already noticeable in the correlation plots in Section 6.6.3.

6.7.2. Reconstruction of Penetration Depth and Track Origin

As the development of a sophisticated reconstruction method was beyond the scope of this thesis, simple approaches have been performed to visualize the dispersion of the energy deposit with varying energies.

In a first attempt, a superposition of the track data was observed with a peak finder algorithm, as this method does not require any assumptions about the beam position. Figure 6.17a illustrates this attempt: as the telescope was rotated around the origin of the cartesian coordinate system in the center of the PMMA cylinder during the measurements, a rotation of the recorded track data around this origin was performed. Figure 6.17b shows the superposition of all track data at $E = 110$ and $d = 89$ mm at the 16 different angles. The maximum of the distribution should be located at the same coordinates for every data set and therefore, be intensified by a superposition. A movement of the Bragg peak is correlated with changes in the beam energy, shown in Table 6.2. Therefore, the superposition of track data was repeated for several energy values. The assumption that the peak of the superposition would move steadily with increasing energies turned out to be wrong. In a further test, the number of tracks for each angle were scaled. The ratio of the number of tracks at the highest energy setting and the number of tracks at the analysed energy was used as a weight to increase the contribution of the larger angles with lower data rates. This approach is illustrated in Figure 6.18 with

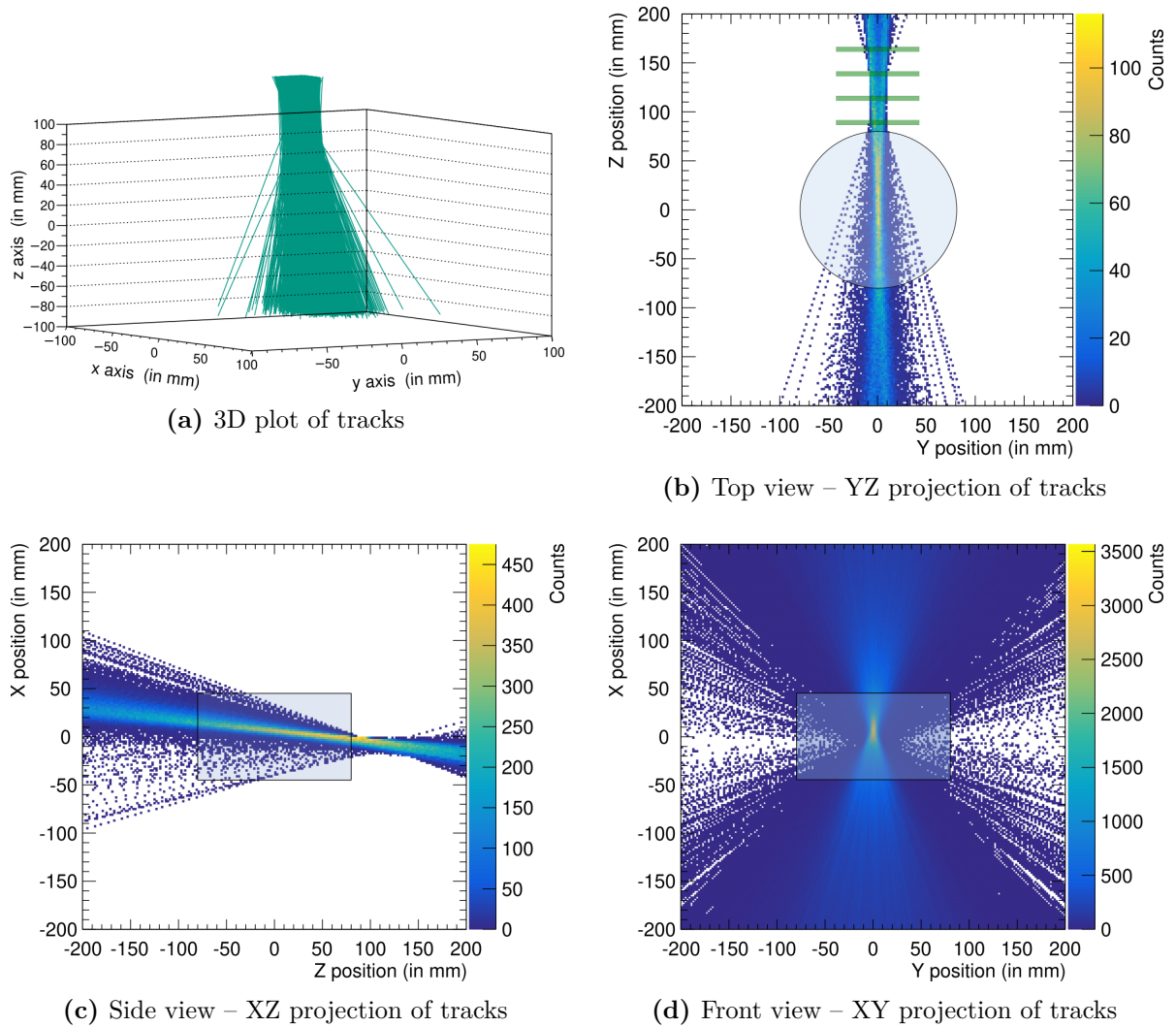


Figure 6.16.: Visualization of secondary tracks – Visualization of track data at $E = 110$, $\beta = 0^\circ$, and $d = 89$ mm – (a) A 3D plot shows the recorded track data. A constriction of the tracks indicates the position of the sensor planes. (b-d) To visualize the origin of the tracks, a projection onto the different coordinate planes was performed. A cross section of the cylinder is indicated in each plot. All tracks seem to have their origin inside the cylinder. Plot (b) shows the position of the sensor carrier boards, explaining the constriction of the tracks at this position. The position but not the size of the carrier boards is to scale for $d = 89$ mm.

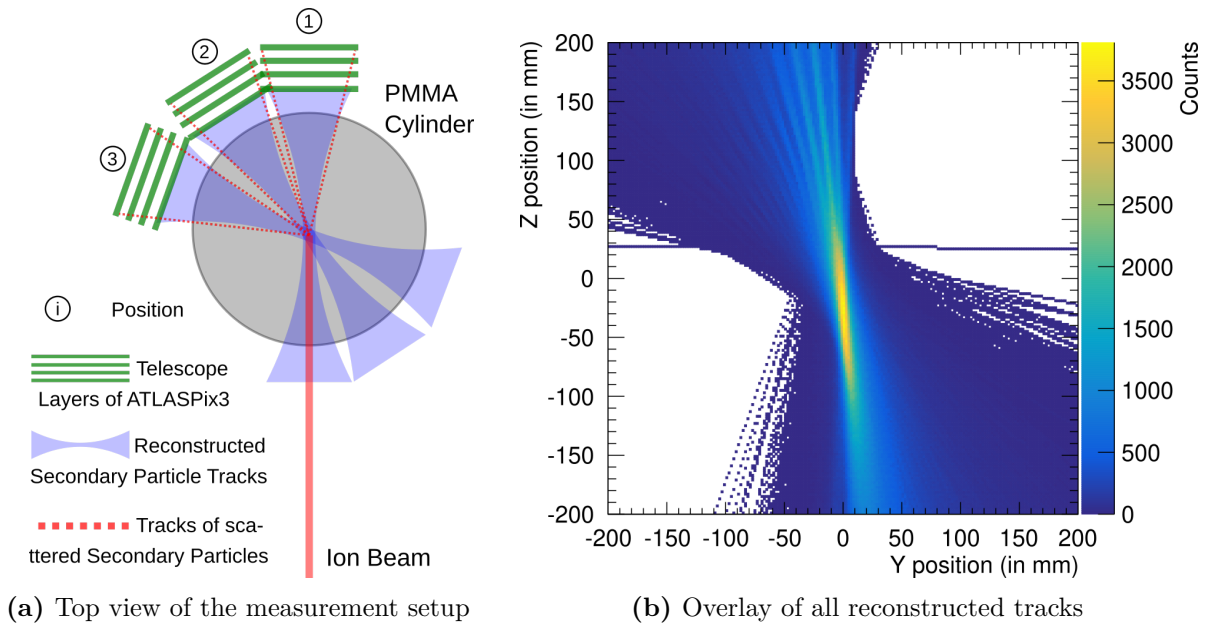


Figure 6.17.: Superposition of rotated track data – (a) A rotation of the telescope setup around the center of the cartesian coordinate system allows a later rotation of the recorded track data. (b) In a first attempt, a movement of the maximum of the superposition for different energy steps was searched. The plot shows the rotated track data of all angle positions with $E = 110$ and $d = 89$ mm. The higher the beam energy E , the further the maximum was expected to be shifted towards positive z positions.

a contour plot to find the maximum. Again, no movement of the maximum of the expected magnitude was detectable.

A further attempt was based on the backprojection method, used in [Sch21c]. Here, the position of the pencil shaped beam was assumed as a straight line through the origin and parallel to the z axis. The track position of least distance towards this straight line was assumed as the point of interaction, hence the track origin. Figure 6.19 shows the distributions of the determined origins for the two extreme energy settings $E = 40$ and $E = 110$ at the angle $\beta = 25^\circ$ and least distance $d = 89$ mm. The distributions show a significant difference in the shape of the distal edge. This approach and further analyses based on the assumptions of Section 6.1 could not be pursued any further in the scope of this thesis.

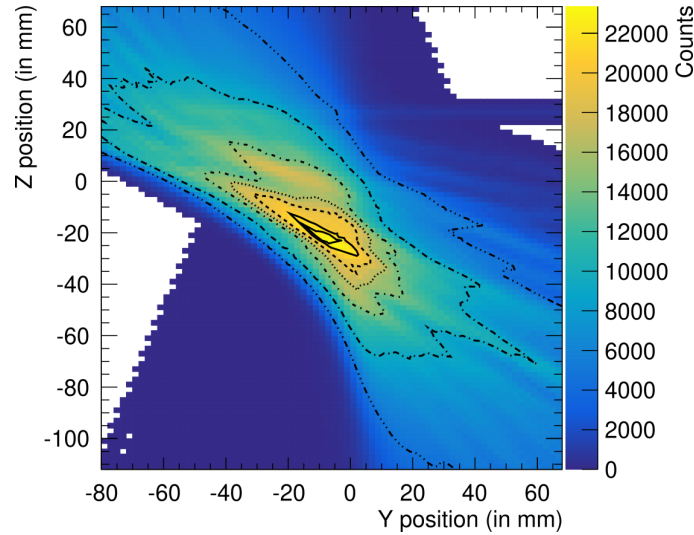


Figure 6.18.: Superposition of rotated and scaled track data with contour plot – The visualized tracks were measured at different angles with $E = 110$ and $d = 89$ mm. In a second attempt, the tracks for the different angles were weighted to level the contribution of all angles. This was done to increase the contribution of larger angles. A contour plot visualizes the maximum of the distribution.

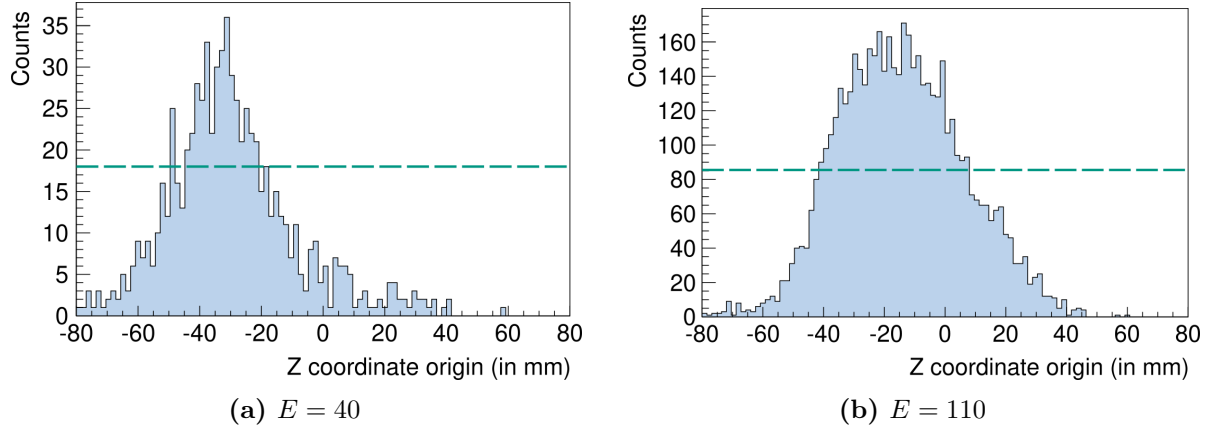


Figure 6.19.: Distribution of z coordinate of track origin – The track origin is determined via backprojection: The ion beam is assumed as a straight line running on the z axis. The track position with the smallest distance to the beam is considered as the track origin. The data of the plots was recorded with settings: $\beta = 25^\circ$, and $d = 89$ mm – The green line is drawn at half maximum of the distribution, orientating to the method described in [Gwo+13]. A shift of the distal edge in the distributions is visible between Figure (a) with $E = 40$, and Figure (b) with $E = 110$. The rate in the left plot is much lower due to the lower initial beam energy.

6.7.3. Particle Rates

An estimation of particle rates must be made to evaluate the suitability of ATLASpix3 and the associated readout system for the telescope setup. The limit of the telescope's data processing was determined as $\Phi_{\text{UDP}} = 5.148 \text{ MHits/s}$ for all layers combined. A maximum hit rate for the individual layers was calculated to be $\Phi_{\text{L}} = 2.5 \text{ MHits/s}$. With different settings, an extension by a factor of at least six (tested) or eight (from design) can be achieved [Sch21a; KIT19].

The settings with the highest expected particle flux are: $E = 110$, $\beta = 0^\circ$, and $d = 89 \text{ mm}$. Figure 6.20a shows the rate distribution of two separated beam spills with these parameters in the first telescope layer. No clustering has been performed, as the total hit rate has to be considered. A hit rate of $\Phi_1 \approx 2.5 \times 10^5 \text{ Hits/s}$ is visible. The rates for the other telescope layers are smaller than Φ_1 . Therefore, the highest achieved hit rate lies one order of magnitude below the maximum readout rate.

Figures 6.20b to 6.20d provide information about the dependency of the hit rate on the individual parameters: Figure 6.20b shows a decrease in rate for rising angles β . This fits the expectations for multiple scattering in matter, described in Section 2.2.4. A reasonable Gaussian fit for small angles fails due to small amount of data and an outlier at $\beta = 15^\circ$. At this angle, problems with the mechanical setup occurred. The nut, fixating the threaded rod at the setup arm, came loose and the measurement had to be interrupted. Because the arm is pushed and pulled by the stepper motor, play of the nut results in an offset in the angle depending on the movement direction to approach a position. As the steps were verified for a movement in one direction, this problem occurred at a change of moving direction and was accounted for with an uncertainty of $\pm 2.5^\circ$. This explains the discontinuity in the hit rate at $\beta = 15^\circ$. The fit in Figure 6.20b shows a dependency on $\sim 1/\sin^4(\theta/2)$ for large angles, as suggested for Rutherford scattering contributions described by Molière.

As the energy steps used in this chapter are not completely linear, the absolute beam energy values were taken into account for the plot in Figure 6.20c. The hit rate increases with rising energies, following an exponential course. This scan was performed for $\beta = 25^\circ$ and $d = 89 \text{ mm}$.

A study of the hit rates in dependency of the distance from origin resulted in a $1/d^2$ drop, shown in Figure 6.20d.

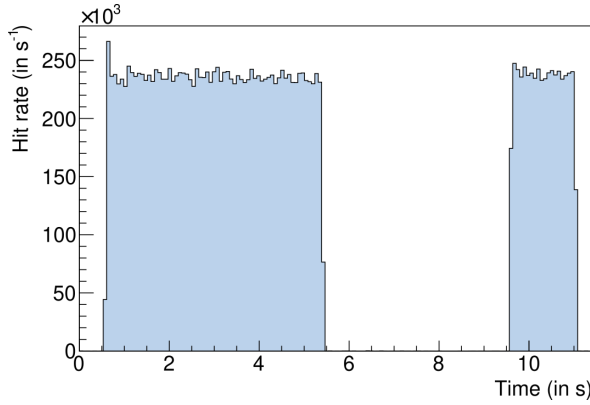
The maximum hit rate of 5.148 MHits/s is never reached. However, it must be noted that the beam test was not performed at maximum intensities. The intensities of the initial beam during the measurement had a value of $3 \times 10^6 \text{ particles/s}$, instead of the maximum for carbon ions with $5 \times 10^8 \text{ particles/s}$.

Further improvements of the setup concerning the readout rates are possible. The sensor design foresees an increase of the rates by a factor of about eight in the data transmission between sensor and FPGA. Using triggered readout mode instead of hit-driven readout mode, as used in this study, would additionally almost double the read out speed. Additional, a margin of factor ten was observed for comparing the limit and actual readout rate. With these improvements and a usage of the full potential readout speed during the measurements, full intensity application may be possible and allows further studies.

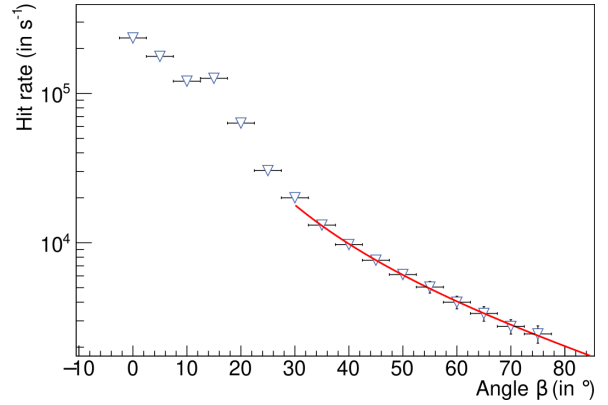
6.8. Summary

In the scope of this thesis, the suitability of HV-CMOS sensors for the detection of secondary particle tracks was studied, using ATLASpix3 as an example. A measurement procedure was developed on the basis of earlier studies with the hybrid silicon sensor TimePix. The used four-layer ATLASpix3 telescope had been built for earlier studies by R. Schimassek.

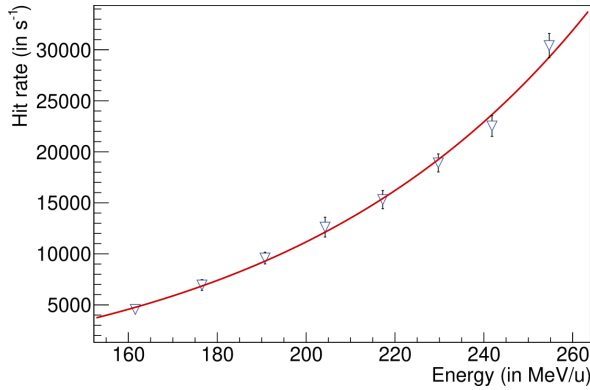
As an ideal future application realizes a full 3D-coverage of the irradiated tissue with secondary particle detectors, a mechanical setup was developed and built allowing an automated positioning



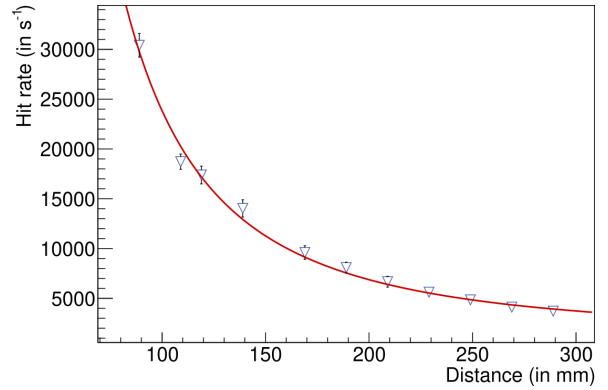
(a) Hit rate in layer four



(b) Mean hit rate in dependency of angle



(c) Mean hit rate in dependency of energy



(d) Mean hit rate in dependency of distance

Figure 6.20.: Hit rates during secondary particle tracking – (a) Two spills at one energy setting: $E = 110$, $\beta = 0^\circ$, and $d = 89$ mm, (b) Angle scan with $E = 110$, $d = 89$ mm; (c) Energy scan with $\beta = 25^\circ$, $d = 89$ mm; (d) Distance scan with $E = 110$, $\beta = 25^\circ$. All uncertainties on ordinate direction are estimated by an error propagation of the standard deviations. The uncertainty on the angle in Figure (b) is assumed with $\pm 2.5^\circ$ for each angle.

of the telescope around a head sized PMMA cylinder. The angle towards the beam axis can be varied in a range of 0° to 75° by a stepper motor and a threaded rod pushing or pulling the pivotable setup. The distance between the first telescope layer and the center of the PMMA cylinder, has a range of 89 mm – 289 mm and is adjustable via a linear stage.

A beam test was performed at HIT facility with the developed setup and a treatment plan with eight energies as used in patient treatments. The acquired data contains hits of – in total – 640 parameter settings.

The analysis was performed with the beam test data analysis framework *Corrvreckan*. To read in the data, the module [EventLoaderATLASp3] was developed, usable for binary and decoded data as generated by the GECCO system.

With *Corrvreckan*, analysis steps as alignment, clustering, correlations of layers, and tracking were performed. The cluster charge distributions show a typical Landau-Gaussian shape. Selecting clusters with different number of pixels, the MPV on the charge distribution changes. For cluster size one, a most probable charge generation value of $8950 e^-$ was found in the second telescope layer.

The residual distributions of recorded secondary particle tracks show standard deviations below the expected values of $p/\sqrt{12}$:

$$\sigma_{x, \text{res}} = 29.61 \mu\text{m} \leq 43.3 \mu\text{m}, \quad \sigma_{y, \text{res}} = 12.92 \mu\text{m} \leq 14.4 \mu\text{m}, \quad (6.7)$$

indicating good tracking results. Here, p describes the asymmetric sensor pixel pitch with $p_x = 150 \mu\text{m}$ and $p_y = 50 \mu\text{m}$. Small offsets of the track residual distributions in a nm range indicate a well aligned telescope. An origin of the tracks inside the PMMA cylinder was visible.

The detected secondary tracks were stored, visualized, and first attempts have been made to find the track origin and the correlating position of the Bragg peak. Further analysis is necessary for the determination of the Bragg position inside the PMMA cylinder and the accuracy of the measurements.

Improvements in the setup could be made for further studies. A smaller distance between the sensor layers could prevent a discarding of tracks and would improve the sensitivity of a telescope towards particle trajectories with larger angles. Additionally, for this purpose three layers would be sufficient. Thinned sensors should lead to a decrease of multiple scattering effects in the sensors and more precise tracking.

Further analysis steps contained the determination of hit rates for the comparison with rate limits of the telescope data processing. This analysis showed resolvable rates at all positions and energies. A maximum rate of 2.5×10^5 Hits/s in a single layer is an order of magnitude below the maximum possible readout rate of the chip at 2.5 MHits/s for the used readout speed. Further improvements of the setup concerning the readout rates are possible, as the system was not operated at full readout rate.

All in all, promising first results have been achieved in the secondary particle tracking with the HV-CMOS sensor ATLASp3. It could be shown that HV-CMOS sensors are capable of tracking charged secondary ion fragments generated during ion irradiation, and can cope with the secondary particle rates at moderate intensities at HIT.

7

Summary and Outlook

Cancer is one of the leading causes of death worldwide, although, different treatment options have been developed. Common treatments include radiation therapy with different types of particles, in which high doses of radiation destroy cancer cells and shrink the tumor. Especially radiation therapy with heavy ions is a spreading treatment method due to accurate energy deposition. Thereby, precise monitoring of the ion beam is indispensable for successful treatment. Further improvement of precision can be achieved with tracking of secondary particles produced by fragmentation processes during irradiation.

The HV-CMOS sensor technology is a new type of silicon sensors, invented by Ivan Perić in 2007. Reduced cost compared to hybrid pixel sensors and reduced material budget with monolithic sensor design make this technology interesting for beam monitoring applications. The presented thesis covers two topics, both of which address the question of whether monolithic HV-CMOS sensors are suited for use in monitoring of irradiation treatments with heavy ions. Two independent series of measurements were planned and conducted:

- Inhomogeneous X-ray irradiation study.
- Secondary particle tracking during irradiation with a medical ion beam.

For both campaigns, the monolithic sensor ATLASpix3 has been used.

X-Ray Irradiation Study

In the course of earlier studies, a stack of several ATLASpix3 sensors was irradiated at the beam dump of the Heidelberg Ion Therapy Center (HIT). There, the sensors were exposed to strongly inhomogeneous irradiation with protons and carbon ions at a mean energy of $E = 110 \text{ MeV/u}$. R. Schimassek showed reduced sensitivity for charged particles in the sensor matrix and a strong increase in noise hits and leakage current.

In this thesis, the influence of damaged readout electronics on these results was studied. Therefore, an iterative irradiation of an ATLASpix3 sample was performed at the X-ray tube at the Institute of Experimental Particle Physics (ETP). A total dose of 300 kGy was used which is comparable to the expected annual dose at HIT. A lead shielding allowed an inhomogeneous irradiation of a sensor region. The properties of the irradiated region were compared with an adjacent shielded region at each irradiation step.

During the studies, attention was paid to the detection efficiency and signal amplification. Therefore, results of test signal measurements and signals of characteristic X-rays were analysed. As a signal height is not directly measurable, the signal size was measured via the time over threshold (ToT) which is correlated to the signal size.

At a dose of 10 kGy, a significant drop down to 60% in the detection rate of characteristic X-rays of molybdenum was visible. For higher doses, the detection rates stabilize at high values. All pixels stayed sensitive until the end of campaign.

A calibration with monoenergetic X-rays allowed the determination of an individual pixel gain (in $\mu\text{V}/e^-$). Here, a gain increase by $\sim 0.3 \mu\text{V}/(e^- \text{ kGy})$ was observed. This hints to a

change of characteristics in the pixel amplification, as no additional threshold dispersion was found. The measured gain increase was induced by an increase of ToT with rising applied dose, depending on the initial signal size. This can have its origin in a higher signal size because of larger amplification, or in a longer signal due to a radiation induced change in the feedback: the feedback controls the signal length and shape, and therefore the ToT.

Additionally, an increase in leakage current by a factor of five at the total dose was visible. A steady increase in noise was measurable, reaching 1.5 times the initial value after the full applied dose. Both values are orders of magnitude below the results from the irradiation with protons and carbon ions, which matches with the expectation that no bulk damage is expected for ionizing radiation. Also, no pixels were lost in the irradiation. Therefore, the problematic effects encountered in the HIT beam dump irradiation seem to be caused by radiation damage in the sensor bulk.

Secondary Particle Tracking at Medical Treatment Facility

Monitoring of the primary ion beam is essential for radiation therapy. Further, non-invasive and in-vivo monitoring methods during irradiation treatments could improve the precision and therefore, treatment success. Promising studies on the detection of secondary particle tracks and their origin, achieving precisions of $<1 \text{ mm}^3$, were previously performed with a two-layer hybrid silicon pixel sensor setup.

In this thesis, the capability of monolithic HV-CMOS sensors at detecting charged secondary particle tracks during an irradiation at HIT was studied. A telescope consisting of four ATLASpix3 sensors, designed, built, and tested by R. Schimassek, was used during these studies.

A mechanical setup for automated positioning of the telescope setup was designed and built. The beam tests took place at HIT facility with realistic treatment energies and a PMMA cylinder as target. The particle track analysis was performed with the beam test data analysis framework *Corryvreckan*. The framework was extended by a module for loading and integrating the data format of the ATLASPix3 telescope.

The residual distributions of recorded secondary particle tracks show standard deviations of:

$$\sigma_{x, \text{res}} = 29.61 \text{ } \mu\text{m} \leq \frac{p_x}{\sqrt{12}} = 43.3 \text{ } \mu\text{m}, \quad \sigma_{y, \text{res}} = 12.92 \text{ } \mu\text{m} \leq \frac{p_y}{\sqrt{12}} = 14.4 \text{ } \mu\text{m},$$

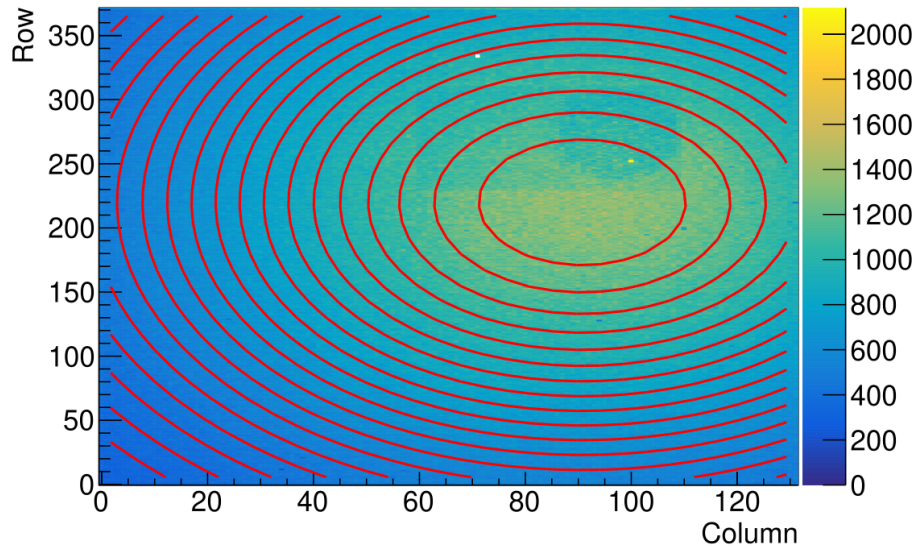
indicating good tracking results, as the values are below the spatial resolution of the individual sensors with $p/\sqrt{12}$. Here, p denotes the pixel pitch of the rectangular pixels with $p_x = 150 \text{ } \mu\text{m}$ and $p_y = 50 \text{ } \mu\text{m}$. It was shown that the secondary particle tracks originate from inside the PMMA cylinder. A reconstruction of penetration depth depending on the beam energy was not successful in the scope of this thesis and offers room for further analyses.

For the suitability studies, an estimation of the resolvable rates of the ATLASpix3 readout system was performed and compared with the actual secondary particle rates. The hit rate of the first telescope layer at highest energy and smallest distance and angle was determined to be $2.5 \times 10^5 \text{ Hits/s}$. This is an order of magnitude below the maximum resolvable rate per layer with $2.5 \times 10^6 \text{ Hits/s}$. Thus, the limit rate of $5.148 \times 10^6 \text{ Hits/s}$ was not exceeded. Further improvements of the setup concerning the readout rates are possible because the system was not operated at full readout rates. Therefore, further studies at higher beam intensities are possible, based on the good tracking results achieved in this study.

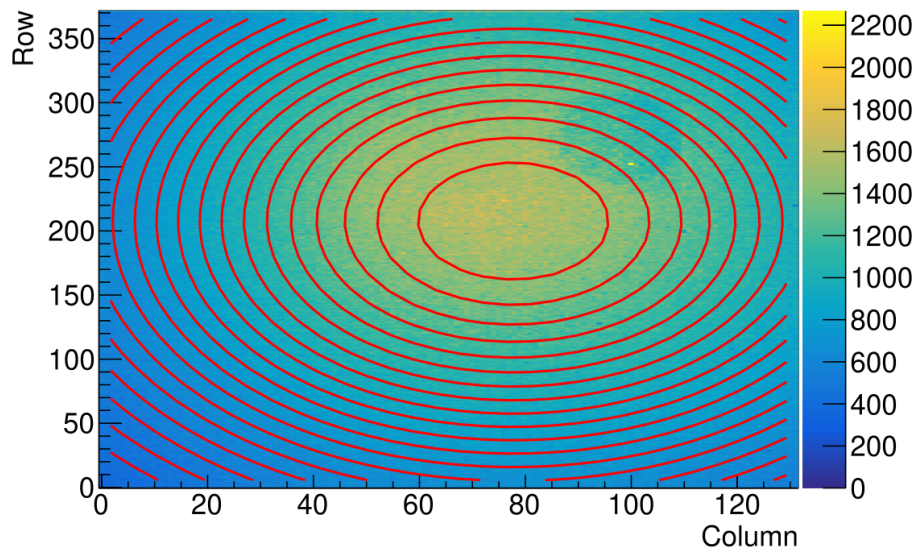
All in all, promising first results have been achieved in the secondary particle tracking with the HV-CMOS sensor ATLASpix3. It could be shown that HV-CMOS sensors are capable of tracking charged secondary ion fragments generated during ion irradiation, and can cope with the secondary particle rates at moderate intensities at HIT.



Irradiation Study with ATLASpix3



(a) ^{90}Sr source position during measurement (60 kGy)



(b) ^{90}Sr source position during measurement (110 kGy)

Figure A.1.: Shift of strontium source during measurements – The Gaussian profiles of the ^{90}Sr source positions suggest an asymmetric placement of the active source part and explains the differences in the rate distribution. The determined Gaussian means have a distance of (2.054 ± 0.005) mm.

B

Secondary Particle Studies with ATLASpix3 Telescope

B.1. Slow Neutron Conversion with Polyethylene (PE)

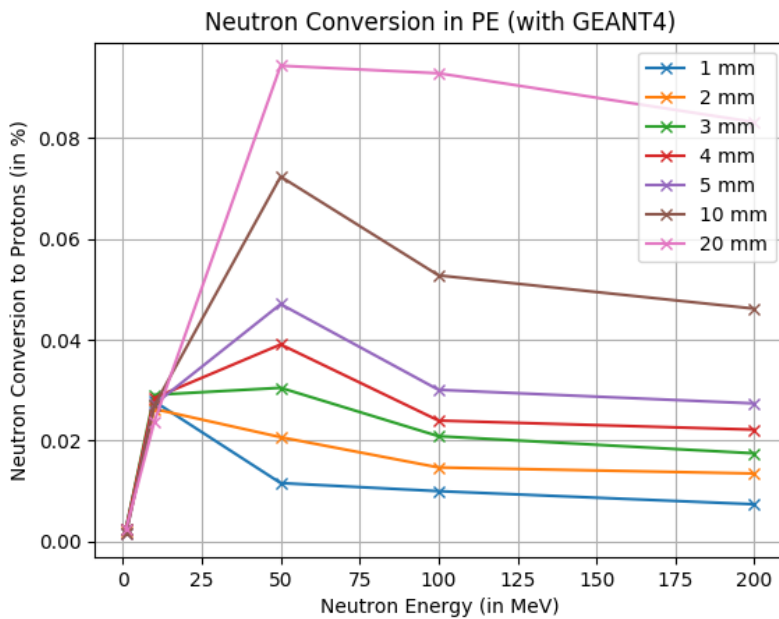


Figure B.1.: GEANT4 simulation of the conversion of neutrons in protons in polyethylene (PE) – As neutrons have neutral electrical charge they are hardly detectable with silicon sensors. Due to high amounts of hydrogen, PE is a suitable converter for slow neutrons. The plot shows neutron conversion rates into detectable protons at different thicknesses of PE and energies. The thicker the PE layer, the higher the percentage of converted neutrons.

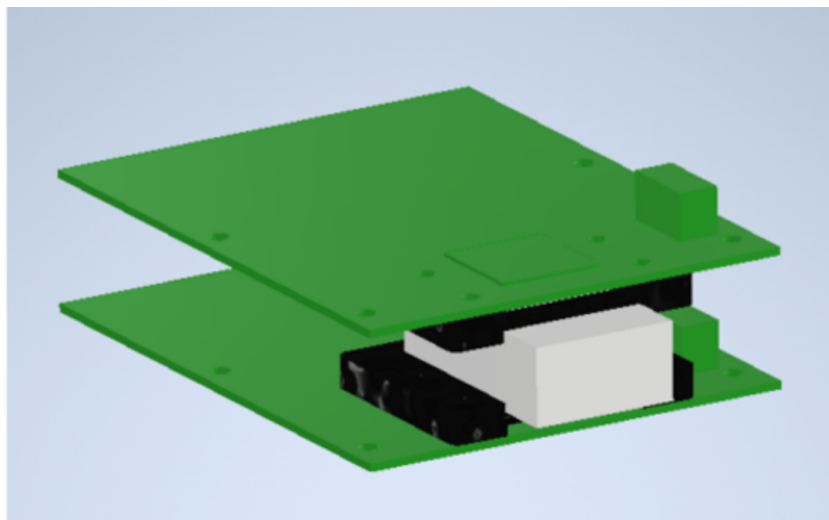


Figure B.2.: Sketch of built-in neutron converter between sensor layers – A holder for a polyethylene (PE) converter was designed and fabricated. This allowed measurements at the beam test with a PE converter.

B.2. Pre-Characterization of Sensor Layers

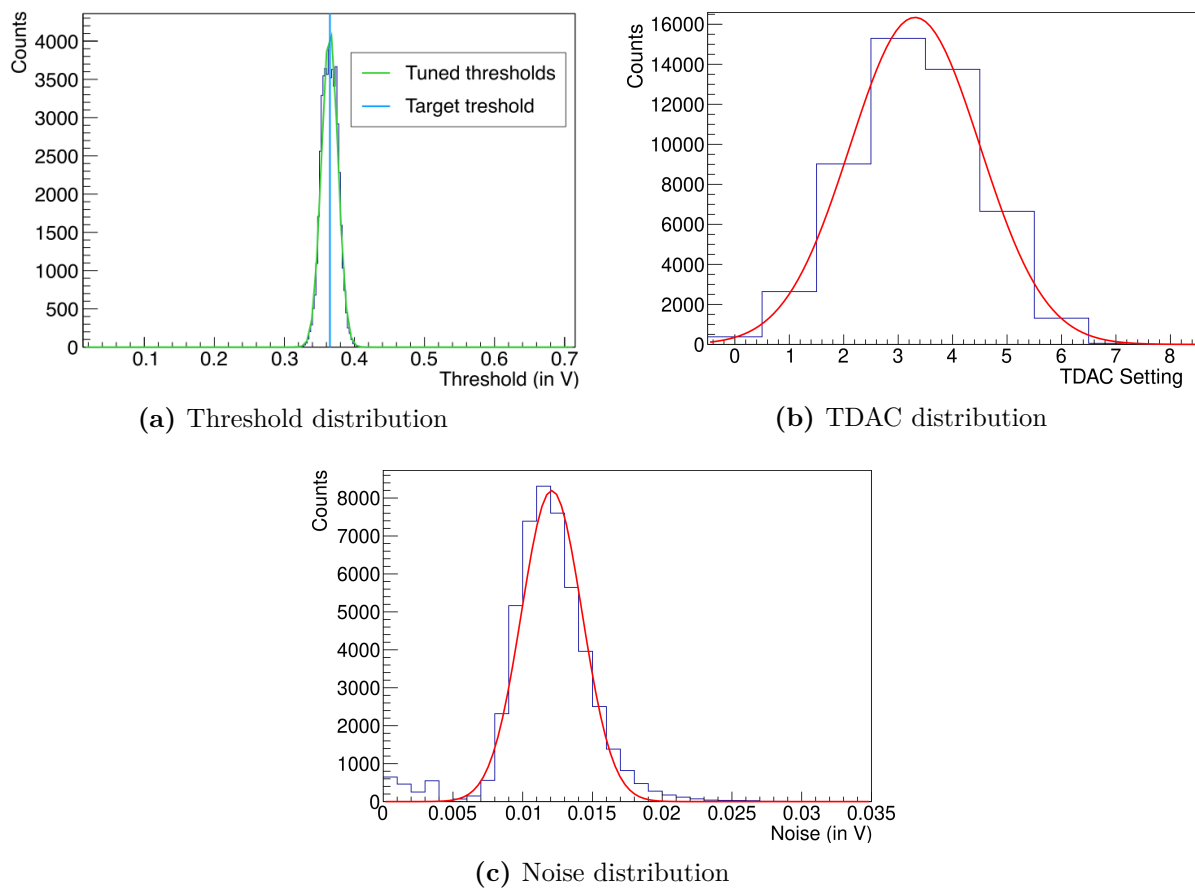


Figure B.3.: Characterization of AP3.8 – Results of the tuning procedure: (a) Threshold distribution of sensor matrix (green) around the target threshold (blue): 0.365 V. (b) TDAC distribution with Gaussian fit: mean value $\mu = 3.31$, and standard deviation $\sigma = 1.19$. (c) Noise distribution with Gaussian fit: mean value $\mu = 12.1$ mV, and standard deviation $\sigma = 2.2$ mV.

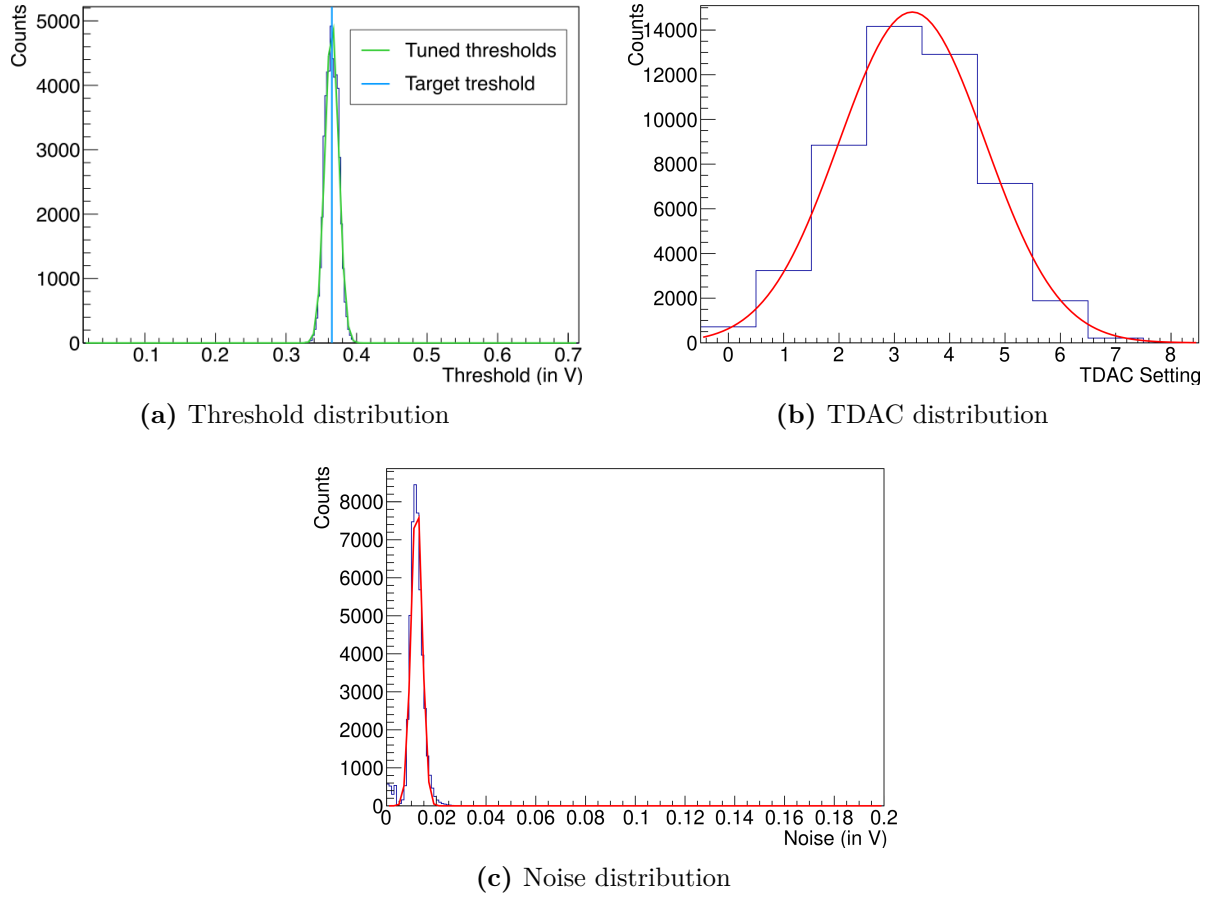


Figure B.4.: Characterization of AP3.9 – Results of the tuning procedure: (a) Threshold distribution of sensor matrix (green) around the target threshold (blue): 0.365 V. (b) TDAC distribution with Gaussian fit: mean value $\mu = 3.32$, and standard deviation $\sigma = 1.32$. (c) Noise distribution with Gaussian fit: mean value $\mu = 12.1$ mV, and standard deviation $\sigma = 2.2$ mV.

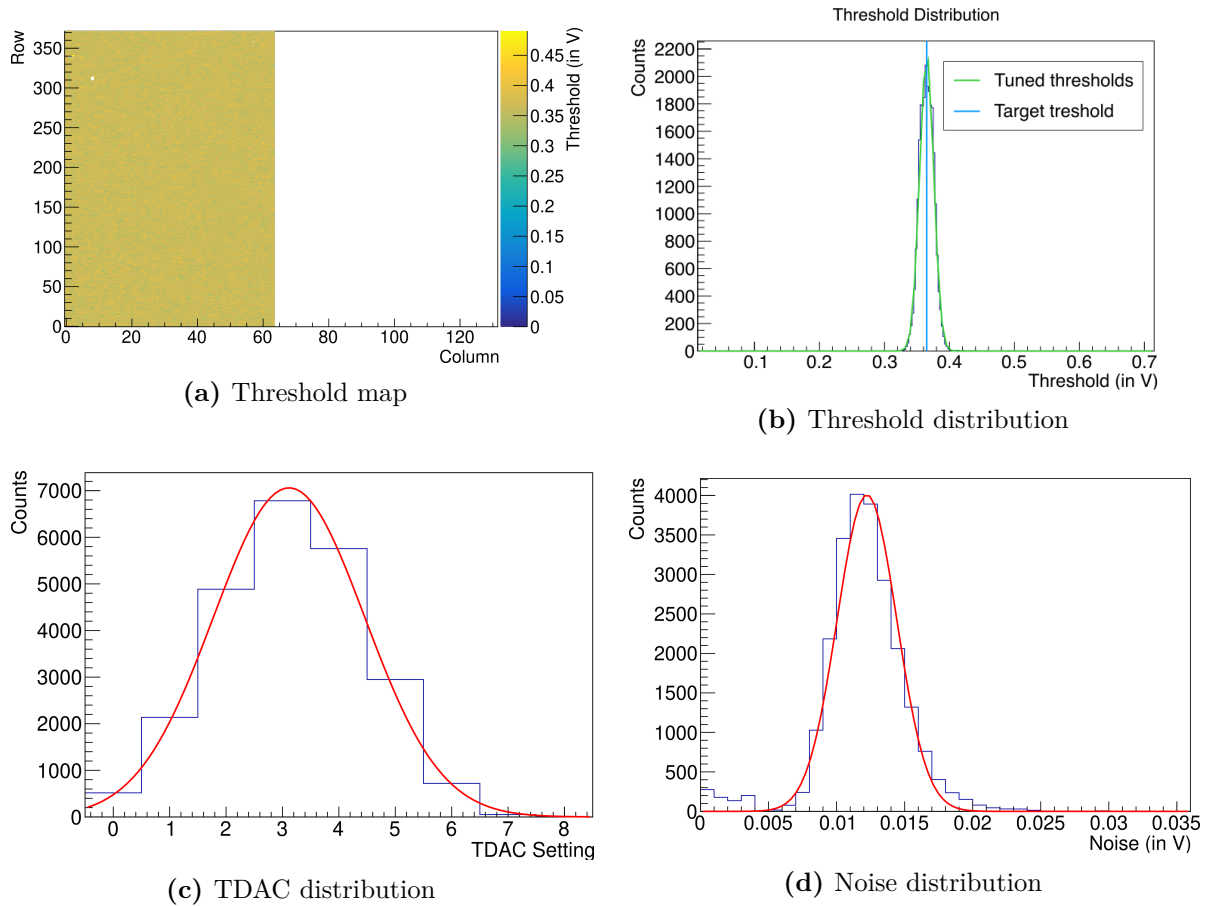


Figure B.5.: Characterization of AP3.11 (1) – Results of the tuning procedure: (a) Due to a damaged column (64), the scan of the tuning procedure had to be split in two parts (see Figure B.6). (b) Threshold distribution of sensor matrix (green) around the target threshold (blue): 0.365 V. (c) TDAC distribution with Gaussian fit: mean value $\mu = 3.12$, and standard deviation $\sigma = 1.34$. (d) Noise distribution with Gaussian fit: mean value $\mu = 12.2$ mV, and standard deviation $\sigma = 2.2$ mV.

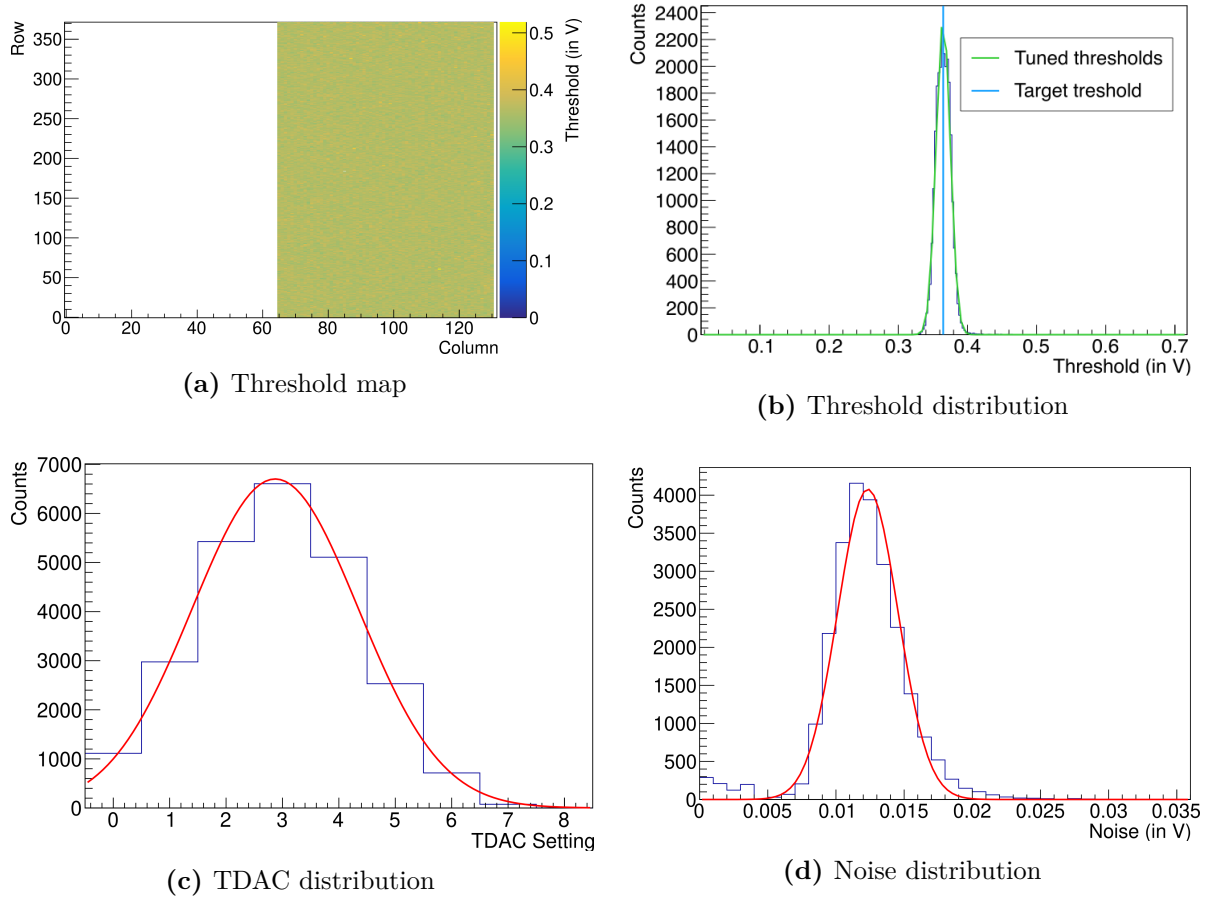


Figure B.6.: Characterization of AP3.11 (2) – Results of the tuning procedure: (a) Due to a damaged column (64), the scan of the tuning procedure had to be split in two parts (see Figure B.5). (b) Threshold distribution of sensor matrix (green) around the target threshold (blue): 0.365 V. (c) TDAC distribution with Gaussian fit: mean value $\mu = 2.87$, and standard deviation $\sigma = 1.47$. (d) Noise distribution with Gaussian fit: mean value $\mu = 12.3$ mV, and standard deviation $\sigma = 2.2$ mV.

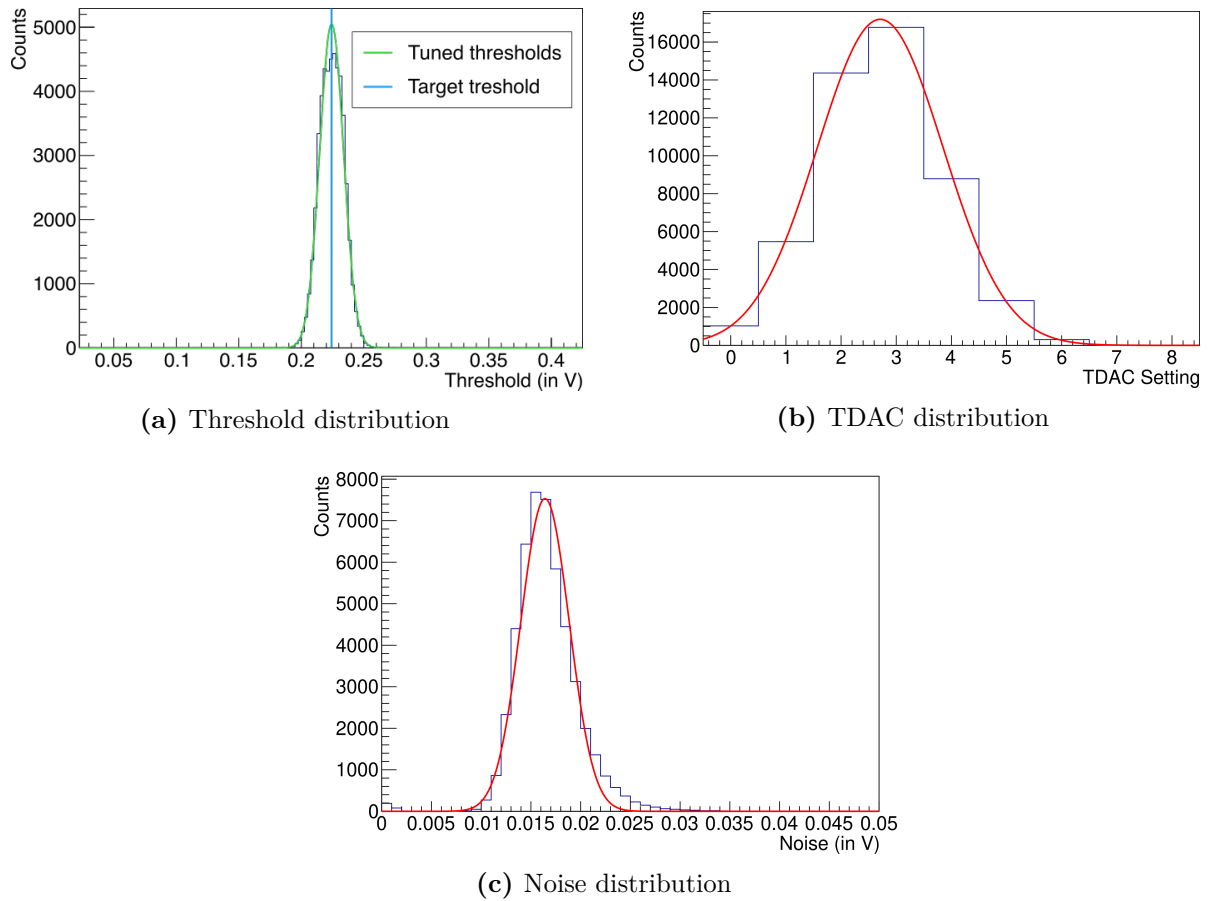


Figure B.7.: Characterization of AP3.4 – Results of the tuning procedure: (a) Threshold distribution of sensor matrix (green) around the target threshold (blue): 0.224 V. (b) TDAC distribution with Gaussian fit: mean value $\mu = 2.7$. (c) Noise distribution with Gaussian fit: mean value $\mu = 8.8$ mV (from [Sch21b])

B.3. Corryvreckan Configuration Files

Exemplary Configuration File

File B.1.: Configuration file for Corryvreckan – The used analysis modules (in brackets) are given with additional information as e.g. spatial and time cuts. The determined parameters and histograms are printed into specified output files.

```
[Corryvreckan]
output_directory = "../output/CorryOutput_e40_d89"
detectors_file = "../geometries/ap3_alignment_telescope_aligned.geo"

histogram_file = "histograms_ap3_telescope_analysis_z12_e40_a10_d89.root"

number_of_tracks = 100000

[Metronome]
event_length = 5us

[EventLoaderATLASPix3]
input_directory = ".././data_atlaspix3_telescope/Datasets_e40_d89"
input_filename = "HIT_TB_Teleskop_210622_z12_e40_a10_d89.dat"

clock_cycle = 50ns

calibration_path = "../calibration/"
calibration_clock_cycle = 100ns

[Clustering4D]
time_cut_abs = 200ns

[Correlations]

[Tracking4D]
track_outputfile = "track_params_z12_e40_a10_d89_track_output.dat"
min_hits_on_track = 3
spatial_cut_abs = 225um, 75um
time_cut_abs = 250ns
exclude_dut = false
momentum = 100MeV

#[AlignmentTrackChi2]
#iterations = 4
```

Exemplary Masking File

File B.2.: Exemplary file with information about masked pixels – This file shows the masked damaged column 64 of sensor AP3.11. A masking of rectangular regions was implemented in the [EventLoaderATLASPix3] of the *Corryvreckan* framework. Here, the lower left and the upper right pixel have to be defined by their column and row address.

```
#####
#####
####  Mask Pixel File - rectangular pixel regions to be masked  ####
####  Region can be defined by coordinates of lower left (ll) and  ####
####  upper right (ur) corner.                                     ####
#####
#####
# c_ll;      r_ll; c_ur; r_ur
64          0      64      371
```

Exemplary ToT Calibration File

File B.3.: Exemplary ToT calibration file – The ToT calibration fitting parameters for each of the 49 104 pixels in the matrix are stored in files, read in during the analysis with *Corryvreckan* framework. The uncertainties originate from the ToT calibration and are not considered in the further analysis.

```
# Fit Parameters for ToT Calibration
# Pixel (0|0)
x0      0.0881217 +- 0.27818
offset  -8.91938 +- 71.9387
lnscale 14.775 +- 13.4017
linear  -0.285458 +- 10.6937

# Pixel (1|0)
x0      0.129492 +- 0.353782
offset  -16.6032 +- 102.125
lnscale 22.6382 +- 28.4718
linear  17.8093 +- 23.5124

# Pixel (2|0)
x0      0.174554 +- 0.379531
offset  -4.639 +- 68.0911
lnscale 18.6491 +- 27.3744
linear  19.9162 +- 23.9857

...
```

Telescope Geometry File after Alignment

File B.4.: Telescope geometry file for Corryvreckan after alignment – All four layers are defined as detectors in this file. The nearest sensor to the PMMA cylinder was chosen as the reference layer. During analysis, the translational and orientational offsets are corrected for each layer by the values given in this file.

```
[ATLASPix3_0]
number_of_pixels = 132, 372
orientation = -0.265394deg, -3.70583deg, 0.125535deg
orientation_mode = "xyz"
pixel_pitch = 150um, 50um
position = 40.502um, -58.98um, 164mm
spatial_resolution = 43.3um, 14.4um
time_resolution = 50ns
type = "ATLASPix3"

[ATLASPix3_1]
number_of_pixels = 132, 372
orientation = 0.013751deg, -3.04722deg, -0.130634deg
orientation_mode = "xyz"
pixel_pitch = 150um, 50um
position = 102.199um, 155.286um, 139mm
spatial_resolution = 43.3um, 14.4um
time_resolution = 50ns
type = "ATLASPix3"

[ATLASPix3_2]
number_of_pixels = 132, 372
orientation = -0.191654deg, -2.18217deg, 0.816522deg
orientation_mode = "xyz"
pixel_pitch = 150um, 50um
position = 50.558um, 15.3um, 114mm
spatial_resolution = 43.3um, 14.4um
time_resolution = 50ns
type = "ATLASPix3"

[ATLASPix3_3]
number_of_pixels = 132, 372
orientation = 0deg, 0deg, 0deg
orientation_mode = "xyz"
pixel_pitch = 150um, 50um
position = 18um, 0um, 89mm
role = "reference"
spatial_resolution = 43.3um, 14.4um
time_resolution = 50ns
type = "ATLASPix3"
```

Bibliography

- [Ahl80] S. P. Ahlen. *Theoretical and experimental aspects of the energy loss of relativistic heavily ionizing particles*. In: Rev. Mod. Phys. 52 (1 Jan. 1980), pp. 121–173. DOI: 10.1103/RevModPhys.52.121 (cited on pp. 12, 31).
- [ATL+08] ATLAS Collaboration et al. *The ATLAS Experiment at the CERN Large Hadron Collider*. In: Journal of Instrumentation 3.08 (Aug. 2008), S08003–S08003. DOI: 10.1088/1748-0221/3/08/s08003 (cited on p. 29).
- [ATL14] ATLAS Collaboration. *Operation and performance of the ATLAS semiconductor tracker*. In: Journal of Instrumentation 9.08 (Aug. 2014), P08009–P08009. ISSN: 1748-0221. DOI: 10.1088/1748-0221/9/08/p08009 (cited on p. 29).
- [ATL17] ATLAS Collaboration. *Technical Design Report for the ATLAS Inner Tracker Pixel Detector*. Tech. rep. Geneva: CERN, Sept. 2017. URL: <https://cds.cern.ch/record/2285585> (cited on pp. 1, 29, 37).
- [ATL19] ATLAS Collaboration. *Expected Tracking Performance of the ATLAS Inner Tracker at the HL-LHC*. Tech. rep. Geneva: CERN, Mar. 2019. URL: <https://cds.cern.ch/record/2669540> (cited on pp. 1, 29).
- [ATL21a] ATLAS Collaboration. *The ATLAS Detector*. 2021. URL: <https://atlas.cern/discover/detector> (visited on 11/19/2021) (cited on p. 29).
- [ATL21b] ATLAS Collaboration. *Trigger and Data Acquisition*. 2021. URL: <https://atlas.cern/discover/detector/trigger-daq> (visited on 12/16/2021) (cited on p. 29).
- [Aug+19] H. Augustin et al. *Performance of the large scale HV-CMOS pixel sensor MuPix8*. In: Journal of Instrumentation 14.10 (Oct. 2019), pp. C10011–C10011. DOI: 10.1088/1748-0221/14/10/c10011 (cited on p. 58).
- [Bas+12] R. Baskar et al. *Cancer and Radiation Therapy: Current Advances and Future Directions*. In: Int J Med Sci 9 (2012), pp. 193–199. DOI: 10.7150/ijms.3635 (cited on p. 31).
- [Bej+17] I. Bejar et al. *High-Luminosity Large Hadron Collider (HL-LHC) Technical Design Report V. 0.1*. Sept. 2017. ISBN: 9789290834717 (cited on pp. 1, 29).
- [Ber+17] M. Berger et al. *Stopping-Power & Range Tables for Electrons, Protons, and Helium Ions*. Tech. rep. Washington, D.C.: U.S. Department of Commerce, July 2017. DOI: <https://dx.doi.org/10.18434/T4NC7P> (cited on p. 39).
- [BK05] W. Bragg and R. Kleeman. XXXIX. *On the α particles of radium, and their loss of range in passing through various atoms and molecules*. In: The London, Edinburgh, and Dublin Philosophical Magazine and Journal of Science 10.57 (1905), pp. 318–340. DOI: 10.1080/14786440509463378. eprint: <https://doi.org/10.1080/14786440509463378> (cited on p. 67).
- [Ble13] J. Bleck-Neuhaus. *Elementare Teilchen (Von den Atomen über das Standard-Modell bis zum Higgs-Boson)*. 2nd ed. Springer Spektrum, Berlin, Heidelberg, 2013. ISBN: 978-3-642-32579-3. URL: <https://doi.org/10.1007/978-3-642-32579-3> (cited on p. 36).
- [Bor18] G. Borghello. *Ionizing radiation effects in nanoscale CMOS technologies exposed to ultra-high doses*. Ph.D. dissertation. University of Udine, 2018 (cited on p. 13).

- [Brä08] M. Bräuer. *Proven Outcomes Oncology Solutions - Commissioning of the Siemens Beam Application and Monitoring System*. copyright Siemens AG. May 2008. URL: https://www.ptcog.ch/archive/conference_p&t&v/PTCOG47/presentations/6_Meeting_Saturday/Session5/Braeuer_Ptcog47/Ptcog47_Sat_Braeuer_SiemensFinal.pdf (cited on pp. 34, 35).
- [Bre11] J. R. Brews. *Semiconductor - Density of States*. Jan. 2011. URL: <https://en.citizendium.org/wiki/Semiconductor> (visited on 11/20/2021) (cited on p. 5).
- [Brü+04] O. S. Brüning et al. *LHC Design Report*. CERN Yellow Reports: Monographs. Geneva: CERN, 2004. DOI: 10.5170/CERN-2004-003-V-1 (cited on pp. 27, 28).
- [Cap+10] M. Capeans et al. *ATLAS Insertable B-Layer Technical Design Report*. Tech. rep. Sept. 2010. URL: <https://cds.cern.ch/record/1291633> (cited on p. 28).
- [Cor12] Corporate Communication and Press Office, Heidelberg University Hospital. *Heidelberger Ion Beam Therapy Center*. Oct. 2012. URL: https://www.klinikum.uni-heidelberg.de/fileadmin/hit/dokumente/121019KV_SS_HITImage_engl_web_ID17763.pdf (visited on 11/22/2021) (cited on p. 33).
- [Cor21] Corryvreckan authors. *Corryvreckan: a modular 4D track reconstruction and analysis software for test beam data - Object: StraightLineTrack*. 2021. URL: <https://gitlab.cern.ch/corryvreckan/corryvreckan/-/blob/master/src/objects/StraightLineTrack.cpp#L48> (visited on 01/02/2022) (cited on p. 77).
- [Cus11] D. Cussol. *Hadron therapy*. In: (Sept. 2011). URL: https://www.researchgate.net/publication/278800705_Hadron_therapy (cited on p. 36).
- [Dan+21] D. Dannheim et al. *Corryvreckan: a modular 4D track reconstruction and analysis software for test beam data*. In: *Journal of Instrumentation* 16 (Mar. 2021), P03008. DOI: 10.1088/1748-0221/16/03/P03008 (cited on pp. 2, 77).
- [Del+05] G. Delaney et al. *The role of radiotherapy in cancer treatment: estimating optimal utilization from a review of evidence-based clinical guidelines*. In: *Cancer* 104 (6 Sept. 2005), pp. 1129–1137. DOI: 10.1002/cncr.21324 (cited on p. 31).
- [Dem14] W. Demtröder. *Experimentalphysik 4 - Kern-, Teilchen- und Astrophysik*. 4th ed. Springer Spektrum, Berlin, Heidelberg, 2014. ISBN: 978-3-642-21476-9. DOI: <https://doi.org/10.1007/978-3-642-21476-9> (cited on pp. 8, 10, 12).
- [Dro18] A. Droll. *Characterization and Performance Study of Prototype Modules equipped with the CMS Binary Chip*. Master’s thesis. Karlsruhe Institute of Technology (KIT), 2018 (cited on p. 13).
- [DS08] O. Deleage and P. Scott. *Modes of operation of an N-type MOSFET*. Sept. 2008. URL: <https://en.wikipedia.org/wiki/MOSFET> (visited on 11/26/2021) (cited on p. 6).
- [dS87] J. A. del Alamo and R. M. Swanson. *Modelling of minority-carrier transport in heavily doped silicon emitters*. In: *Solid-State Electronics* 30.11 (1987), pp. 1127–1136. ISSN: 0038-1101. DOI: [https://doi.org/10.1016/0038-1101\(87\)90077-3](https://doi.org/10.1016/0038-1101(87)90077-3) (cited on p. 19).
- [Ehr15] F. Ehrler. *Development of active CMOS sensors for particle physics experiments*. Master’s thesis. 2015. DOI: 10.5445/IR/1000055062 (cited on pp. 16, 22, 43, 60).
- [Ehr21] F. Ehrler. *Characterization of monolithic HV-CMOS pixel sensors for particle physics experiments*. Ph.D. dissertation. Karlsruher Institut für Technologie (KIT), 2021 (cited on pp. 1, 10, 19–21, 23, 35).

-
- [Eli21] U. Elicabuk. *Development of an Iterative Irradiation Setup and Online Beam Monitor for Silicon Sensor Irradiation Studies*. Master's thesis. Karlsruhe Institute of Technology (KIT), 2021 (cited on p. 71).
- [Fah+16] L. Fahrmeir et al. *Statistik, Der Weg zur Datenanalyse*. 8th ed. Springer, Berlin, Heidelberg, 2016. ISBN: 978-3-662-50371-3. DOI: <https://doi.org/10.1007/978-3-662-50372-0> (cited on p. 55).
- [Fai83] Fairchild Semiconductor. *CMOS, the Ideal Logic Family*. Application Note 77. 1983. URL: <https://web.archive.org/web/20150109070537/https://www.fairchildsemi.com/application-notes/AN/AN-77.pdf> (cited on p. 8).
- [Fél+21] R. Félix-Bautista et al. *Quality assurance method for monitoring of lateral pencil beam positions in scanned carbon-ion radiotherapy using tracking of secondary ions*. In: *Medical Physics* 48.8 (June 2021), pp. 4411–4424. DOI: <https://doi.org/10.1002/mp.15018>. eprint: <https://aapm.onlinelibrary.wiley.com/doi/pdf/10.1002/mp.15018> (cited on pp. 2, 37).
- [FS96] A. Ferrari and P. R. Sala. *The Physics of High Energy Reactions*. Workshop on Nuclear Reaction Data and Nuclear Reactors Physics, Design and Safety. May 1996. URL: <https://cds.cern.ch/record/682497/files/phys-97-113.pdf> (cited on p. 36).
- [GM14] R. Gross and A. Marx. *Festkörperphysik*. De Gruyter Oldenbourg, 2014. ISBN: 9783110358704. DOI: [doi:10.1524/9783110358704](https://doi.org/10.1524/9783110358704) (cited on p. 4).
- [Gra+20] C. Grau et al. *Particle therapy in Europe*. In: *Molecular Oncology* 14.7 (2020), pp. 1492–1499. DOI: <https://doi.org/10.1002/1878-0261.12677>. eprint: <https://febs.onlinelibrary.wiley.com/doi/pdf/10.1002/1878-0261.12677> (cited on p. 32).
- [Gwo+13] K. Gwosch et al. *Non-invasive monitoring of therapeutic carbon ion beams in a homogeneous phantom by tracking of secondary ions*. In: *Physics in Medicine & Biology* 58.11 (May 2013), pp. 3755–3773. DOI: [10.1088/0031-9155/58/11/3755](https://doi.org/10.1088/0031-9155/58/11/3755) (cited on pp. 2, 37, 67–69, 88).
- [Hab+04] T. Haberer et al. *The Heidelberg Ion Therapy Center*. In: *Radiotherapy and Oncology* 73 (2004). Carbon-Ion Therapy, S186–S190. ISSN: 0167-8140. DOI: [https://doi.org/10.1016/S0167-8140\(04\)80046-X](https://doi.org/10.1016/S0167-8140(04)80046-X) (cited on pp. 1, 32).
- [Har17] F. Hartmann. *Evolution of Silicon Sensor Technology in Particle Physics*. 2nd ed. Springer, Nov. 3, 2017. ISBN: 978-3-319-64434-9. DOI: [10.1007/978-3-319-64436-3](https://doi.org/10.1007/978-3-319-64436-3) (cited on p. 13).
- [Hen06] M. Hennig. *Dotierung im Siliciumkristallgitter*. Jan. 2006. URL: <https://de.wikipedia.org/wiki/Dotierung> (visited on 11/26/2021) (cited on p. 5).
- [HM06] W. Herr and B. Muratori. *Concept of luminosity*. In: (2006). DOI: [10.5170/CERN-2006-002.361](https://doi.org/10.5170/CERN-2006-002.361) (cited on p. 1).
- [Ins20] Institute of Experimental Particle Physics - Karlsruhe Institute of Technology. *X-Ray Irradiation*. Aug. 2020. URL: <https://www.etp.kit.edu/english/265.php> (visited on 11/25/2021) (cited on p. 41).
- [Jak+11] J. Jakubek et al. *Selective detection of secondary particles and neutrons produced in ion beam therapy with 3D sensitive voxel detector*. In: *Journal of Instrumentation* 6.12 (Dec. 2011), pp. C12010–C12010. DOI: [10.1088/1748-0221/6/12/c12010](https://doi.org/10.1088/1748-0221/6/12/c12010) (cited on pp. 12, 70).

- [Kie+18] M. Kiehn et al. *Performance of CMOS pixel sensor prototypes in ams H35 and aH18 technology for the ATLAS ITk upgrade*. In: (July 2018) (cited on pp. 1, 20).
- [Kir+86] J. Kirz et al. *Center for X-ray Optics, X-ray Data Booklet*. Apr. 1, 1986. URL: https://xdb.lbl.gov/Section1/Table_1-2.pdf (cited on p. 45).
- [KIT19] KIT ADL. *ATLASPIX3 user manual*. June 2019. URL: https://adl.ipe.kit.edu/downloads/ATLASPIX3_um_v1.pdf (cited on p. 89).
- [Kob15] D. Kobayashi. *Performance of the ATLAS Muon Trigger in Run I and Upgrades for Run II*. In: *Journal of Physics, Conference Series* 664 (Dec. 2015), p. 092016. DOI: 10.1088/1742-6596/664/9/092016 (cited on p. 29).
- [KOW09] C. Kleffner, D. Ondreka, and U. Weinrich. *The Heidelberg Ion Therapy (HIT) Accelerator Coming into Operation*. In: *AIP Conference Proceedings* 1099.1 (2009), pp. 426–428. DOI: 10.1063/1.3120065 (cited on p. 32).
- [Kra15] A. C. Kraan. *Range Verification Methods in Particle Therapy: Underlying Physics and Monte Carlo Modeling*. In: *Frontiers in Oncology* 5 (2015), p. 150. ISSN: 2234-943X. DOI: 10.3389/fonc.2015.00150 (cited on pp. 2, 35, 36).
- [Kri+18] J. Krimmer et al. *Prompt-gamma monitoring in hadrontherapy: A review*. In: *Nuclear Instruments and Methods in Physics Research Section A: Accelerators, Spectrometers, Detectors and Associated Equipment* 878 (2018). *Radiation Imaging Techniques and Applications*, pp. 58–73. ISSN: 0168-9002. DOI: <https://doi.org/10.1016/j.nima.2017.07.063> (cited on pp. 31, 37).
- [KW16] H. Kolanoski and N. Wermes. *Teilchendetektoren - Grundlagen und Anwendungen*. 1st ed. Springer Spektrum, Berlin, Heidelberg, 2016. ISBN: 978-3-662-45350-6. DOI: <https://doi.org/10.1007/978-3-662-45350-6> (cited on pp. 8, 9, 13, 14, 16, 17, 19).
- [Lab05] Laboratoire National Henri Becquerel. *Atomic and Nuclear data*. Nov. 2005. URL: <http://www.lnhb.fr/nuclear-data/nuclear-data-table/> (visited on 12/30/2021) (cited on p. 46).
- [LD91] G. R. Lynch and O. I. Dahl. *Approximations to multiple Coulomb scattering*. In: *Nuclear Instruments and Methods in Physics Research Section B: Beam Interactions with Materials and Atoms* 58.1 (1991), pp. 6–10. ISSN: 0168-583X. DOI: [https://doi.org/10.1016/0168-583X\(91\)95671-Y](https://doi.org/10.1016/0168-583X(91)95671-Y) (cited on p. 12).
- [LHC12] LHCb Collaboration. *For LHCb Talks*. General Photo. July 2012. URL: <https://cds.cern.ch/record/1463546> (cited on p. 28).
- [Lom09] A. J. Lomax. *Charged Particle Therapy: The Physics of Interaction*. In: *The Cancer Journal* 15.4 (July 2009), pp. 285–291. DOI: 10.1097/PP0.0b013e3181af5cc7 (cited on p. 32).
- [Mar20] R. Marco-Hernández. *Overview of CMOS Sensors for Future Tracking Detectors*. In: *Instruments* 4.4 (2020). ISSN: 2410-390X. DOI: 10.3390/instruments4040036 (cited on p. 20).
- [May97] T. Mayer-Kuckuk. *Atomphysik - Eine Einführung*. 5th ed. Vieweg+Teubner Verlag, Springer Fachmedien Wiesbaden GmbH, Wiesbaden, 1997. ISBN: 978-3-663-01606-9. URL: <https://doi.org/10.1007/978-3-663-01606-9> (cited on p. 41).
- [MMR69] H. D. Maccabee, U. Madhvanath, and M. R. Raju. *Tissue activation studies with alpha-particle beams*. In: *Physics in Medicine & Biology* 14.2 (Apr. 1969), pp. 213–224. DOI: 10.1088/0031-9155/14/2/304 (cited on p. 36).

-
- [Mol99] M. Moll. *Radiation Damage in Silicon Particle Detectors*. PhD thesis. University of Hamburg, 1999. URL: <https://mmoll.web.cern.ch/mmoll/thesis/> (cited on p. 64).
- [MRS02] O. Madelung, U. Rössler, and M. Schulz. *Silicon (Si), band structure: Datasheet from Landolt-Börnstein - Group III Condensed Matter, Volume 41A1β: "Group IV Elements, IV-IV and III-V Compounds. Part b - Electronic, Transport, Optical and Other Properties"*. 2002. DOI: 10.1007/10832182_432 (cited on p. 5).
- [Mül21] J.-O. Müller-Gosewisch. *Investigation of Radiation Damage in Silicon Sensors for the Phase-2 Upgrade of the CMS Outer Tracker*. Ph.D. dissertation. Karlsruhe Institute of Technology (KIT), 2021 (cited on p. 40).
- [NZ15] W. D. Newhauser and R. Zhang. *The physics of proton therapy*. In: *Physics in Medicine and Biology* 60.8 (Mar. 2015), R155–R209. DOI: 10.1088/0031-9155/60/8/r155 (cited on p. 67).
- [Pau85] W. Pauli. *Wolfgang Pauli - Wissenschaftlicher Briefwechsel mit Bohr, Einstein, Heisenberg u.a. Band II: 1930–1939*. Ed. by K. Meyenn. Springer, Berlin, Heidelberg, 1985. ISBN: 978-3-540-13609-5. DOI: <https://doi.org/10.1007/978-3-540-78801-0> (cited on p. 4).
- [Peq08] J. Pequenao. *Computer generated image of the whole ATLAS detector*. Mar. 2008. URL: <https://cds.cern.ch/record/1095924> (cited on p. 30).
- [Per+21] I. Perić et al. *High-Voltage CMOS Active Pixel Sensor*. In: *IEEE Journal of Solid-State Circuits* 56.8 (2021), pp. 2488–2502. DOI: 10.1109/JSSC.2021.3061760 (cited on pp. 20, 22).
- [Per04] I. Perić. *Design and Realisation of Integrated Circuits for the Readout of Pixel Sensors in High-Energy Physics and Biomedical Imaging*. Ph.D. dissertation. Bonn University, 2004 (cited on p. 20).
- [Per07] I. Perić. *A novel monolithic pixel detector implemented in high-voltage CMOS technology*. In: 2 (2007), pp. 1033–1039. DOI: 10.1109/NSSMIC.2007.4437188 (cited on pp. 1, 19, 20).
- [Pet18] A. Peters. *Medical Applications - Instrumentation and Diagnostics*. June 2018. URL: <https://arxiv.org/pdf/2005.08729.pdf> (cited on p. 35).
- [Pet20] A. Peters. *Medical Applications – Instrumentation and Diagnostics*. 2020. arXiv: 2005.08729 [physics.ins-det] (cited on pp. 34, 37).
- [Phi09] Phirosiberia. *MOSFET: Depletion mode of n-channel transistor*. June 2009. URL: https://commons.wikimedia.org/wiki/File:MOSFET_depletion-mode_n-channel_en.svg (visited on 11/30/2021) (cited on p. 7).
- [Poi+14] T. Poikela et al. *Timepix3: a 65K channel hybrid pixel readout chip with simultaneous ToA/ToT and sparse readout*. In: *Journal of Instrumentation* 9.05 (May 2014), pp. C05013–C05013. DOI: 10.1088/1748-0221/9/05/c05013 (cited on p. 67).
- [Pra20] M. Prathapan. *High Voltage and Nanoscale CMOS Integrated Circuits for Particle Physics and Quantum Computing*. 54.02.03; LK 01. PhD thesis. Karlsruher Institut für Technologie (KIT), 2020. 186 pp. DOI: 10.5445/IR/1000105789 (cited on p. 73).
- [Rei+17] A. M. Reinhart et al. *Three dimensional reconstruction of therapeutic carbon ion beams in phantoms using single secondary ion tracks*. In: *Physics in Medicine & Biology* 62.12 (May 2017), pp. 4884–4896. DOI: 10.1088/1361-6560/aa6aeb (cited on pp. 37, 67, 68).

- [Ric+16] C. Richter et al. *First clinical application of a prompt gamma based in vivo proton range verification system*. In: Radiotherapy and Oncology 118.2 (2016), pp. 232–237. ISSN: 0167-8140. DOI: <https://doi.org/10.1016/j.radonc.2016.01.004> (cited on p. 37).
- [Rob18] Robert Koch Institut (RKI) - Zentrum für Krebsregisterdaten. *Krebsarten - Krebs gesamt*. 2018. URL: https://www.krebsdaten.de/Krebs/DE/Content/Krebsarten/Krebs_gesamt/krebs_gesamt_node.html;jsessionid=655FA54125242BD8059E1837602D76D7.internet071 (visited on 10/15/2021) (cited on p. 31).
- [RR20] M. Roser and H. Ritchie. *Moore’s Law Transistor Count 1970-2020*. Oct. 2020. URL: <https://ourworldindata.org/uploads/2020/11/Transistor-Count-over-time.png> (cited on p. 3).
- [Sau10] R. Sauer. *Halbleiterphysik: Lehrbuch für Physiker und Ingenieure*. Oldenbourg Wissenschaftsverlag, 2010. ISBN: 9783486598506. DOI: [doi:10.1524/9783486598506](https://doi.org/10.1524/9783486598506) (cited on p. 7).
- [Sca10] D. Scannicchio. *ATLAS Trigger and Data Acquisition: Capabilities and commissioning*. In: Nuclear Instruments and Methods in Physics Research Section A: Accelerators, Spectrometers, Detectors and Associated Equipment 617.1 (2010). 11th Pisa Meeting on Advanced Detectors, pp. 306–309. ISSN: 0168-9002. DOI: <https://doi.org/10.1016/j.nima.2009.06.114> (cited on p. 29).
- [Sch+08] J. Schwank et al. *Radiation effects in MOS oxides*. In: Nuclear Science, IEEE Transactions on 55 (Sept. 2008), pp. 1833–1853. DOI: [10.1109/TNS.2008.2001040](https://doi.org/10.1109/TNS.2008.2001040) (cited on pp. 13, 15, 16).
- [Sch+15] C. Schoemers et al. *The intensity feedback system at Heidelberg Ion-Beam Therapy Centre*. In: Nuclear Instruments and Methods in Physics Research Section A: Accelerators, Spectrometers, Detectors and Associated Equipment 795 (2015), pp. 92–99. ISSN: 0168-9002. DOI: <https://doi.org/10.1016/j.nima.2015.05.054> (cited on p. 34).
- [Sch+21] R. Schimassek et al. *Test results of ATLASPIX3 — A reticle size HVCMOS pixel sensor designed for construction of multi chip modules*. In: Nuclear Instruments and Methods in Physics Research Section A: Accelerators, Spectrometers, Detectors and Associated Equipment 986 (2021), p. 164812. ISSN: 0168-9002. DOI: <https://doi.org/10.1016/j.nima.2020.164812> (cited on pp. 21, 26).
- [Sch16] R. Schimassek. *Evaluation of CMOS Sensors as Particle Detectors at HL-LHC*. Master’s thesis. 2016 (cited on p. 20).
- [Sch21a] R. Schimassek. Personal communication. Dec. 2021 (cited on p. 89).
- [Sch21b] R. Schimassek. *Entwicklung und Charakterisierung von Integrierten Sensoren für die Teilchenphysik*. Ph.D. dissertation. Karlsruher Institut für Technologie (KIT), 2021. DOI: <https://doi.org/10.5445/IR/1000141412> (cited on pp. 2, 14, 21, 23, 37, 39, 40, 46, 49, 54, 61, 62, 64, 65, 67, 71, 73, 103).
- [Sch21c] A. Schlechter. *Monitoring of Carbon Ion Radiotherapy using track distributions of secondary ions at different detection angles*. Bachelor’s thesis. Department of Physics and Astronomy, University of Heidelberg, 2021 (cited on pp. 68, 87).
- [Sha+11] G. Shakirin et al. *Implementation and workflow for PET monitoring of therapeutic ion irradiation: a comparison of in-beam, in-room, and off-line techniques*. In: Physics in Medicine & Biology 56.5 (Feb. 2011), pp. 1281–1298. DOI: [10.1088/0031-9155/56/5/004](https://doi.org/10.1088/0031-9155/56/5/004) (cited on p. 36).

-
- [Tes+09] E. Testa et al. *Dose profile monitoring with carbon ions by means of prompt-gamma measurements*. In: Nuclear Instruments and Methods in Physics Research Section B: Beam Interactions with Materials and Atoms 267.6 (2009). Proceedings of the Seventh International Symposium on Swift Heavy Ions in Matter, pp. 993–996. ISSN: 0168-583X. DOI: <https://doi.org/10.1016/j.nimb.2009.02.031> (cited on p. 37).
- [Thu18] F. Thuselt. *Physik der Halbleiterbauelemente*. 3rd ed. Springer Spektrum, Berlin, Heidelberg, 2018. ISBN: 978-3-662-57638-0. DOI: <https://doi.org/10.1007/978-3-662-57638-0> (cited on pp. 6, 7).
- [Tri21] Trinamic Motion Control. *PD42-x-1140*. 2021. URL: <https://www.trinamic.com/products/drives/details/pd42-x-1140> (visited on 12/27/2021) (cited on pp. 71, 72).
- [TSD15] R. Turchetta, K. R. Spring, and M. W. Davidson. *Introduction to CMOS Image Sensors*. Nov. 2015. URL: <https://micro.magnet.fsu.edu/primer/digitalimaging/cmosimagesensors.html> (visited on 11/30/2021) (cited on p. 19).
- [Tse+07] L. Tsetseris et al. *Hydrogen effects in MOS devices*. In: Microelectronic Engineering 84.9 (2007). INFOS 2007, pp. 2344–2349. ISSN: 0167-9317. DOI: <https://doi.org/10.1016/j.mee.2007.04.076> (cited on p. 16).
- [Veb12] D. Veberič. *Lambert W function for applications in physics*. In: Computer Physics Communications 183.12 (2012), pp. 2622–2628. ISSN: 0010-4655. DOI: <https://doi.org/10.1016/j.cpc.2012.07.008> (cited on p. 49).
- [W-M06] W.-M. Yao et al. *Accelerator Physics of Colliders*. In: Journal of Physics G 33.01 (2006). URL: <https://pdg.lbl.gov/2006/reviews/accelrpp.pdf> (cited on p. 28).
- [WB19] D. Wiedner and N. Berger. *The Mu3e Experiment*. Feb. 2019. URL: <https://www.psi.ch/de/mu3e/introduction> (visited on 12/06/2021) (cited on p. 20).
- [Web21] A. Weber. *Development of Integrated Circuits and Smart Sensors for Particle Detection in Physics Experiments and Particle Therapy*. Ph.D. dissertation. Heidelberg University, 2021. DOI: <https://doi.org/10.11588/heidok.00030650> (cited on p. 37).
- [WK99] U. Weber and G. Kraft. *Design and construction of a ripple filter for a smoothed depth dose distribution in conformal particle therapy*. In: Physics in Medicine & Biology 44.11 (Oct. 1999), pp. 2765–2775. DOI: 10.1088/0031-9155/44/11/306 (cited on p. 34).
- [WSK21] M. Williams, S. Spannagel, and J. Kröger. *Corryvreckan User Manual*. Feb. 2021. URL: <https://project-corryvreckan.web.cern.ch/project-corryvreckan/usermanual/corryvreckan-manual-v2.0.1.pdf> (visited on 12/20/2021) (cited on p. 77).
- [ZF13] X. Zhu and G. E. Fakhri. *Proton Therapy Verification with PET Imaging*. In: Theranostics 3 (2013), pp. 731–740. DOI: 10.7150/thno.5162 (cited on pp. 34, 36).
- [Zie99] J. F. Ziegler. *Stopping of energetic light ions in elemental matter*. In: Journal of Applied Physics 85.3 (1999), pp. 1249–1272. DOI: 10.1063/1.369844. eprint: <https://doi.org/10.1063/1.369844> (cited on p. 9).
- [Zyl+20] P. Zyla et al. *Review of Particle Physics*. In: PTEP 2020.8 (2020), p. 083C01. DOI: 10.1093/ptep/ptaa104 (cited on pp. 9, 11).

Acknowledgments – Danksagung

Abschließend möchte ich mich bei allen bedanken, die maßgeblich zu dieser Arbeit beigetragen haben.

Zunächst möchte ich Herrn Prof. Dr. Ulrich Husemann für die Möglichkeit danken, meine Arbeit am Institut für Experimentelle Teilchenphysik durchzuführen. Danke für die schnellen und gewissenhaften Korrekturen und die Zeit für Diskussionen. Ein weiteres Dankeschön gilt Herrn Prof. Dr. Ivan Perić, für die spontane Übernahme des Korreferats und die spannende Einführung in die Welt der HV-CMOS Technologie durch seine Paper.

Dr. Rudolf Schimassek danke ich für die hervorragende Betreuung in der Endphase seiner Promotion und die sorgfältigen Korrekturen. Du hast Dir – wenn nötig – immer Zeit genommen, geduldig und mit viel Papier erklärt. Vielen Dank auch für alle interessanten Diskussionen und Ideen.

Dr. Stefan Maier danke ich für den organisatorischen, fachlichen und mentalen Beistand und die Korrekturen einiger Kapitel. Dr. Felix Ehrler danke ich für die Einführungen in die Bestrahlung von HV-CMOS Strukturen und die Unterstützung auf den Testbeams. Ebenfalls bedanke ich mich bei Dr. Alexander Dierlamm für die vielen Anregungen und Korrekturen. Ein großes Dankeschön gilt noch Marius Neufeld, der mit mir ein funktionales Setup aus dem Boden stampfte, das zu den Ergebnissen in dieser Arbeit führte.

Der gesamten Arbeitsgruppe des ETP danke ich für die produktive und angenehme Arbeitsatmosphäre: Tobias Barvich, Bernd Berger, Justus Braach, Luc Brandl, Dr. Alexander Droll, Umut Elicabuk, Diana Fellner, Gani Kösker, Roland Koppenhöfer, Prof. Dr. Thomas Müller, Dr. Jan-Ole Müller-Gosewisch, Dr. Andreas Nürnberg, Martin Pittermann, Alexander Salameh, Dr. Hans Jürgen Simonis, Julian Stanulla, Pia Steck, Lea Stockmeier und Florian Wittig. Ohne die emotionalen Tischkickerpausen, gelegentliche Spaziergänge und das ein oder andere Franzbrötchen wäre die Zeit nur halb so schön gewesen.

Jakob Naumann danke ich stellvertretend für das Heidelberger Ionenstrahl-Therapiezentrum für die Erstellung der Beamläne – die die Datennahme in dieser Form ermöglichten, die Messzeit und die spannenden Einblicke in die Thematik der medizinischen Bestrahlungen. Auch dem DKFZ gilt mein Dankeschön für die unkomplizierte Ausleihe des PMMA Zylinders.

Meinen Freunden und meiner WG danke ich für alle schönen Momente im Studium und außerhalb. Jakob Stark danke ich für die vielen Diskussionen bis spät in die Nacht, die Aufmunterungen und das Aufspüren einiger verschwundener Artikel. Ein weiteres großes Dankeschön gilt meiner Familie: Irmgard & Adam Haas, Gisela & Wolfgang Klauda und Wolfgang Haas. Danke mein Schwesterherz, Johanna, für alle vergangenen und kommenden Abenteuer.

Mein größtes Dankeschön richte ich an meine Eltern, Gertraud und Dr. Matthias Klauda: Danke für eure immerwährende Unterstützung, die vielen Wanderungen, Ausflüge und Gespräche am Esstisch, ich liebe euch von Herzen.